

Politecnico di Torino

ScuDo
Scuola di Dottorato ~ Doctoral School
WHAT YOU ARE, TAKES YOU FAR

Doctoral Dissertation
Doctoral Program in Energy Engineering (38^{th}cycle)

Verification and Validation of CFD Models for Multi-Physics Engineering Applications

By

Aldo Collaku

******

Supervisor(s):
Prof. L. Savoldi, Supervisor
Prof. L. D. Marocco., Co-Supervisor

Doctoral Examination Committee:
Prof. A. Cammi, Politecnico di Milano
Prof. G. Lomonaco, Università di Genova

Politecnico di Torino
2026

Declaration

I hereby declare that, the contents and organization of this dissertation constitute my own original work and does not compromise in any way the rights of third parties, including those relating to the security of personal data.

Aldo Collaku
2026

* This dissertation is presented in partial fulfillment of the requirements for **Ph.D. degree** in the Graduate School of Politecnico di Torino (ScuDo).

Abstract

Computational Fluid Dynamics (CFD) has become an essential tool in the analysis, design, and optimisation of complex engineering systems involving coupled physical phenomena such as fluid flow, heat transfer, species transport, multiphase effects, and electrochemical reactions. However, the increasing complexity of these models requires a rigorous assessment of their predictive capability, particularly when they are applied to design support or safety-critical contexts. In this framework, the Verification and Validation (V&V) methodology provides a structured approach to quantify numerical and modelling uncertainties and to assess the credibility of simulation results with respect to experimental or reference data. This work applies a comprehensive V&V framework to four representative case studies of increasing physical complexity: TPMS structures for heat transfer applications, a V-rib turbulence promoter, tritium transport in confined environments, and a Proton Exchange Membrane Fuel Cell (PEMFC) as a fully coupled multiphysics electrochemical system. Each case is used to investigate different dominant sources of uncertainty, ranging from geometric and manufacturing effects to turbulence modelling, transient flow behaviour, and electrochemical closure relations.

The first case study considers TPMS (Triply Periodic Minimal Surface) structures for heat transfer enhancement and pressure drop characterisation. The objective is the development of empirical correlations based on validated CFD simulations. The analysis combines grid convergence studies and experimental validation to quantify discretization and modelling uncertainties. Results show that model performance strongly depends on the TPMS orientation and operating conditions. While some configurations exhibit good agreement with experimental data within uncertainty bounds, others show systematic deviations attributable to manufacturing imperfections introduced by additive manufacturing, including surface roughness and geometric deviations from the idealised computational model. In addition, at low Reynolds numbers the relative importance of measurement uncertainty increases,

leading to larger discrepancies between numerical and experimental results. Overall, the TPMS study highlights the importance of accounting for geometric variability when developing reduced-order predictive models.

The second case study focuses on a V-rib configuration used as a turbulence promoter in conjugate heat transfer applications. The presence of ribs induces complex flow structures characterised by separation, reattachment, and secondary motion, which significantly enhance heat transfer while increasing pressure losses. Two turbulence modelling approaches are investigated: a lagged eddy-viscosity model and a Reynolds Stress Model (RSM). The V&V analysis shows that numerical uncertainty is strongly dependent on both mesh resolution and turbulence closure. The RSM provides improved predictions for thermal fields, accurately capturing the temperature evolution and characteristic trends observed experimentally, while the simpler model shows better robustness for hydraulic quantities. Validation against experimental data confirms that both models reproduce the main physical behaviour of the system, although discrepancies remain in regions dominated by strong anisotropy and thermal gradients. The study also identifies the assumption of simplified thermal boundary conditions as a relevant source of epistemic uncertainty.

The third case study addresses tritium transport in confined environments, where the objective is to assess the capability of CFD models to predict the dispersion and accumulation of radioactive species under complex flow conditions. This application is particularly relevant for safety assessment, as even moderate modelling inaccuracies may lead to significant deviations in predicted concentration levels in localised regions. The analysis reveals that the system is strongly influenced by transient flow structures and turbulence-driven mixing processes. In the absence of detailed experimental data, the assessment is based primarily on solution verification and sensitivity analysis. The results show that numerical predictions are highly sensitive to modelling assumptions related to turbulence representation and boundary conditions. In this context, the V&V framework is used to quantify numerical robustness and to identify the limits of applicability of the model rather than to perform strict validation. The study highlights that in safety-critical applications involving radioactive species such as tritium, uncertainty quantification is essential to ensure conservative and reliable interpretation of CFD results.

The fourth case study concerns a PEMFC, which involves strongly coupled electrochemical, thermal, and multiphase transport phenomena. The V&V analysis

is performed across different CFD platforms and modelling strategies, including ANSYS Fluent, STAR-CCM+, and OpenFOAM. Significant differences in numerical robustness and predictive accuracy are observed depending on the multiphase formulation and electrochemical implementation. Euler–Euler multiphase approaches exhibit numerical instability under certain conditions, while simplified formulations provide more stable but less detailed representations of the physical processes. Validation is performed using current density data, as no experimental measurements are available for liquid water saturation. The results show that discrepancies between numerical predictions and experiments are strongly influenced by differences in electrochemical modelling, interface treatment, and phase interaction assumptions. In particular, the kinetic-dominated regime exhibits larger deviations, highlighting the sensitivity of the model to the formulation of reaction source terms.

Across all four case studies, several general conclusions emerge. First, model-form uncertainty is consistently identified as the dominant contributor to the overall error budget once a sufficient level of grid refinement is achieved. Second, model performance is strongly dependent on the operating regime, with specific flow or transport conditions leading to a degradation of predictive accuracy. Third, the V&V framework proves essential not only for quantifying numerical and modelling uncertainties, but also for identifying the physical origins of discrepancies between simulations and experimental data. The results demonstrate that CFD model credibility cannot be defined in absolute terms, but must be assessed relative to a specific context of use and a quantified uncertainty range. Depending on the application, the same model may be suitable for engineering correlation development, design support, qualitative trend prediction, or only indicative analysis. This perspective is particularly relevant for multiphysics systems, where no single modelling approach is universally valid across all operating conditions. Overall, this work demonstrates that a systematic V&V methodology is essential to ensure that CFD simulations provide not only physically consistent results, but also quantitatively reliable information for engineering decision-making and safety assessment. By explicitly distinguishing between numerical errors, modelling assumptions, and experimental uncertainties, the proposed framework enables a transparent and robust interpretation of simulation results across a wide range of complex engineering applications.

Contents

List of Figures viii

List of Tables xiii

1 Introduction 1

1.1 Verification and Validation in Computational Fluid Dynamics 1

1.2 Objective and Scope of the Thesis 3

2 Verification and Validation Methodology 8

2.1 V&V Framework and Workflow 9

2.2 Definition of Quantities of Interest 12

2.3 Sources of Numerical Uncertainty in CFD 13

2.4 Solution Verification 16

2.5 Validation and Comparison Strategies 19

3 Pure hydraulic model of a Triply Periodic Minimal Surface 24

3.1 Problem Definition and Intended Use 25

3.2 Numerical Model Description 26

3.3 Application of the V&V Methodology 29

3.4 Model Credibility and Discussion 32

4 Thermo-Fluid Dynamic Model of a V-Rib turbulence promoter 36

4.1 Problem Definition and Intended Use 37
4.2 Numerical Model Description 39
4.3 Application of the V&V Methodology 42
4.4 Model Credibility and Discussion 51

5 CFD Assessment of Tritium Release in a ITER Process Systems 54
5.1 Problem Definition and Intended Use 55
5.2 Numerical Model Description 57
5.3 Solution Verification 58
5.4 Model Assessment and Numerical Robustness 63

6 Multiphysics and Multiphase model of a lab scale PEM Fuel Cell 67
6.1 Problem Definition and Intended Use 69
6.2 Numerical Model Description 70
6.3 Application of the V&V Methodology 73
6.4 Model Credibility and Discussion 79

7 Discussion and Conclusions 86

References 90
.1 Appendix A - V-rib Geometry and CFD Results 94
.2 Appendix 2 - PEM Fuel Cell Physics and Numerical Implementation 97

List of Figures

2.1 Schematic representation of the verification and validation workflow adopted in this work. The intended use defines the Quantities of Interest, followed by verification and, when experimental data are available, validation to assess model credibility. 10

3.1 Examples of different triply periodic minimal surface (TPMS) unit cell structures; this study focuses on the analysis of the gyroid one. . 25

3.2 CAD representation of the computational domain, including inlet section, TPMS core, and outlet extrusion. 26

3.3 Different orientations of the gyroid TPMS structure tested in the experimental setup and analyzed in this study: (a) $-45°$, (b) $+45°$, and (c) $0°$. 27

3.4 Pressure probe locations highlighted in purple, corresponding to the positions of the experimental pressure transducers. Pressure values are extracted using point-wise, volume-averaged (0.1 mm spherical region), and surface-averaged approaches, all providing consistent results. 29

3.5 Different mesh refinement displayed on a cross-sectcion of the TPMS sampling (-45° orientation) from finest (a) to coarsest (c). 30

3.6 Validation error δ_{model} for the three TPMS orientations ($0°$, 45^{+}, 45^{-}). The colored markers indicate the numerical results for each configuration (blue: 45^{+}, green: $0°$, red: 45^{-}), while the error bars represent the associated validation uncertainty. 33

4.1 Schematic representation of the prototypical mock-up of the HCPB First Wall cooling system (left) and detail of the V-rib turbulence promoter geometry (right), highlighting the rib arrangement along the heated wall of the channel. 37

4.2 Geometry (a) and boundary conditions (b) of the computational domain of a single step of V-rib, including the applied heat flux and characteristic dimensions of the periodic unit. 41

4.3 Flow-chart illustrating the numerical workflow adopted for grid independence assessment and thermo-hydraulic simulation sequence. 41

4.4 Domain cross-section highlighting different grid refinement in the fluid and solid regions. 43

4.5 Section view of the computational grids from the coarsest (a) to the finest (e). 43

4.6 Grid convergence of the maximum velocity for different turbulence models. The red line refers to the RSM model, while the blue line corresponds to the Lag-EB model. 45

4.7 Grid convergence of the pressure drop for different turbulence models. The red line refers to the RSM model, while the blue line corresponds to the Lag-EB model. 45

4.8 Grid convergence of the temperature increase for different turbulence models. The red line refers to the RSM model, while the blue line corresponds to the Lag-EB model. 46

4.9 Test section of the ribbed channel (a) and cross-section of the channel (b) adopted in the HETREX-PT experimental campaign. 47

4.10 Geometry and boundary conditions adopted for the CFD simulation of the HETREX-PT test section. 48

4.11 Computational mesh for the HETREX-PT configuration: detail of the ribbed region and inlet/outlet extrusion (a), transversal and longitudinal sections highlighting mesh refinement (b). 49

4.12 Location of numerical probes corresponding to experimental measurement points along the channel. The figure also shows reference sections used for post-processing of velocity and temperature fields (reported in Appendix .1) 49

4.13 Temperature profile along the axial coordinate at thermocouple locations: comparison between CFD predictions (Lag-EB and RSM), experimental data, and CFX results. 50

4.14 Pressure profile along the axial coordinate: comparison between CFD predictions (Lag-EB and RSM), experimental data, and CFX results. 50

5.1 Computational domain of the ITER Process Room #2, including tritium release location and monitoring points used for the evaluation of the QoI. 56

5.2 Boundary conditions adopted for the CFD simulation of the ITER Process Room #2. 58

5.3 Standard deviation of the specific activity at the monitoring locations, reported in absolute value (a) and normalized with respect to the mean value (b), for the two turbulence models, SST in blue and RNG in red. 59

5.4 Specific activity at monitoring locations as a function of normalized grid size for (a) k–ω SST and (b) k–ε RNG turbulence models. . . . 61

5.5 Time evolution of the specific activity at the monitoring locations for the SST (red) and RNG (black) turbulence models. Uncertainty bands derived from the numerical uncertainty analysis are also reported. 64

5.6 Computed detection times corresponding to (a) 1 DAC and (b) detection threshold for the different monitoring locations. 65

6.1 Schematic representation of the PEM fuel cell structure, including membrane electrode assembly and flow field channels [1]. 68

6.2 Details of the computational grid of the PEMFC segment common to the three software. Grid refinement is performed only in the porous zone in the through-plane direction. 75

6.3 Through-plane cross-sections of the different computational grid refinements adopted in the solution verification. 76

6.4 Local profiles of liquid water saturation along the cathode porous layers for Fluent (red), STAR-CCM+ (black), and OpenFOAM multiphase model (blue). 77

6.5 Current density (a) and liquid saturation (b) normalized to the respective extrapolated values for Fluent (red), OpenFOAM (blue and green) and STAR-CCM+ (black). In OpenFOAM current density has been computed with a single phase model (green) and two phase model (blue). 83

6.6 Comparison error computed at the validation point for STAR-CCM+ (blue), Fluent (red) and OpenFOAM (magenta). Modeling error expressed in absolute value on top axis and in percentage terms on the bottom axis. 84

6.7 Polarization curve (a), provided with validation uncertainty, and modeling error δ_{model} (b) computed with the most refined grid with the different solvers for the whole polarization curve. 85

1 V-rib geometry with main geometric parameters and rib orientation as implemented in the numerical model based on the experimental design specifications. 94

2 Section view of the computational domain derived from the experimental test section. The modeled configuration reproduces the main features of the HETREX-PT setup, including the heated channel and flow direction. 94

3 Temperature field at the heated wall computed with RSM (a) and Lag-EB (b). The comparison highlights differences in thermal spreading and local heat transfer enhancement induced by the turbulence closure. 95

4 Temperature distribution on a representative cross-section of the channel computed with RSM (a) and Lag-EB (b), showing differences in thermal mixing and boundary layer development. 95

5 Velocity field computed with RSM and Lag-EB turbulence models. Top: full domain representation. Bottom: selected cross-sections at inlet (right), mid-plane (center), and outlet (left), illustrating differences in flow redistribution induced by the rib structures. 96

6 Computational domain of PEMFC segment. 105

List of Tables

2.1 Summary of Quantities of Interest (QoIs) for the considered case studies. 13

3.1 Grid refinement study for the TPMS case for three orientations ($-45°$, $0°$, $+45°$). 30

3.2 Metrics of the 5-step solution verification procedure for the pressure drop across the TPMS sample. 31

3.3 Validation uncertainty and comparison error for the pressure drop across the TPMS sample. 32

4.1 Mesh parameters for the grid refinement study. 44

4.2 Numerical uncertainties associated with the selected grid (case c). . 46

5.1 Mesh parameters adopted for the grid refinement study. 60

5.2 Summary of numerical uncertainties for the finest grid and the two turbulence models. The total uncertainty u_{num} is obtained by conservatively summing the spatial discretization and observed temporal variability contributions. 63

6.1 Set of governing equations used to describe multiphase transport and electrochemical charge conservation in the PEMFC model, common to STAR-CCM+ and ANSYS Fluent. Equations are expressed in a generalized steady-state multiphase formulation. [2, 3]. 72

6.2 Set of governing equations used to describe multiphase transport and electrochemical charge conservation in the OpenFOAM PEMFC model. [4]. 72

6.3 Source terms for the governing equations in the PEMFC domains. . 73

6.4 Number of computational cells in the through-plane direction adopted for each grid. 75

6.5 Representative grid size and refinement ratios for the grid convergence study. 76

6.6 Metrics of the 5-steps procedure of the solution verification considering the current density (A/cm^2) and liquid saturation (-) of the PEMFC under investigation. 82

6.7 Validation uncertainties and comparison errors computed for the current density at the validation point of $0.7V$ for the three software. 84

1 Parameters used in the Butler–Volmer equations (15). 102

2 Computational domain thickness in μm. 104

3 Operating conditions of the experimental PEMFC adopted in the numerical models. 105

4 Material properties adopted in the numerical models [5–7]. 106

Chapter 1

Introduction

1.1 Verification and Validation in Computational Fluid Dynamics

The increasing use of CFD as a quantitative tool for engineering analysis introduces a fundamental requirement: numerical results must be accompanied by a clear assessment of their reliability. This requirement does not arise from the complexity of specific applications, but from the intrinsic structure of numerical modeling, where multiple sources of approximation coexist and interact [8]. Any CFD prediction is the outcome of a sequence of modeling and numerical choices. The governing equations are formulated under specific assumptions, closure models approximate unresolved physics, boundary conditions idealize real operating environments, and discretization introduces a finite representation of the problem. These elements do not contribute independently, but combine in a non-trivial way, making it difficult to isolate the origin of discrepancies between simulations and physical observations. For this reason, the evaluation of model reliability cannot rely on qualitative agreement or isolated comparisons. A structured approach is required to separate and interpret the different contributions to the overall error. Discretization errors depend on mesh resolution and numerical schemes, and can be systematically reduced through grid refinement [9]. Iterative errors are associated with solver convergence and must be controlled to ensure solution consistency [10]. Modeling errors originate from the assumptions embedded in closure relations and often represent the dominant source of uncertainty in complex flows. Additional variability is introduced through input

parameters and boundary conditions, while experimental data used for comparison are affected by measurement uncertainty and limited resolution.

Within this framework, verification and validation provide a formal distinction between different aspects of model assessment [8]. Verification addresses the numerical problem, focusing on whether the governing equations are solved consistently. It involves the analysis of convergence behavior and the estimation of discretization uncertainty for selected Quantities of Interest. Validation, on the other hand, concerns the physical problem, evaluating the extent to which the mathematical model represents reality under specific conditions. These two steps are inherently linked but conceptually distinct: verification establishes numerical reliability, while validation addresses physical credibility. A central element in this process is the definition of the intended use of the model. Credibility is not an absolute property, but depends on the purpose of the simulation and on the acceptable level of uncertainty associated with the decision it supports. A model may be adequate for trend analysis and inadequate for design verification, or acceptable for nominal conditions but unreliable when extrapolated beyond the validated range. This perspective requires that uncertainty is not only quantified, but also interpreted in relation to the specific application.

To formalize these concepts, several methodologies have been developed, among which the ASME V&V 20-2009 Standard for Verification and Validation in Computational Fluid Dynamics and Heat Transfer represents a widely adopted reference for CFD and heat transfer applications [11]. The standard provides a structured procedure for defining Quantities of Interest, performing solution verification, and assessing the agreement between simulations and experimental data. Its main contribution lies in linking uncertainty quantification to decision-making, rather than treating it as a purely numerical exercise. Practical implementations of this framework have been discussed in the literature, including structured workflows tailored to engineering applications [12]. Despite this structured framework, the practical implementation of V&V remains challenging. Grid convergence studies require additional simulations, uncertainty quantification increases computational cost, and validation depends on the availability of reliable experimental data. In time-constrained engineering environments, these requirements are often only partially addressed, leading to simplified procedures that do not fully capture the underlying uncertainty. These limitations are amplified in multiphysics applications, where different modeling components interact and contribute to the overall behavior of the system. In such cases, V&V serves not only to quantify numerical errors, but also to identify dominant

modeling assumptions, reveal sensitivities, and, when necessary, question the applicability of the model itself. The present work adopts the ASME V&V20 framework as a reference and evaluates its application across a set of heterogeneous case studies. The focus is placed on its operational use, with the objective of assessing how a consistent credibility assessment procedure can be integrated into practical CFD analyses and how it influences the interpretation of simulation results. Across all applications, a common sequence is followed. The intended use is first defined, and the relevant Quantities of Interest are identified. Solution verification is then performed through grid refinement and discretization error estimation. When experimental data are available, validation is conducted by comparing numerical predictions with measurements, accounting for experimental uncertainty. In cases where direct validation is not feasible, sensitivity analyses and inter-code comparisons are used to assess the robustness of the results. The final step consists in evaluating model credibility in relation to the specific decision context. This approach allows different applications, characterized by distinct physical regimes and modeling assumptions, to be analyzed within a unified framework, providing a consistent basis for interpreting the role and limitations of CFD in engineering practice.

1.2 Objective and Scope of the Thesis

Building upon the Verification and Validation framework introduced in the previous section, Computational Fluid Dynamics (CFD) has progressively evolved from a supporting analysis tool to a central pillar in the design and safety assessment of advanced energy technologies. In nuclear, aerospace and electrochemical applications, numerical simulations are routinely employed to explore operating conditions, optimize geometries, reduce experimental campaigns, and anticipate off-design or accidental scenarios. The increasing geometrical complexity of modern components, the presence of coupled multiphysics phenomena, and the need to operate under extreme thermal, mechanical, or chemical loads have reinforced this trend. In such contexts, CFD results are no longer interpreted as qualitative flow visualizations, but as quantitative inputs to engineering decisions. However, predictive capability is not an intrinsic property of a numerical model but it must be demonstrated. Governing equations are approximated, turbulence and multiphase effects are modeled through closures, geometries are discretized, and boundary conditions are simplified

representations of physical reality. Each of these steps introduces numerical errors and uncertainties. When simulations are used to support design or safety decisions without a structured assessment of these uncertainties, the apparent precision of numerical outputs can conceal substantial epistemic limitations. In complex multiphysics systems, the absence of a rigorous Verification and Validation (V&V) process can therefore lead either to unjustified confidence or to the complete dismissal of otherwise valuable computational tools. The ASME V&V 20-2009 standard provides a formal framework for the credibility assessment of computational fluid dynamics and heat transfer models. It establishes a structured methodology to define the intended use of a model, identify relevant Quantities of Interest (QoIs), estimate discretization errors through solution verification, quantify uncertainties, and evaluate agreement with experimental data through validation metrics. In principle, such a framework transforms CFD from a heuristic instrument into a quantitatively assessed predictive tool. In practice, however, a lack of systematic evidence persists regarding how V&V20 performs when applied to heterogeneous, industrially relevant multiphysics systems, and how its outcomes concretely influence engineering decisions. The standard is often perceived as resource-intensive, conservative, and difficult to integrate into time-constrained engineering workflows. As a consequence, V&V activities are frequently simplified or partially implemented, reinforcing the gap between formal methodological prescriptions and pragmatic industrial practice. The objective of this thesis is to investigate the operational value of the ASME V&V20 standard when applied to multiphase and multiphysics CFD models of practical relevance in energy-related applications. Rather than proposing a new theoretical framework, this work implements the existing standard across four heterogeneous case studies, characterized by different physical regimes, modelling assumptions, and decision contexts, in order to assess its practical robustness and engineering impact. The selected case studies span laminar and turbulent regimes, steady and unsteady flows, as well as single-phase and multiphase configurations, providing a broad testbed to evaluate the applicability and limitations of the V&V framework under diverse conditions.

The first case study focuses on a Triply Periodic Minimal Surface (TPMS) geometry used as a compact heat exchanger configuration, with potential applications in aerospace and nuclear energy systems. These structures, manufactured via Additive Manufacturing (AM), are being investigated for their ability to provide high surface area while reducing weight and volume. The activity originates from an experimental

campaign aimed at characterizing the hydraulic performance of such structures under controlled laboratory conditions. The flow regime is laminar, and the main Quantity of Interest is the pressure drop as a function of mass flow rate. In this context, the objective is not limited to reproducing experimental results, but to quantify the numerical uncertainty associated with the CFD model used to support the experiments, since the same model is then employed to derive an empirical correlation between mass flow rate and pressure drop. The application of the V&V framework therefore allows the resulting correlation to be interpreted in terms of predictive capability over a defined operating range, rather than as a simple fit of the available data.

The second case study concerns a turbulence promoter, referred to as V-rib, investigated in the context of high heat flux cooling applications for nuclear fusion systems, where efficient heat removal represents a primary design constraint, as structural integrity and operational reliability are directly linked to the capability of the cooling architecture to withstand extreme thermal loads. The activity originates from a collaborative effort with the Karlsruhe Institute of Technology (KIT), where dedicated experimental campaigns were conducted to characterize the thermo-hydraulic performance of ribbed channel configurations, in particular within the Helium Thermal Hydraulics Experimental (HETREX) facility. In this context, preliminary CFD analyses were available but exhibited limited predictive capability, particularly in capturing the complex flow structures induced by the rib geometry. The need for a more reliable numerical representation emerged as a critical requirement to support the interpretation of experimental data and to extend the analysis beyond the tested conditions. The present work revisits the available CFD model within a structured Verification and Validation framework, with the aim of quantifying its predictive capability, making the associated uncertainties explicit, and clarifying the extent to which turbulence modeling assumptions influence the overall credibility of the results.

The third case study addresses the simulation of a radioactive release in a confined environment, in the context of safety system design for nuclear fusion facilities. The activity is part of a broader effort to assess and optimize monitoring strategies for hazardous releases in controlled environments, where experimental investigations are difficult, costly, and often constrained by safety considerations. The reference scenario consists of a constant release of tritium within a representative process room configuration, including the main geometrical features and the operating HVAC system. The objective of the simulation is to track the time evolution of the

contaminant concentration at selected monitoring locations, providing quantitative support for the evaluation of detection system performance. In this context, CFD represents a potentially valuable tool for design and analysis, but the reliability of numerical predictions becomes critical, as the results may directly influence safety-related decisions. However, no experimental data are available for this configuration, preventing a formal validation of the model. As a consequence, the analysis is limited to solution verification and numerical uncertainty quantification, highlighting the boundaries within which the simulation results can be interpreted. The complexity of the flow, driven by the interaction between ventilation, obstacles, and transient source terms, introduces multiple sources of uncertainty that must be explicitly accounted for, motivating a structured assessment of numerical errors and their impact on the overall credibility of the simulation results in relation to their intended use.

The fourth case study focuses on the modeling of a Polymer Electrolyte Membrane Fuel Cell (PEMFC), a key technology for efficient and low-emission energy conversion in both stationary and transport applications. Despite their apparent simplicity at the system level, PEMFCs involve strongly coupled multiphysics phenomena, including electrochemical reactions, multi-species transport, heat transfer, and two-phase flow within porous media, making their numerical modeling particularly challenging. The activity builds upon an experimental campaign conducted on a laboratory scale fuel cell, for which a detailed numerical model is developed and implemented across three different CFD solvers: ANSYS Fluent, STAR-CCM+ and OpenFOAM. While these tools rely on similar physical principles, differences in model implementation, numerical schemes, and multiphase formulations can lead to significantly different predictions, even under identical operating conditions. In this context, the objective is not limited to reproducing the experimental polarization curve, but to investigate the consistency and reliability of the numerical solutions across different computational frameworks. In addition to validation against experimental data, a code-to-code comparison is performed to assess the consistency of the numerical predictions. This comparison, while not constituting validation in a strict sense, provides complementary insight into the influence of solver-dependent assumptions and numerical implementations. Particular attention is given to the role of these assumptions and to the stability of the multiphase formulations, which are known to be a critical aspect in PEMFC simulations. The study therefore combines validation and code-to-code analysis to clarify the extent to which simulation results can be considered reliable for engineering use.

The original contribution of this thesis lies in the systematic application of the ASME V&V20 framework to a set of heterogeneous multiphysics problems of direct engineering relevance. By adopting a common credibility assessment structure across different physical regimes and modeling approaches, the work highlights how verification and validation can be effectively integrated into practical CFD workflows, not only to quantify numerical uncertainty, but also to expose modeling limitations, delimit the range of applicability of simulation results, and support more informed engineering decisions. In this perspective, the thesis does not aim at extending the theoretical foundations of V&V, but at clarifying its operational value, identifying its limitations, and demonstrating the conditions under which its application remains both meaningful and sustainable within realistic engineering constraints.

Chapter 2

Verification and Validation Methodology

This chapter defines the verification and validation (V&V) methodology adopted to assess the accuracy and credibility of Computational Fluid Dynamics (CFD) models across the applications considered in this work. The methodology is formulated in accordance with the principles established in the ASME V&V20 standard [11], with the objective of quantifying the degree of agreement between simulation results and reference data for specified Quantities of Interest (QoI) under defined conditions. Within this context, verification and validation are treated as distinct but sequential processes. Verification addresses the correctness of the numerical solution with respect to the underlying mathematical model. This includes the assessment of discretization errors, iterative convergence, and the overall consistency of the numerical formulation. Validation, by contrast, evaluates the degree to which the mathematical model represents physical reality for its intended use, through comparison with experimental data or, when such data are not available, through alternative consistency assessments.

The primary objective of the V&V process is not the elimination of error, but its quantification. Numerical predictions are inherently affected by multiple sources of error and uncertainty, including discretization effects, modeling assumptions, and uncertainties in boundary conditions and input parameters. In this framework, accuracy is expressed as a bounded quantity associated with a specific QoI, rather than as a global property of the model. A central concept in the present methodology

is that model credibility is conditional upon the intended use. A simulation cannot be considered valid in a general sense, but only with respect to the specific conditions, variables, and decisions it is intended to support. Consequently, the assessment of accuracy is always formulated relative to explicitly defined QoIs and operating conditions. The approach adopted in this work follows a structured sequence consistent with the V&V20 framework. For each application, the intended use of the model is defined, relevant QoIs are identified, and solution verification is performed to estimate numerical uncertainty. Validation is then carried out through comparison with experimental data when available. The final outcome is a quantitative and context-dependent assessment of model credibility. The methodology is applied uniformly across all case studies, which include turbulent heat transfer, laminar flow in complex geometries, transient species transport in confined environments, and multiphysics electrochemical systems. Despite the differences in physical modeling and numerical implementation, the same V&V structure is maintained, ensuring consistency in the evaluation of uncertainty and in the interpretation of simulation results.

2.1 V&V Framework and Workflow

The credibility assessment of a CFD model is conducted through a structured sequence of steps that progressively constrain the interpretation of numerical results. The process is not a linear execution of independent tasks, but a chain of dependent operations in which each stage defines the admissible outcomes of the subsequent one. A schematic representation of the workflow is reported in fig. 2.1.

The workflow explicitly reflects the hierarchical dependency among the different steps, highlighting how the definition of the intended use constrains the selection of QoIs and propagates through verification and validation, ultimately determining the level of confidence that can be associated with the model predictions. The process begins with the definition of the intended use of the model. This step establishes the decision context in which the simulation is employed, including the relevant operating conditions and the level of accuracy required to support engineering conclusions. The intended use acts as a boundary condition for the entire V&V process, as it determines which physical phenomena must be resolved and which level of uncertainty can be tolerated. Without this definition, any statement on model

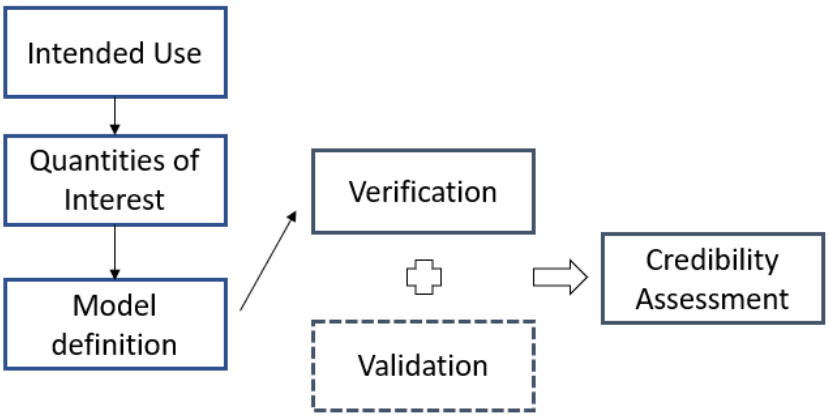


Fig. 2.1 Schematic representation of the verification and validation workflow adopted in this work. The intended use defines the Quantities of Interest, followed by verification and, when experimental data are available, validation to assess model credibility.

accuracy remains ambiguous. Following the definition of the intended use, a set of Quantities of Interest is identified which represent the variables through which model predictions are evaluated and compared. They correspond to measurable physical quantities, such as temperature or pressure drop, or obtained through a combination of measured variables. For instance, a heat transfer coefficient can be derived from temperature measurements, heat flux, and fluid properties, introducing additional sources of uncertainty that must be accounted for in the validation process. The selection of QoIs reduces the full solution field to a limited set of variables, and therefore implicitly defines which aspects of the model are assessed and which are not. Once the QoIs are defined, the computational model is constructed. This includes the specification of governing equations, constitutive relations, boundary conditions, and numerical discretization schemes. At this stage, multiple sources of approximation are introduced simultaneously. These include modeling assumptions, simplifications in geometry and boundary conditions, and numerical errors associated with discretization. The resulting solution cannot be interpreted directly, as the contribution of each source of error is not yet quantified.

The next step in the workflow is verification, which aims to quantify the numerical uncertainty affecting the computed QoIs. Within the V&V framework, it is necessary to distinguish between code verification and solution verification. Code verification addresses the correctness of the numerical implementation, ensuring that the governing equations are solved without programming or algorithmic errors.

This involves ensuring that convective, diffusive, and source terms are correctly discretized, boundary conditions are consistently applied, and the numerical scheme achieves the expected order of accuracy as the grid is refined. In general terms, code verification aims to ensure the absence of bugs and the correct numerical behavior of the solver. In practical engineering applications, code verification is rarely performed directly by the end user. When established commercial solvers are used, this responsibility is typically delegated to the software developer, who is expected to ensure code correctness through internal verification procedures. This reliance is often unavoidable, especially when using black-box solvers, where access to the underlying numerical implementation is limited or unavailable. As a result, users generally assume that code verification has been adequately addressed and instead focus on the assessment of the specific simulation. From a methodological standpoint, however, this assumption represents a limitation that should be explicitly acknowledged. Although widely used solvers may have undergone extensive verification, this does not guarantee correctness for all possible model configurations or combinations of physical models. The ASME V&V20 standard explicitly cautions against relying solely on vendor-provided verification and recommends independent assessment whenever feasible. In practice, such independent verification is rarely carried out due to time constraints and the complexity of real-world applications. A rigorous approach to code verification relies on the comparison of numerical results with exact analytical solutions. Since analytical solutions of the full governing equations are generally not available for realistic problems, the Method of Manufactured Solutions (MMS) is often adopted as a systematic alternative. In this approach, an artificial analytical solution is constructed, and the governing equations are modified accordingly so that this solution becomes exact. The numerical solver is then tested against this reference to assess its correctness. Although theoretically robust, this procedure is typically restricted to simplified configurations and is rarely applied in industrial contexts due to its complexity and limited direct relevance to practical applications.

For these reasons, the present work assumes code verification as a prerequisite and focuses on solution verification, which is problem-dependent and directly relevant to the assessment of numerical accuracy. As commonly stated in the V&V literature, *verification answers the question: "am I solving the equations correctly?", while validation addresses "am I solving the correct equations?"*. In this context, solution verification is performed through systematic grid refinement and the assess-

ment of iterative convergence. The objective is to evaluate the sensitivity of the QoIs to spatial and temporal discretization and to estimate the associated uncertainty. This process provides a quantitative measure of the numerical error affecting the solution, which must be established before any validation activity is undertaken.

2.2 Definition of Quantities of Interest

Within the V&V framework, the definition of Quantities of Interest establishes the variables on which the entire credibility assessment is performed. QoIs represent the link between the numerical solution and the engineering objective, and therefore determine both what must be verified and what must be validated. A QoI is generally not a primary solution variable, but a quantity derived from the numerical fields. Depending on the application, it can be defined as a local value (e.g., temperature at a specific location), a volume or time averaged quantity (e.g., mean concentration or velocity), or a quantity obtained through post-processing operations (e.g., pressure drop between two sections, integral fluxes, or performance indicators). This distinction is relevant because numerical errors propagate differently depending on how the QoI is constructed from the underlying solution. The selection of QoIs is driven by the intended use of the model and by the availability of reference data. In CFD analyses, QoIs can naturally coincide with primary solution variables of the governing equations, such as velocity, pressure, or scalar fields. However, in validation oriented studies, it is essential to define QoIs in a manner consistent with measurable quantities, so as to enable a direct comparison between simulation and experiment. In design-oriented applications, QoIs can also correspond to derived performance metrics or operational constraints, which are obtained from the primary solution variables through appropriate post-processing.

In the present work, QoIs are defined coherently with the objectives of each case study. In the TPMS heat transfer promoter, the QoI is the pressure drop between inlet and outlet, expressed as a function of the mass flow rate. For the V-rib configuration, the temperature and pressure profiles along the channel are used to characterize the thermo-hydraulic behavior of the system. In the tritium release scenario, the QoIs are the detection times at multiple monitoring locations, defined as the time required to reach specified concentration thresholds. In the PEM fuel cell model, the QoIs are the mean current density under potentiostatic conditions and the average liquid

water fraction within the porous regions of the cell. A summary of the defined QoIs is reported in Table 2.1.

The definition of QoIs directly influences the subsequent steps of the V&V process. Solution verification must be performed on these quantities, ensuring that discretization errors are quantified at the level relevant to the analysis. Similarly, validation must be carried out on QoIs that are consistent with experimental measurements, including their spatial and temporal resolution.

Table 2.1 Summary of Quantities of Interest (QoIs) for the considered case studies.

Case Study	**QoI**	**Definition**	**Unit**
TPMS	Pressure drop	Inlet-outlet difference	[Pa]
V-rib	Temperature profile	Pointwise values along channel	[K]
	Pressure profile	Pointwise values along channel	[Pa]
T-detection	Detection time	Time to reach threshold	[s]
PEMFC	Current density	Volume-averaged in catalyst layer	$\left[\frac{A}{m^2}\right]$
	Liquid fraction	Volume-averaged in porous media	[–]

2.3 Sources of Numerical Uncertainty in CFD

The assessment of numerical accuracy requires a clear distinction between *error* and *uncertainty*, following the common definitions in the literature [11, 9, 8, 12]. An error is defined as the difference between a quantity of interest and its true value, which remains an abstract and generally unknown reference. In this context, the error represents the unknown deviation from the true value, while uncertainty provides a quantitative estimate of the bounds within which this error is expected to lie, based on available information and assumptions.

Denoting a generic quantity by X, this relation can be expressed as:

$$X = X_{\text{true}} + \delta \tag{2.1}$$

where δ represents the total error. In practice, the objective is not to determine δ exactly, but to estimate a bounded interval within which it is expected to lie. Uncertainty is therefore introduced as a quantitative estimate of this bound. It is defined as a parameter that characterizes the dispersion of values that can reasonably

be attributed to a quantity. In this context, an uncertainty u provides an interval $[-u, +u]$ within which the error is expected to lie with a given level of confidence. When a confidence level is explicitly specified, the uncertainty is referred to as expanded uncertainty.

In CFD applications, multiple sources contribute to the total numerical error affecting a computed solution. Restricting the discussion to numerical aspects, the overall numerical uncertainty can be expressed as the combination of three main contributions:

$$u_{num} = \sqrt{u_{disc}^2 + u_{iter}^2 + u_{round}^2} \tag{2.2}$$

where u_{disc}, u_{iter}, and u_{round} denote the contributions associated with discretization, iterative convergence, and round-off errors, respectively. These quantities are expressed as standard uncertainties, corresponding to one standard deviation under the assumption that the individual error sources can be treated as statistically independent. The root-sum-square formulation therefore represents the propagation of independent uncertainty contributions rather than a direct summation of the corresponding errors.

The discretization error originates from the replacement of continuous governing equations with a finite set of algebraic equations defined on a discrete grid. This error depends on mesh resolution and on the formal order of accuracy of the numerical scheme. In the limit of vanishing grid spacing, a consistent numerical method is expected to converge toward the exact solution of the mathematical model. Discretization error typically represents the dominant contribution to numerical uncertainty and is therefore the primary target of solution verification.

The iterative error arises from the use of iterative algorithms to solve the discretized equations. At any finite number of iterations, the numerical solution does not exactly satisfy the discrete system, resulting in a residual error relative to the fully converged solution on the given grid. Iterative convergence is therefore defined as the reduction of this error to a level that does not affect the quantities of interest. Within the V&V framework, it is required that the iterative error be reduced to at least one or two orders of magnitude below the discretization error, so that its contribution to the overall numerical uncertainty can be neglected.

The round-off error is associated with the finite precision representation of real numbers in computer arithmetic. Although always present, it is generally negligible in practical CFD simulations when double-precision solvers are employed. As a consequence, it is not explicitly treated in the present analysis.

The round-off error is associated with the finite precision representation of real numbers in computer arithmetic. Although it is always present, it is generally negligible in practical CFD simulations when double-precision solvers are employed. As a consequence, it is not explicitly treated in the present analysis.

It is important to note that numerical uncertainty represents only one component of the overall uncertainty affecting simulation results. Additional contributions arise from input uncertainty, associated with boundary conditions, material properties, and operating parameters, and from experimental uncertainty when validation data are considered. However, these aspects are addressed separately within the validation process and sensitivity analyses. The focus of this section is limited to the identification of numerical error sources that can be controlled and quantified through solution verification. In practical CFD applications, the relative importance of the different numerical error sources is not uniform across all problems and quantities of interest. While round-off and iterative errors can generally be reduced to negligible levels through appropriate solver settings, discretization error often remains the dominant contribution. Its magnitude depends not only on the grid resolution, but also on the ability of the mesh to adequately represent the relevant physical gradients and transport mechanisms. As a consequence, the same numerical setup may yield significantly different uncertainty levels depending on the selected QoI. Quantities involving strong gradients, localized phenomena, or nonlinear source terms are typically more sensitive to discretization effects than globally averaged variables. This aspect is particularly relevant in multiphysics applications, where different physical processes may require different spatial resolutions to be accurately captured.

These considerations motivate the need for a systematic solution verification procedure, in which discretization effects are quantified explicitly for each QoI. The methodology adopted to perform this assessment is presented in the following section.

2.4 Solution Verification

Solution verification represents the first operational step of the V&V process and aims at quantifying the numerical uncertainty affecting the computed Quantities of Interest (QoIs). As previously discussed, numerical errors arise from three main sources: round-off, iterative, and discretization errors. In practical CFD applications, the discretization error is typically the dominant contribution, provided that double-precision solvers are employed and a sufficiently strict iterative convergence is achieved.

The objective of solution verification is therefore to estimate the discretization error associated with a given numerical solution and to express it in terms of a corresponding numerical uncertainty. This is achieved through systematic grid refinement studies, performed directly on the QoIs of interest. The procedure adopted in this work follows the methodology recommended by the ASME V&V 20 standard [11] and is based on the Grid Convergence Index (GCI) framework proposed by Roache [9]. The approach is applicable to different types of QoIs, including local values, spatial or temporal averages, and integral quantities. Since the error propagation depends on how the QoI is constructed from the solution fields, the verification process must be carried out directly on the selected QoIs rather than on the underlying variables. The estimation of numerical uncertainty is performed through the following five-step procedure:

1. Definition of a representative grid size for the quantities of interest.
2. Generation of a set of systematically refined computational grids.
3. Evaluation of the observed order of convergence p.
4. Estimation of the QoI value at infinitely refined grid using Richardson extrapolation.
5. Quantification of numerical errors and estimation of the numerical uncertainty using the Grid Convergence Index (GCI).

Representative grid size and refinement strategy

A representative grid size h_i must be defined for each grid level i, in a manner consistent with the spatial resolution relevant to the QoIs. The definition of h_i is problem-dependent and may reflect a global characteristic cell size or a directional resolution associated with dominant gradients. The refinement strategy should be designed to systematically reduce h_i while preserving mesh quality and topology as much as possible. The refinement ratio between two consecutive grids is defined as

$$r_{ji} = \frac{h_j}{h_i} \tag{2.3}$$

where i and j denote two grid levels, with i corresponding to the finer grid. A constant refinement ratio is generally preferred, although this condition may not always be strictly satisfied in complex geometries.

Observed order of convergence

For a set of at least three grids, the observed order of convergence p is evaluated as

$$p = \frac{1}{\ln(r_{21})}\left[\ln\left(\frac{\varepsilon_{32}}{\varepsilon_{21}}\right) + \ln\left(\frac{r_{21}^p - s}{r_{32}^p - s}\right)\right] \tag{2.4}$$

where the differences between grid solutions are defined as

$$\varepsilon_{ji} = \phi_j - \phi_i \tag{2.5}$$

and

$$s = \operatorname{sign}\left(\frac{\varepsilon_{32}}{\varepsilon_{21}}\right) \tag{2.6}$$

In the case of constant refinement ratio ($r_{32} = r_{21} = r$), the formulation simplifies accordingly. The evaluation of p is sensitive to both the refinement strategy and the solution behavior. Although the theoretical order of convergence p^{th} is determined by the numerical schemes employed, the observed value may deviate significantly in

practical applications. As a consistency check, the following empirical bound can be adopted [12]:

$$\frac{1}{2}p^{th} < p < \frac{4}{3}p^{th} \tag{2.7}$$

Values outside this interval may indicate non-asymptotic behavior, insufficient refinement, or localized solution irregularities.

Richardson extrapolation

When the observed order of convergence is deemed acceptable, an extrapolated value of the QoI corresponding to an infinitely refined grid can be estimated using Richardson extrapolation:

$$\phi_{ext}^{21} = \frac{r_{21}^{p}\phi_1 - \phi_2}{r_{21}^{p} - 1} \tag{2.8}$$

This value represents the best available estimate of the exact solution within the numerical framework and provides a reference for error estimation.

Error estimation and Grid Convergence Index

Based on the extrapolated value, the discretization error can be estimated in both absolute and relative form:

$$\varepsilon_{ext}^{21} = |\phi_{ext}^{21} - \phi_1| \tag{2.9}$$

$$\varepsilon_{ext}^{21} = \left| \frac{\phi_{ext}^{21} - \phi_1}{\phi_{ext}^{21}} \right| \tag{2.10}$$

An approximate error based on two consecutive grids is defined as

$$\varepsilon_{a}^{21} = |\phi_1 - \phi_2| \tag{2.11}$$

$$\varepsilon_a^{21} = \left| \frac{\phi_1 - \phi_2}{\phi_1} \right| \tag{2.12}$$

The Grid Convergence Index (GCI), introduced by Roache [9], provides a conservative estimate of the numerical uncertainty:

$$GCI_{21} = \frac{F_S \cdot \varepsilon_a^{21}}{r_{21}^p - 1} \tag{2.13}$$

where the safety factor F_S is typically set to 3 for two-grid comparisons, while a value of 1.25 is recommended for three-grid studies.

The numerical uncertainty associated with the QoI can be expressed as

$$u_{num} = \frac{GCI}{k} \tag{2.14}$$

where k is an expansion factor related to the assumed error distribution. In the absence of detailed statistical information, a conservative estimate is obtained by setting $k = 1$. The outcome of the solution verification process is therefore a quantitative estimate of the numerical uncertainty associated with each QoI. This information is subsequently used in the validation stage to assess the agreement between simulation results and reference data.

2.5 Validation and Comparison Strategies

Validation represents the second phase of the V&V process and aims at assessing the capability of the model to reproduce physical reality for the intended use. The assessment is based on the comparison between simulation results and reference data, and on the quantification of the associated discrepancies.

The fundamental quantity used to assess agreement is the *comparison error* (or validation error), defined as:

$$E = S - D \tag{2.15}$$

where S and D denote the simulated and measured values of the selected QoI, respectively. This quantity represents the observable discrepancy between model predictions and experimental evidence, and it does not directly correspond to a single source of error.

In general, the comparison error arises from the combined effect of different contributions associated with the numerical model, the input data, and the experimental measurements. This can be expressed in a general form as:

$$E = \delta_{model} + \delta_{num} + \delta_{input} + \delta_D \tag{2.16}$$

where δ_{model} represents the model form error (i.e., the discrepancy due to physical modeling assumptions), δ_{num} the numerical error, δ_{input} the uncertainty associated with input parameters, and δ_D the experimental measurement error.

From a practical standpoint, these contributions are not individually accessible, but their combined effect can be quantified through an uncertainty-based formulation. Following the ASME V&V 20 framework [11], the *validation uncertainty* is defined as:

$$u_{val} = \sqrt{u_{input}^2 + u_{num}^2 + u_D^2} \tag{2.17}$$

where each term represents the standard uncertainty associated with the corresponding contribution to the comparison error. This definition allows the comparison error to be interpreted in a probabilistic framework:

$$\delta_{model} \in E \pm u_{val} \tag{2.18}$$

providing a quantitative measure of the agreement between simulation and experiment.

Input uncertainty and sensitivity

Uncertainty in model inputs, including material properties, boundary conditions, and model parameters, contributes to the overall discrepancy between simulation and

experiment. Formally, the input uncertainty can be estimated using sensitivity-based approaches. Given a vector of input parameters

$$\vec{\zeta} = \{\zeta_1, \zeta_2, ..., \zeta_N\} \tag{2.19}$$

the associated uncertainty can be expressed, under a first-order approximation, as

$$u_{input}^2 = \sum_{i=1}^{N} \left(\frac{\partial S}{\partial \zeta_i} u_{\zeta_i} \right)^2 \tag{2.20}$$

where u_{ζ_i} is the uncertainty associated with the input parameter ζ_i, and $\partial S/\partial \zeta_i$ represents the sensitivity coefficient of the QoI with respect to that parameter. These coefficients can be estimated using finite-difference perturbations in the parameter space.

Despite its formal rigor, the explicit evaluation of u_{input} may become computationally prohibitive in practical CFD applications, particularly in multiphysics problems involving a large number of uncertain inputs. In such cases, simplified approaches are often adopted. A common strategy consists in treating input uncertainty as part of the overall modeling error, implicitly incorporating it into the model discrepancy.

Under this assumption, the validation uncertainty reduces to

$$u_{val}^{\star\,2} = u_{num}^2 + u_D^2 \tag{2.21}$$

This approach simplifies the analysis but requires careful interpretation, as the resulting discrepancy includes both modeling and input-related effects.

Experimental data uncertainty

The uncertainty associated with experimental measurements, u_D, represents the dispersion of the measured values due to limitations in instrumentation, data acquisition, and processing procedures. This contribution must be quantified according to established metrological standards and incorporated into the validation uncertainty. In practical applications, the availability and quality of experimental uncertainty data

may vary significantly. When uncertainty bounds are explicitly provided, they can be directly included in the validation framework. Otherwise, reasonable estimates based on experimental practice or literature sources may be adopted, with appropriate caution in the interpretation of the results.

Validation in the absence of experimental data

In the absence of experimental data, a direct validation of the numerical model cannot be performed. In this context, comparisons with results obtained from other numerical models or software are sometimes employed to provide additional insight into the behavior of the solution. However, it is important to emphasize that such code-to-code comparisons do not constitute validation in a strict V&V sense. Validation requires the assessment of model predictions against independent experimental measurements. Comparing results obtained from different numerical tools may highlight discrepancies related to numerical implementation, discretization schemes, or modeling assumptions, but it does not provide information on the correctness of the underlying physical model. Agreement between different codes may simply indicate consistency in the implementation of similar assumptions, rather than accuracy with respect to reality.

Nevertheless, code-to-code comparisons can still be useful within the broader model assessment process. When one of the reference models has been previously validated against experimental data under similar conditions, the comparison may provide indirect confidence in the results, although this remains conditional and cannot replace a rigorous validation exercise.

In the present work, this approach is adopted in the PEM fuel cell case, where, in addition to validation against experimental data, a code-to-code comparison is performed to further assess the consistency and robustness of the numerical predictions. Therefore, code-to-code comparisons are interpreted as a qualitative consistency check rather than as a validation step, and their outcomes are discussed accordingly.

Distinction between validation and calibration

A fundamental distinction must be made between validation and calibration. Calibration consists in adjusting model parameters to improve agreement with a specific dataset, typically by minimizing the discrepancy E. While calibration can enhance the predictive capability of a model under conditions similar to those used for tuning, it does not constitute validation. Validation, on the other hand, requires an independent assessment of the model against data that have not been used during parameter adjustment. As highlighted in the ASME standards [11], a model that reproduces a calibrated dataset with high accuracy may still lack predictive capability under different operating conditions.

This distinction is particularly relevant in complex multiphysics simulations, where multiple parameters may be tuned simultaneously.

Chapter 3

Pure hydraulic model of a Triply Periodic Minimal Surface

This chapter presents the application of the V&V methodology to a simplified CFD problem characterized by a single, well-defined Quantity of Interest (QoI): the pressure drop across a porous structure. The objective is not to develop a fully predictive model of a complex system, but to assess the reliability of numerical results used to support the derivation of semi-empirical correlations. The case study focuses on a Triply Periodic Minimal Surface (TPMS) geometry, for which the relationship between mass flow rate and pressure drop represents one of the key design parameters. In this context, CFD is employed to complement experimental data and extend the range of operating conditions. The credibility of the numerical model is therefore directly linked to its ability to provide consistent estimates of the pressure losses. The purpose of this chapter is to evaluate whether the numerical uncertainty associated with the CFD model remains sufficiently small compared to the variability of the experimental data, ensuring that the model can be reliably used within its intended scope. The analysis therefore provides a baseline example of credibility assessment in a controlled setting, where the impact of individual uncertainty sources can be clearly identified and interpreted.

3.1 Problem Definition and Intended Use

The case study addresses the numerical analysis, verification and validation of a 3D CFD model of a Triply Periodic Minimal Surface (TPMS) sample tested in Politecnico di Milano laboratories. TPMS structures are periodic three-dimensional surfaces characterized by zero mean curvature and continuous topology, which can be exploited to generate highly interconnected porous media with favorable transport properties [13–15].

In recent years, TPMS-based geometries have attracted increasing interest in heat transfer applications due to their high surface-to-volume ratio, smooth curvature, and absence of sharp edges, which promote efficient thermal exchange while limiting pressure losses [16–19]. The adoption of additive manufacturing (AM) techniques has further enabled the realisation of such complex structures at laboratory and industrial scale [20, 21]. Among the different TPMS structures, some of which are shown in fig. 3.1, the present work focuses on the gyroid one [14, 22, 23] as representative geometry for the development of compact heat exchanger concepts.

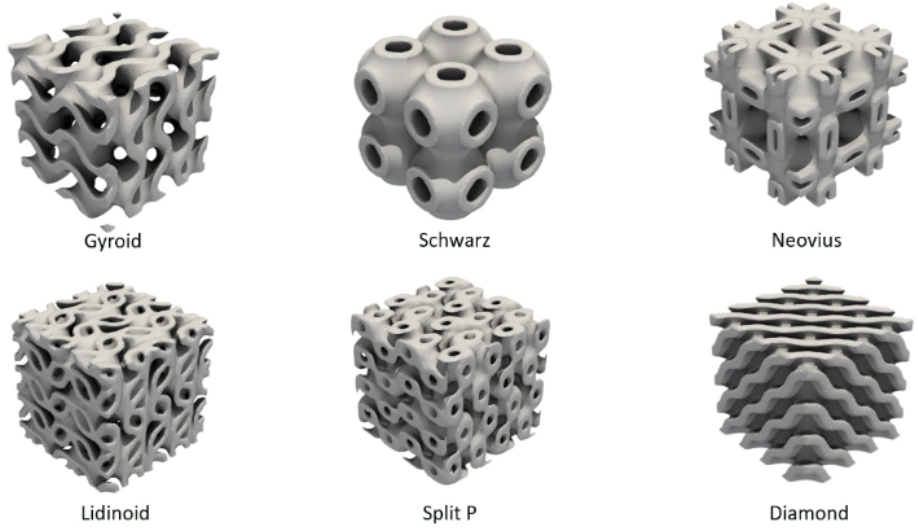


Fig. 3.1 Examples of different triply periodic minimal surface (TPMS) unit cell structures; this study focuses on the analysis of the gyroid one.

The analysis focuses on the hydraulic response of the structure under steady-state flow conditions, with the pressure drop across the sample identified as the sole Quantity of Interest. This choice reflects the role of the present model within a wider experimental campaign, where CFD is employed to complement laboratory

measurements in the construction of semi-empirical correlations [24]. Accordingly, the intended use of the model is not high-fidelity prediction of local flow features, but the generation of consistent and reliable data for correlation development over a range of operating conditions. In this context, the primary requirement is that numerical errors remain controlled and well-characterized, so as not to introduce systematic bias in the derived relationships. Given the predominantly laminar regime and the absence of additional physical couplings, the problem provides a simplified yet rigorous testbed for the application of the V&V methodology, in line with previous studies on TPMS structures [22, 23]. The analysis therefore emphasizes solution verification and uncertainty quantification, enabling a transparent assessment of model credibility with respect to its intended use.

3.2 Numerical Model Description

The computational domain reproduces the experimental test section adopted for the hydraulic characterization of the TPMS sample, consistent with previous experimental and numerical investigations on similar structures [21, 24]. A schematic representation of the full CFD domain is reported in fig. 3.2.

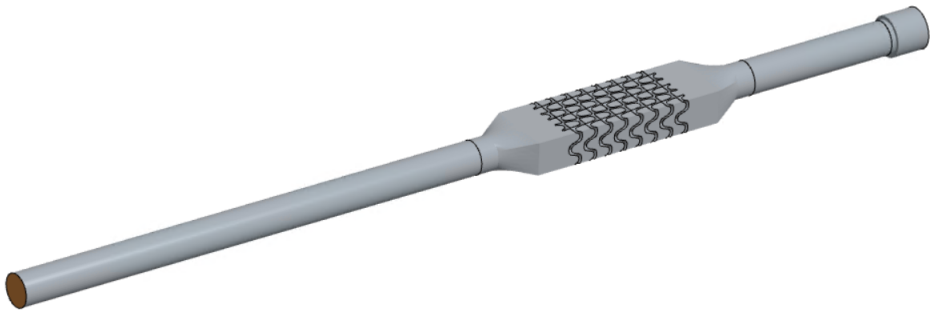


Fig. 3.2 CAD representation of the computational domain, including inlet section, TPMS core, and outlet extrusion.

The domain consists of three main regions. An inlet pipe section is included to reproduce the experimental feeding line, followed by a contraction connecting the inlet diameter to the TPMS core. This geometric transition ensures consistency with the experimental configuration and allows the same flow development before entering the porous structure. At the core of the domain, the gyroid TPMS structure is embedded within a parallelepiped volume and represents the actual test sample re-

sponsible for the dominant hydraulic resistance. The TPMS sample is manufactured in resin via additive manufacturing, as in the experimental campaign. Its morphology can be characterized through the porosity, defined as

$$\varepsilon = \frac{V_f}{V_{tot}} \tag{3.1}$$

where V_f is the fluid volume and V_{tot} is the total volume of the TPMS domain. Three different orientations of the gyroid structure are considered, corresponding to 0°, $+45^\circ$, and -45° rotations with respect to the main flow direction, as shown in fig. 3.3. This allows assessing the influence of geometric anisotropy on the hydraulic response.

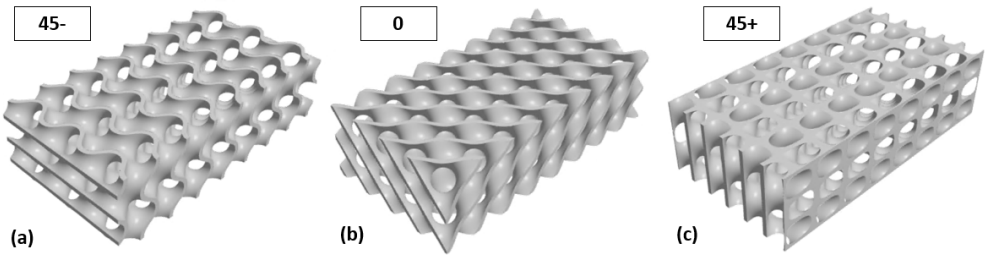


Fig. 3.3 Different orientations of the gyroid TPMS structure tested in the experimental setup and analyzed in this study: (a) -45°, (b) $+45^\circ$, and (c) 0°.

Downstream of the TPMS, an outlet extrusion is introduced as a standard CFD practice to minimize the influence of the outlet boundary condition on the solution and to improve numerical stability and convergence. The inlet and outlet diameters are equal to 5 mm, consistently with the experimental setup. The inclusion of inlet and outlet extensions ensures that the pressure drop is evaluated under conditions consistent with the experimental measurement procedure.

The working fluid is air, and the flow rate is controlled through a mass flow controller, allowing for accurate regulation of the inlet conditions. The operating range is selected to cover Reynolds numbers up to approximately 150, ensuring that the flow remains well within the laminar regime. In particular, the investigated conditions span a range of Reynolds numbers between 0 and 100, for which inertial effects are limited and the flow is expected to be predominantly viscous-dominated. The outlet boundary condition corresponds to ambient pressure. The flow regime is characterized through a Reynolds number defined on the basis of a characteris-

tic length scale representative of the TPMS structure. In porous geometries, the Reynolds number can be expressed as

$$Re = \frac{\rho U D_h}{\mu} \tag{3.2}$$

where ρ is the fluid density, U is a characteristic velocity based on the superficial flow rate, μ is the dynamic viscosity, and D_h is an equivalent hydraulic diameter of the porous structure, defined as

$$D_h = \frac{4V_{\text{fluid}}}{A_{\text{wetted}}} \tag{3.3}$$

as commonly adopted for porous media such as TPMS structures [14, 15]. For the investigated operating conditions, the resulting Reynolds number range falls entirely within the laminar regime. This simplifies the modeling assumptions and allows focusing on numerical aspects without introducing turbulence modeling uncertainties. From the numerical standpoint, simulations are performed using STAR-CCM+ in double precision. The flow is assumed steady, incompressible, and isothermal, with constant fluid properties corresponding to the experimental conditions. No heat transfer is modeled, due to the absence of thermal sources or sinks in the experimental configuration. Moreover, given that the pressure drops in the system are of the order of a few hundred Pascals, fluid properties can be safely considered constant. Due to the geometric complexity of the TPMS structure, the computational mesh is generated using unstructured polyhedral cells, allowing an efficient discretization of highly curved surfaces while maintaining a reasonable number of volumetric cells. Mesh refinement is applied in regions characterized by reduced cross-sectional area and high curvature to ensure adequate resolution of velocity gradients and pressure losses. Boundary conditions are imposed consistently with the experimental setup: a constant mass flow rate is applied at the inlet, while a uniform fixed static pressure is imposed at the outlet. No-slip conditions are enforced on all solid walls. This numerical setup provides the basis for the subsequent application of verification and validation procedures, with particular focus on the quantification of discretization uncertainty affecting the pressure drop prediction.

3.3 Application of the V&V Methodology

The verification and validation procedure described in Chapter 2 is applied to assess the reliability of the numerical model used to predict the pressure drop across the TPMS sample for the three investigated orientations (0°, +45°, −45°). Code verification is not addressed, as the simulations are performed using the commercial software STAR-CCM+, which is assumed to be previously verified. The analysis therefore focuses on solution verification and validation.

Quantity of interest The QoI is the pressure drop across the sample, Δp, evaluated between two locations corresponding to the positions of the experimental pressure transducers. The same locations are used in the CFD model, as illustrated in Fig. 3.4, where the probes are highlighted. In order to assess the sensitivity of the QoI to the post-processing procedure, the pressure values at the probe locations are extracted using three different approaches: point-wise values, volume-averaged values over a spherical region of 0.1 mm radius centered at the probe location, and surface-averaged values over the corresponding cross-sectional sections. All three methods yield consistent results, indicating that the evaluation of the pressure drop is not affected by the specific extraction technique. The QoI is computed for all three TPMS orientations and for the range of Reynolds numbers investigated experimentally.

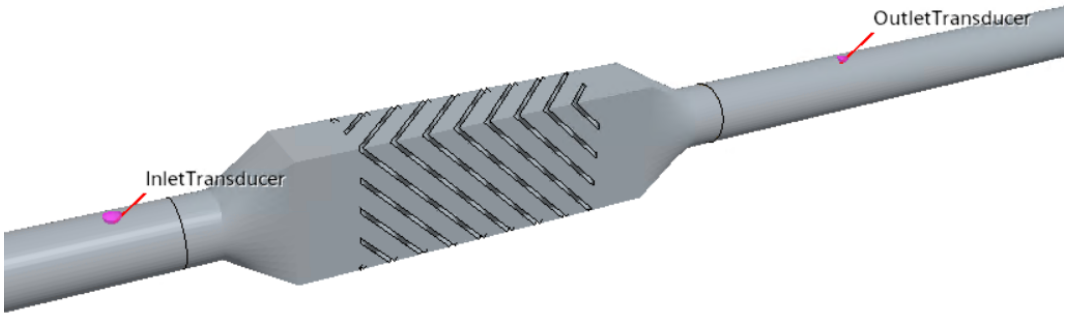


Fig. 3.4 Pressure probe locations highlighted in purple, corresponding to the positions of the experimental pressure transducers. Pressure values are extracted using point-wise, volume-averaged (0.1 mm spherical region), and surface-averaged approaches, all providing consistent results.

Solution Verification Solution verification is performed through a systematic grid refinement study following the methodology described in Chapter 2. A sequence of five progressively refined meshes is generated by adapting the mesh parameters while preserving the overall topology.

The representative grid size is defined as:

$$h = \left(\frac{V}{N}\right)^{1/3} \tag{3.4}$$

where V is the total fluid volume and N is the number of volumetric cells in the sample. The characteristics of the grids are reported in Table 3.1 while a qualitative overview of the mesh structure is shown in fig. 3.5.

Table 3.1 Grid refinement study for the TPMS case for three orientations ($-45°$, $0°$, $+45°$).

Orientation	**Grid**	**Cells** ($\times 10^6$)	h **(mm)**	r **(-)**
$-45°$	G1	4.3	6.1	1.18
	G2	2.2	7.6	1.27
	G3	1.4	9.0	-
$0°$	G1	2.5	7.3	1.10
	G2	1.9	8.0	1.41
	G3	0.7	11.3	-
$+45°$	G1	5.0	5.8	1.41
	G2	1.8	8.2	1.34
	G3	0.7	11.0	-

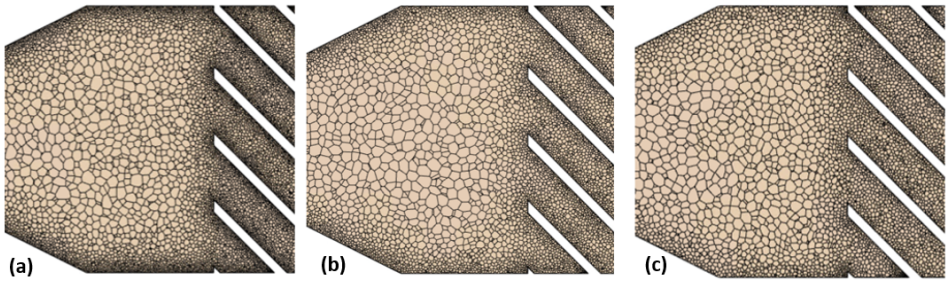


Fig. 3.5 Different mesh refinement displayed on a cross-sectcion of the TPMS sampling (-45° orientation) from finest (a) to coarsest (c).

The discretization error is quantified using the five-step procedure applied on the highest Reynolds condition of the investigated range, including the estimation of the observed order of convergence, Richardson extrapolation, and the computation of

the Grid Convergence Index (GCI). The results are reported in Table 3.2, where the metrics are provided separately for each TPMS orientation.

Table 3.2 Metrics of the 5-step solution verification procedure for the pressure drop across the TPMS sample.

Metric	-45°	0°	$+45^\circ$
p_{123} (-)	1.1	2.6	2.3
ϕ_{ext} (Pa)	29.4	34.2	42.0
ε_{ext} (%)	3.3	2.4	3.0
ε_{21} (%)	0.9	0.7	3.7
GCI_{21} (%)	4.2	3.1	3.9

The results indicate a consistent convergence behavior across the investigated grids. Iterative and round-off errors are considered negligible due to strict convergence criteria and the use of double precision respectively.

Validation and Uncertainty Quantification Validation is carried out by comparing the numerical predictions of the pressure drop with the available experimental measurements. In order to assess the robustness of the model with respect to operating conditions, a sensitivity analysis is performed on the inlet mass flow rate by introducing a perturbation of $\pm 5\%$ around the nominal value. This results in a variation of the predicted pressure drop of approximately 7.5%, evaluated according to eq. (2.20).

The contribution associated with experimental measurements is quantified based on the analysis reported in [24, 21], leading to an estimated uncertainty of 3.5% on the pressure readings.

The comparison between numerical and experimental results is therefore interpreted in terms of the validation error E together with its associated uncertainty bounds. Clear differences in the level of agreement are observed among the three TPMS orientations, namely 0°, 45^+, and 45^-, and these trends are further discussed in the following section.

In line with the adopted V&V methodology, graphical comparisons between CFD results and experimental data are not considered sufficient for validation purposes and are therefore not used as the primary validation metric. The assessment is instead based on the quantitative evaluation of the comparison error and its associated

Table 3.3 Validation uncertainty and comparison error for the pressure drop across the TPMS sample.

Metric	-45°	0°	$+45^\circ$
u_{num} (%)	4.2	3.1	3.9
u_D (%)	4.2	4.2	4.0
u_{input} (%)	3.1	3.4	3.4
u_{val} (%)	6.7	6.2	6.5
ϕ_{exp} (Pa)	28.1	29.5	33.1
ϕ_{CFD} (Pa)	28.2	33.2	39.3
E (Pa)	0.1	3.7	6.1
E (%)	0.3	12.5	18.4

uncertainty. Figure 3.6 reports the validation error for the three TPMS orientations. The results corresponding to the 45^+ orientation are shown in blue, those for the 0° configuration in green, and those for the 45^- orientation in red. The error bars represent the validation uncertainty discussed in Chapter 2.

3.4 Model Credibility and Discussion

Within the V&V framework, the results presented in the previous section are interpreted in light of the intended use of the model, which is the development of an empirical correlation for pressure drop across TPMS structures.

As discussed in Chapter 2, validation does not lead to a binary statement regarding the correctness of the model. Instead, model credibility is assessed by comparing the validation error with its associated uncertainty and by evaluating whether the resulting level of confidence is adequate for the intended application. For the present case, the comparison error exhibits different behaviors depending on the TPMS orientation. For the -45° configuration, the agreement is generally satisfactory over the investigated range, with modeling errors remaining below approximately 15% except at the lowest Reynolds numbers, where the relative error increases markedly. The 0° configuration shows slightly larger discrepancies, generally in the range of 10% to 25%, while maintaining a similar trend with increasing Reynolds number. The $+45^\circ$ configuration exhibits the largest discrepancies among the three orientations, with errors systematically higher over the investigated range and maximum values exceeding 30%. These differences indicate that the model performance is

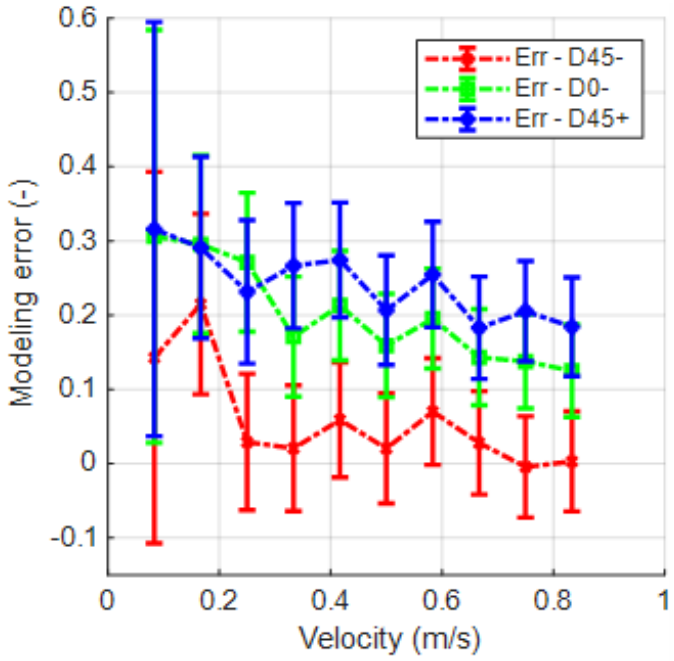


Fig. 3.6 Validation error δ_{model} for the three TPMS orientations (0°, 45^+, 45^-). The colored markers indicate the numerical results for each configuration (blue: 45^+, green: 0°, red: 45^-), while the error bars represent the associated validation uncertainty.

not independent of the orientation of the TPMS structure and should therefore be considered separately for each configuration.

From a physical standpoint, the observed discrepancies may be attributed to multiple factors. In particular, the manufacturing process based on additive manufacturing introduces uncertainties in the internal geometry, including surface roughness, local defects, and deviations from the nominal porosity [20, 21, 25]. These effects are not captured in the numerical model, which assumes an ideal geometry. The higher discrepancy observed for the $+45°$ configuration may therefore be associated with orientation-dependent manufacturing imperfections. However, in the absence of direct measurements of the manufactured geometries, this interpretation remains a possible explanation rather than a demonstrated cause of the observed discrepancies. Further experimental investigations could therefore be beneficial, for instance by testing multiple samples with identical orientation or by characterizing the manufactured geometries through direct dimensional measurements, in order to isolate the effect of geometric variability.

At very low Reynolds numbers, the increase in the comparison error indicates a loss of agreement between numerical predictions and experimental measurements, with modeling errors reaching values up to 60%. In this regime, the pressure drop becomes very small in absolute terms, and its experimental determination is inherently more challenging. As a consequence, measurement uncertainties and instrumentation limits may play a significant role, potentially leading to larger relative errors in the experimental data. From the numerical standpoint, the flow approaches a creeping regime dominated by viscous effects, where the pressure drop is sensitive to geometric details and boundary conditions. However, given the magnitude and trend of the discrepancies, it is likely that the observed deviations cannot be attributed solely to modeling assumptions, but also to limitations in the experimental measurements at very low flow rates. From a V&V perspective, this highlights an important aspect: large comparison errors do not necessarily imply a lack of model fidelity, but may also reflect increased uncertainty in the reference data. In such conditions, the interpretation of validation results must be performed with caution, and the credibility of the model should be assessed primarily in the range of operating conditions where both numerical and experimental uncertainties remain controlled.

From the perspective of the intended use, the objective is not to achieve exact agreement with experimental data, but to ensure that the modeling error remains within acceptable bounds for the development of reliable pressure drop correlations. In this context, the validation results provide a clear quantitative indication of the model performance. Excluding the low-Reynolds-number regime, where larger discrepancies are observed, the -45° configuration shows modeling errors consistently below 15%, indicating a good agreement between numerical predictions and experimental measurements. The 0° configuration exhibits slightly higher deviations, with modeling errors generally in the range of 10% to 25%, but still within a range that can be considered acceptable for engineering correlation development. These results suggest that, for the majority of the operating conditions of practical interest, the model is capable of capturing the dominant flow physics governing the pressure drop across the TPMS structures.

An important outcome of this study is that the V&V process enables not only the quantification of uncertainty, but also the identification of potential inconsistencies between the numerical model and the physical system. In the present case, the analysis indicates that part of the discrepancy may originate from the experimental side,

potentially including geometric deviations introduced by the additive manufacturing process, rather than from deficiencies in the numerical formulation alone. Given the relatively low cost and flexibility of manufacturing additional samples, further experimental campaigns could be designed to better characterize this variability and to decouple geometric uncertainties from modeling errors. This highlights the role of CFD, when supported by a rigorous V&V framework, not only as a predictive tool but also as a means to support the interpretation and assessment of experimental data. Overall, the model can be considered credible for its intended use, namely the development of semi-empirical correlations for pressure drop in TPMS structures. The level of agreement achieved, combined with the explicit quantification of uncertainties, provides a sufficient degree of confidence for engineering applications, while also clearly identifying the limits within which the model predictions should be interpreted.

Chapter 4

Thermo-Fluid Dynamic Model of a V-Rib turbulence promoter

This chapter presents the application of the V&V methodology to a more complex CFD problem, characterized by multiple interacting physical phenomena and a larger set of QoIs. In contrast to the previous case study, which focused on a purely hydraulic behavior, the present analysis involves a thermo fluid dynamic problem where turbulence and heat transfer mechanisms play a central role. The case study focuses on a ribbed cooling channel equipped with V-shaped turbulence promoters, called V-ribs, representative of advanced cooling solutions for components that operate under high heat flux conditions, such as the cooling system of the Helium Cooled Pebble Bed First Wall (HCPB-FW) of a future fusion reactor. A sketch of the prototypical mock-up of the cooling system is reported in fig. 4.1 along with the V-rib turbulent promoter structures.

The V-ribs enhance the heat transfer by periodically disrupting the boundary layer, promoting flow recirculation and increasing mixing within the channel. However, these benefits come at the cost of increased pressure losses, making the accurate prediction of both thermal and hydraulic performance essential for design purposes. From a modeling perspective, the problem is more demanding than the TPMS case. The flow is fully turbulent and the results are sensitive to the choice of turbulence closure. In addition, conjugate heat transfer between the fluid and the solid domain is considered, introducing further sources of uncertainty related to thermal boundary conditions and material properties. As a consequence, the V&V process must account

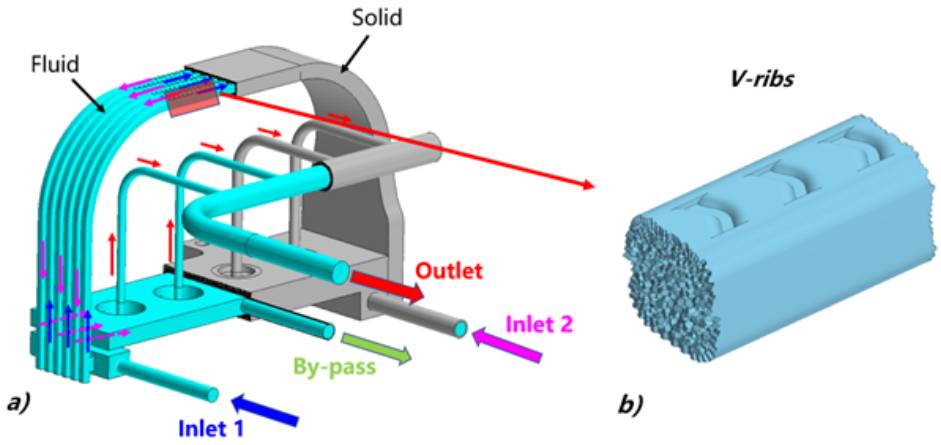


Fig. 4.1 Schematic representation of the prototypical mock-up of the HCPB First Wall cooling system (left) and detail of the V-rib turbulence promoter geometry (right), highlighting the rib arrangement along the heated wall of the channel.

not only for numerical errors, but also for modeling uncertainties associated with turbulence and heat transfer.

4.1 Problem Definition and Intended Use

The analysis is structured in two complementary parts. First, a grid convergence study is performed on a reduced computational domain consisting of a single periodic unit of the ribbed channel. This simplified configuration allows isolating discretization effects and quantifying the numerical uncertainty affecting the selected QoIs: pressure drop, maximum velocity within the domain and temperature increase. The outcome of this step is the identification of a grid providing an optimal balance between accuracy and computational cost, together with an estimate of the associated numerical uncertainty.

In the second part, the numerical model is applied to a full-scale configuration reproducing the experimental setup of the HETREX test campaign. In this case, the objective shifts from verification to validation, and the CFD results are compared against experimental measurements of temperature and pressure along the channel. Two different turbulence models are considered, namely the Lag-Elliptic Blending (Lag-EB) model and the Reynolds Stress Model (RSM), in order to assess the impact of turbulence closure on the predicted quantities.

The intended use of the numerical model is twofold. On one hand, it aims at providing a consistent description of the coupled flow and heat transfer mechanisms within the ribbed channel, with particular attention to the interaction between turbulence, recirculation, and thermal boundary layers. On the other hand, it is used to support the interpretation of experimental data and to evaluate the impact of modeling choices, especially in relation to turbulence closure and thermal boundary conditions. In this context, the V&V process is used to quantify both numerical and modeling uncertainties affecting the QoIs. While discretization errors are addressed through the grid convergence study, additional uncertainty sources arise from the turbulence modeling and from the assumptions on the thermal boundary conditions, which are not directly measured in the experiments. The results of the verification step are therefore propagated to the validation analysis in the form of uncertainty bounds, enabling a consistent and quantitative comparison between numerical predictions and experimental data.

The transfer of the numerical uncertainty from the periodic verification domain to the full HETREX-PT configuration is based on the assumption that the spatial discretization error is primarily governed by the local numerical resolution of the relevant physical phenomena, rather than by the overall extent of the computational domain. The periodic domain preserves the same channel cross-section, V-rib geometry, near-wall treatment, turbulence models, and conjugate heat transfer formulation adopted in the full-scale model. It therefore provides a representative sub-domain in which the sensitivity of the QoIs to spatial resolution can be assessed while avoiding additional effects associated with the inlet and outlet regions. Under these assumptions, the numerical uncertainty estimated from the periodic configuration is considered representative of the discretization uncertainty of the corresponding physical model when applied to the full HETREX-PT geometry. The uncertainty obtained from the verification study is consequently propagated to the validation analysis, while the additional effects associated with the full geometry are considered as part of the model-form and experimental uncertainties rather than as a separate discretization contribution.

4.2 Numerical Model Description

From a physical point of view, the presence of the V-ribs strongly affects the structure of the boundary layer. As a matter of fact, the ribs periodically interrupt the development of the near-wall region, inducing flow separation, reattachment, and secondary recirculation zones. This mechanism enhances mixing and reduces the thickness of the thermal boundary layer, leading to a higher global heat transfer coefficient. The side effects of such structures are increased pressure losses and enhanced turbulence production. The accurate prediction of such physics requires an appropriate modeling of both turbulence and boundary layer phenomena. The flow regime is characterized by Reynolds numbers based on the hydraulic diameter of the channel and bulk velocity, in the order of $Re = 10^5$, thus justifying the adoption of turbulence models. The numerical analysis is based on the HETREX-PT experimental campaign [26], which provides high-resolution data for pressure drop and heat transfer in rib-roughened channels representative of helium-cooled first wall concepts. The experiments were conducted on single-channel stainless steel test sections equipped with distributed thermocouples and subjected to controlled electrical heating via cartridge heaters. Flow conditions were scaled to reproduce Reynolds similarity between pressurized helium operation and atmospheric air tests, allowing a consistent comparison of different rib configurations in terms of thermal-hydraulic performance.

The CFD simulations are performed using STAR-CCM+ [27] in steady-state conditions with a segregated solver. Helium is modeled using a real gas approach based on the Van der Waals equation of state, while a turbulent Prandtl number equal to 0.9 is adopted, in accordance with standard CFD practice. The near-wall treatment and turbulence closures are selected according to the STAR-CCM+ theory guide [27], which provides the theoretical and numerical formulation of the implemented models. The flow is assumed fully turbulent throughout the domain. Two different turbulence closure models are considered.

The first is the κ-ε Lag-Elliptic Blending (Lag-EB) model, which extends the standard eddy-viscosity framework by introducing an additional transport equation for the redistribution of turbulent stresses. In this formulation, the classical Boussinesq hypothesis is relaxed through a lag term that accounts for the delayed response of Reynolds stresses to mean strain variations, improving the prediction of flows with strong curvature, separation, and reattachment. The elliptic blending function further

allows a smooth transition between near-wall and core-flow regions, making the model particularly robust in complex wall-bounded configurations while maintaining a relatively low computational cost.

The second model is the Reynolds Stress Model (RSM), in which a transport equation is solved for each component of the Reynolds stress tensor. This approach enables a more accurate description of turbulence anisotropy, which is particularly relevant in complex geometries with strong secondary flows, such as ribbed channels. Unlike eddy-viscosity models, the RSM does not rely on the isotropy assumption of turbulent stresses, but directly resolves their directional evolution, including production, redistribution, and dissipation mechanisms. This makes the model better suited for flows involving strong streamline curvature, rotation, and separation, at the expense of higher computational cost and increased numerical stiffness, as well as more demanding convergence behavior and boundary condition specification [27].

The computational domain adopted for the analysis is shown in Fig. 4.2. A single periodic unit of the V-ribbed channel is considered, including both the fluid and solid regions, together with the imposed thermal load at the heated wall. In order to reduce the computational effort, only half of the physical domain is simulated, exploiting geometric symmetry with respect to the vertical mid-plane of the channel. This assumption is consistent with the geometry and boundary conditions of the problem and allows a substantial reduction in the number of control volumes without affecting the physical accuracy of the solution.

A preliminary isothermal CFD setup is performed to replicate the hydraulic conditions of the experimental campaign. This configuration is consistent with the HETREX-PT methodology, where pressure drop and velocity fields are first characterized independently of thermal effects. The resulting fully developed velocity profile is then mapped as inlet condition for the conjugate heat transfer simulation, ensuring consistency with the experimental flow development conditions. The present numerical setup provides the basis for the subsequent application of the V&V methodology, where both discretization and modeling uncertainties are quantified with respect to the selected QoIs.

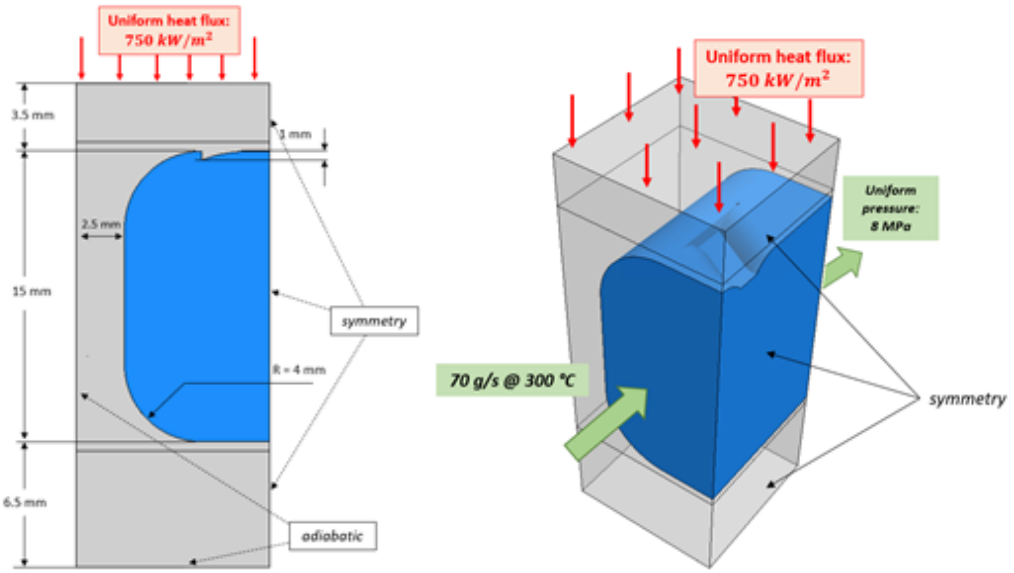


Fig. 4.2 Geometry (a) and boundary conditions (b) of the computational domain of a single step of V-rib, including the applied heat flux and characteristic dimensions of the periodic unit.

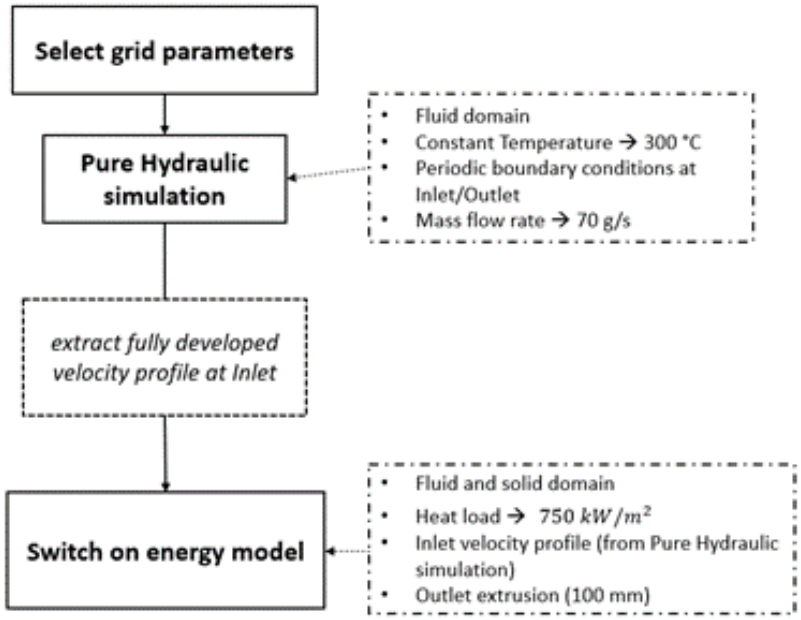


Fig. 4.3 Flow-chart illustrating the numerical workflow adopted for grid independence assessment and thermo-hydraulic simulation sequence.

4.3 Application of the V&V Methodology

The V&V methodology described in Chapter 2 is here applied to the thermo-fluid dynamic problem which is characterized by multiple QoIs. As in the previous case, code verification is not addressed thus the analysis focuses on solution verification and, in a second step, on validation against experimental data. On the other hand, the present study involves both fluid and solid domains, turbulence modeling, and conjugate heat transfer. As a consequence, the verification process must account for multiple quantities of interest and for the interaction between thermal and hydraulic phenomena.

Quantities of Interest Three QoIs are considered in the grid convergence study:

- the pressure drop across a single V-rib periodic unit, ΔP,
- the maximum velocity in the fluid domain, $v_{\max}$,
- the temperature increase of both fluid and solid domains, defined as $\Delta T = T_{\max} - T_{\text{inlet}}$.

These quantities are selected to capture both hydraulic and thermal aspects of the problem, and to assess the sensitivity of the numerical solution to grid refinement under different physical mechanisms.

Solution Verification The computational mesh is generated using polyhedral cells for the fluid domain and prism layers for the near-wall region. The boundary layer discretization is designed to ensure $y^+ \leq 1$ throughout the domain, with at least four prism layers at the wall. The resulting mesh parameters are:

- First prism layer height: 1.0×10^{-6} m,
- Total prism layer thickness: 8.0×10^{-5} m.

The fluid mesh is locally refined in the proximity of the V-ribs to better resolve turbulence structures, while the solid domain is divided into three regions. The top and bottom regions are meshed through extrusion, whereas the central region, in

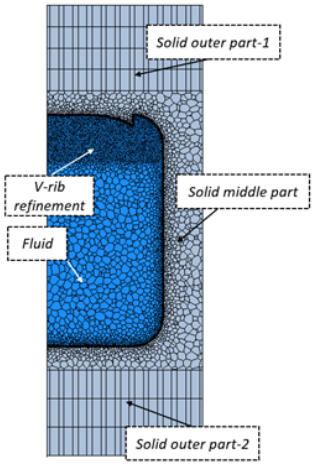


Fig. 4.4 Domain cross-section highlighting different grid refinement in the fluid and solid regions.

contact with the fluid, is discretized using polyhedral cells to ensure conformity at the interface. The computational gird is reported in Fig. 4.4.

The grid refinement study is performed using five computational grids, generated by progressively refining the base size, the number of prism layers, and the local refinement in the V-rib region. The total number of cells ranges from approximately 0.2 to 4.0 million cells. A qualitative comparison of the grid sequence is shown in Fig. 4.5, while the main mesh parameters are summarized in Table 4.1.

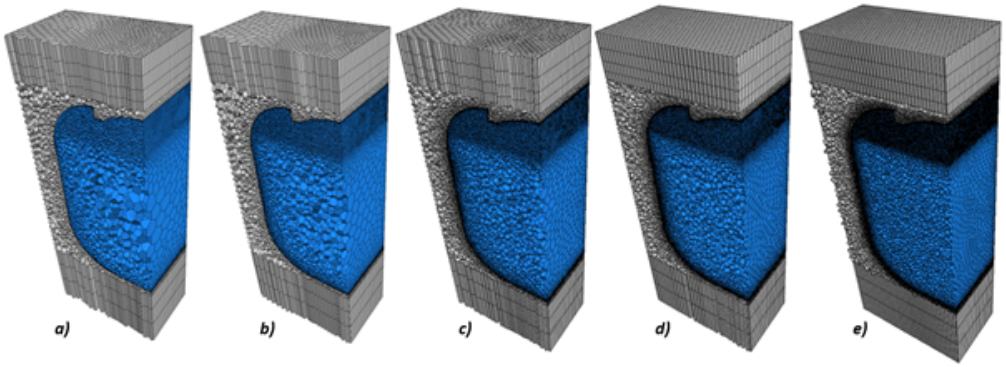


Fig. 4.5 Section view of the computational grids from the coarsest (a) to the finest (e).

The verification is performed on the periodic domain because the objective of this analysis is to isolate the effect of spatial discretization while retaining the same local thermo-fluid dynamic physics of the full configuration. Since the periodic domain contains the same V-rib geometry, near-wall treatment, turbulence closures,

Table 4.1 Mesh parameters for the grid refinement study.

	(a)	(b)	(c)	(d)	(e)
Base size solid (mm)	0.5	0.4	0.3	0.225	0.175
Base size fluid (mm)	0.4	0.3	0.2	0.16	0.12
Prism layers (-)	4	6	8	10	10
Refinement V-rib (mm)	0.13	0.10	0.10	0.08	0.05
Fluid cells (M)	0.17	0.43	0.91	1.79	3.60
Solid cells (M)	0.04	0.05	0.12	0.17	0.43
Total cells (M)	0.21	0.48	1.03	1.96	4.03

and conjugate heat transfer formulation as the HETREX-PT model, the resulting grid sensitivity is considered representative of the discretization behaviour of the full configuration.

The discretization uncertianties are quantified using the five-step procedure described in Chapter 2. The grid convergence behavior is analyzed, qualitatively, by expressing each QoI as a function of the representative grid size h normalized to the finest grid size h_a. The results are reported in fig. 4.6–4.8, where the numerical solutions obtained on the different grids are plotted against h. For each QoI, the value at $h = 0$ is obtained through Richardson extrapolation using the three finest grids, and represents an estimate of the grid-independent solution. In the figures, the blue curves refer to the Lag-EB turbulence model, while the red curves correspond to the RSM model.

The results show a general decrease of numerical error with mesh refinement, although non-monotonic behavior is observed in some cases due to variations in the location of peak values. The hydraulic quantities (velocity and pressure drop) exhibit lower sensitivity to grid refinement when using the Lag-EB model (errors within $\sim 5\%$), while larger discrepancies are observed with the RSM model. Conversely, the temperature predictions are more stable when using RSM.

Based on this analysis, the intermediate grid (approximately 1 million cells) is selected as a compromise between accuracy and computational cost. The numerical uncertainty associated with this grid is evaluated by combining the Grid Convergence Index with the relative grid error, according to:

$$\Phi_j = \phi_j \pm (u_{\text{num}} + \text{err}_{\text{grid},j} \cdot \phi_j) \tag{4.1}$$

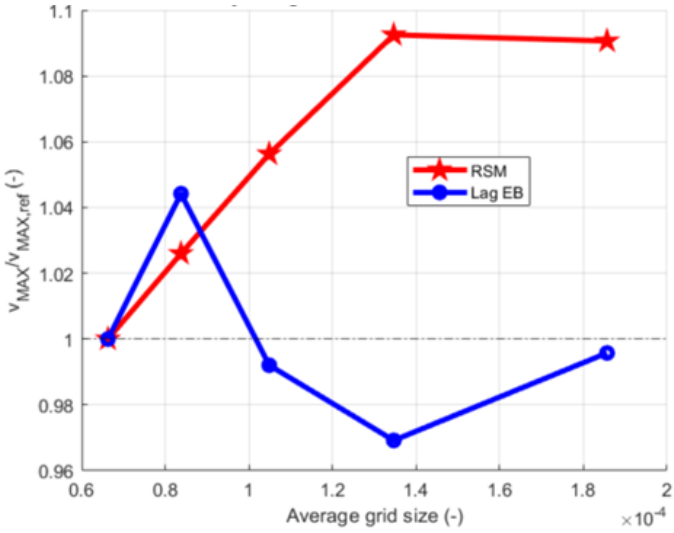


Fig. 4.6 Grid convergence of the maximum velocity for different turbulence models. The red line refers to the RSM model, while the blue line corresponds to the Lag-EB model.

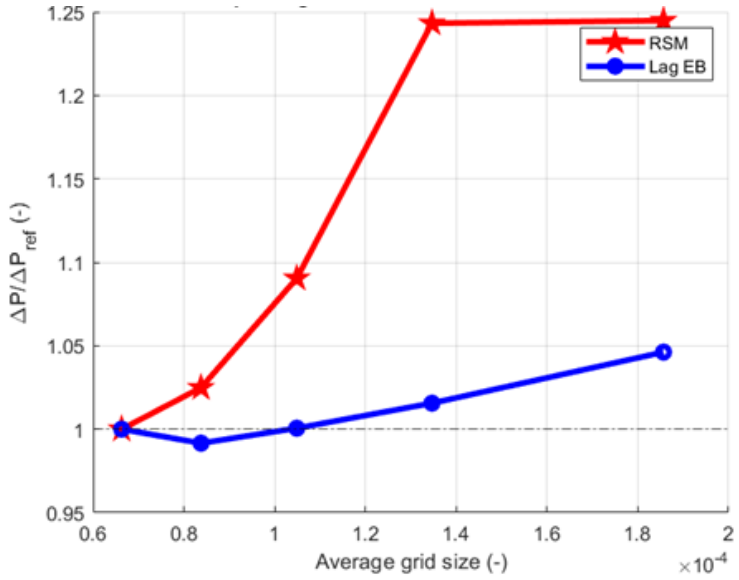


Fig. 4.7 Grid convergence of the pressure drop for different turbulence models. The red line refers to the RSM model, while the blue line corresponds to the Lag-EB model.

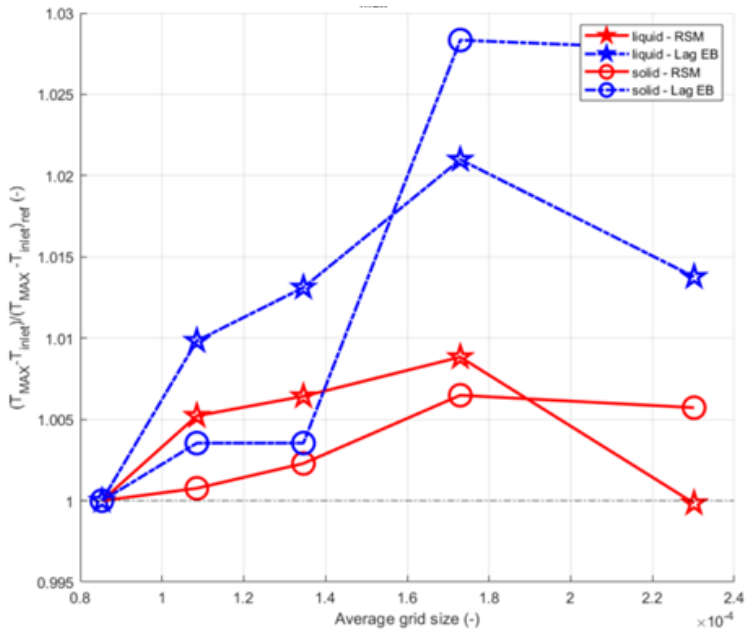


Fig. 4.8 Grid convergence of the temperature increase for different turbulence models. The red line refers to the RSM model, while the blue line corresponds to the Lag-EB model.

where u_{num} is derived from the GCI and $\text{err}_{\text{grid},j}$ represents the relative error with respect to the finest grid. The resulting uncertainties for the selected grid are summarized in Table 4.2.

Table 4.2 Numerical uncertainties associated with the selected grid (case c).

QoI	Metric	Units	Lag-EB	RSM
ΔT_l	u_{num}	(K)	2.64	2.29
	err_{grid}	(%)	1.31	0.64
ΔT_s	u_{num}	(K)	5.18	0.35
	err_{grid}	(%)	0.35	0.23
ΔP	u_{num}	(Pa)	5.1	14.2
	err_{grid}	(%)	0.06	9.0
v_{max}	u_{num}	(m/s)	6.27	3.28
	err_{grid}	(%)	0.8	5.63

Validation and Uncertainty Quantification In the second part of the analysis, the numerical model is applied to a configuration representative of the HETREX-PT experimental campaign, with the objective of assessing its capability to reproduce both thermal and hydraulic behavior under realistic operating conditions. The

reference geometry corresponds to a ribbed cooling channel made of stainless steel, with a square cross-section and a total ribbed length of 300 mm, including 30 V-ribs with a pitch of 10 mm. The working fluid is air at approximately 0.4 MPa. A schematic representation of the experimental test section and its cross-section is reported in Fig. 4.9.

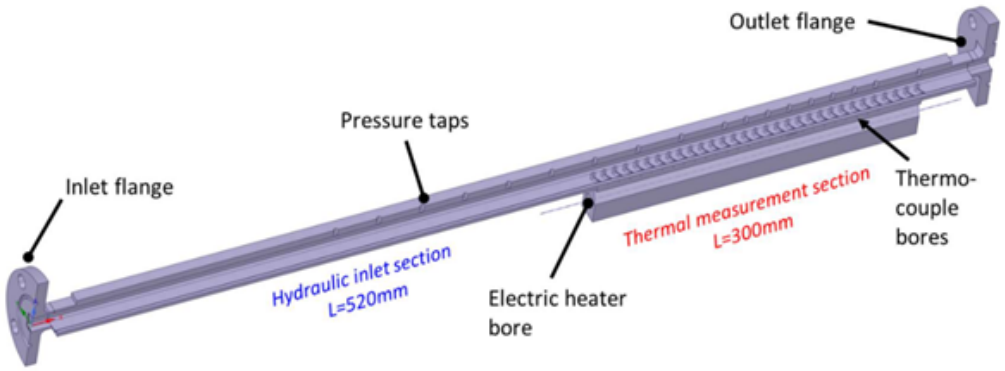


Fig. 4.9 Test section of the ribbed channel (a) and cross-section of the channel (b) adopted in the HETREX-PT experimental campaign.

The thermal boundary condition is modelled by imposing a uniform heat flux on the heated portion of the channel wall. The value of the heat flux is derived from the total input power and the effective heated surface, resulting in approximately 51.6 kW/m^2 over a heated length of 285 mm. This approximation is introduced due to the lack of detailed measurements of the spatial heat flux distribution. A steady-state conjugate heat transfer simulation is performed, consistently with the approach adopted in the verification phase. Both turbulence models previously introduced (Lag-EB and RSM) are retained in order to evaluate their impact on the predicted quantities. Due to the geometric symmetry of the configuration, only half of the domain is simulated. The boundary conditions adopted in the CFD model are summarized in Fig. 4.10.

The computational mesh in the ribbed region is consistent with the grid (c) identified during the verification step, ensuring that the numerical uncertainties previously quantified can be directly propagated to the validation analysis. Additional inlet and outlet extrusions are included to guarantee a proper boundary flow development as done in the experimental setup. A detailed view of the computational mesh is reported in fig. 4.11, where both the inlet/outlet extrusion and the ribbed regions are highlighted. The locations at which numerical results are extracted, corresponding to the positions of the experimental probes along the channel, are reported in fig. 4.12.

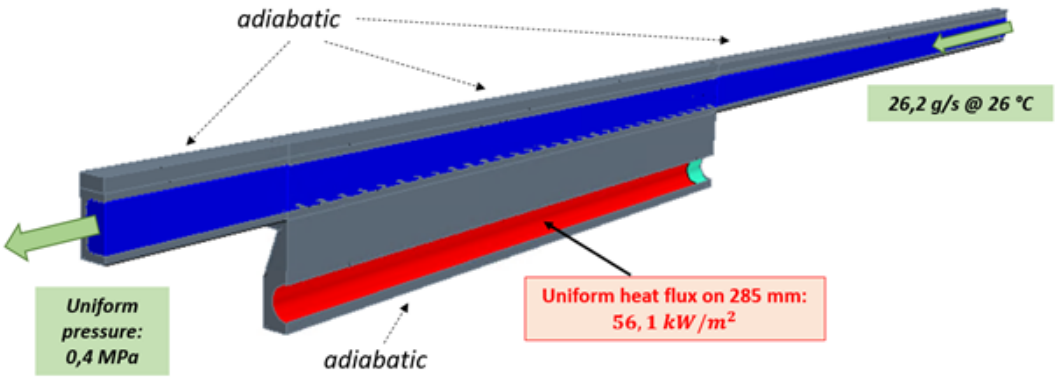


Fig. 4.10 Geometry and boundary conditions adopted for the CFD simulation of the HETREX-PT test section.

This ensures consistency between numerical and experimental data processing. The same figure also identifies reference sections used for the visualization of velocity and temperature fields, reported in Appendix A.

Validation is performed by comparing CFD predictions with experimental measurements of temperature and pressure distributions along the channel. In addition, numerical results obtained with an independent CFD model (ANSYS CFX) are considered as a secondary reference for comparison, providing further insight into modeling-related discrepancies. The comparison focuses on axial profiles of temperature and pressure, evaluated at the same locations of the experimental thermocouples and pressure taps. The results are reported in fig. 4.13 and fig. 4.14.

From a qualitative standpoint, the RSM turbulence model provides a better agreement with the experimental temperature profiles, capturing the overall trend of the temperature increase along the channel and reproducing the plateau observed in the measurements. The Lag-EB model, on the other hand, tends to systematically underpredict the temperature rise. Quantitatively, the average relative error for the Lag-EB model is of the order of $\sim 12\%$, with peaks up to $\sim 19\%$, while the RSM model shows a mean error of approximately $\sim 6\%$, with local deviations up to $\sim 20\%$ in the upstream region of the ribbed channel. Discrepancies observed near the boundaries of the heated section may be attributed to the simplified assumption of uniform heat flux, which does not fully reproduce the actual thermal boundary conditions of the experiment. This modeling assumption represents a relevant source of epistemic uncertainty that is not accounted for in the present sensitivity analysis.

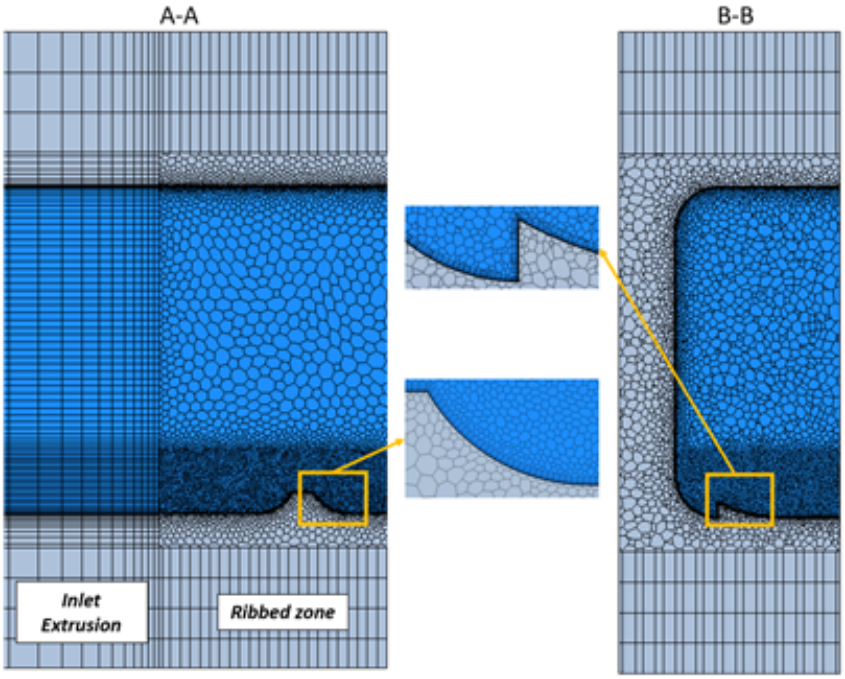


Fig. 4.11 Computational mesh for the HETREX-PT configuration: detail of the ribbed region and inlet/outlet extrusion (a), transversal and longitudinal sections highlighting mesh refinement (b).

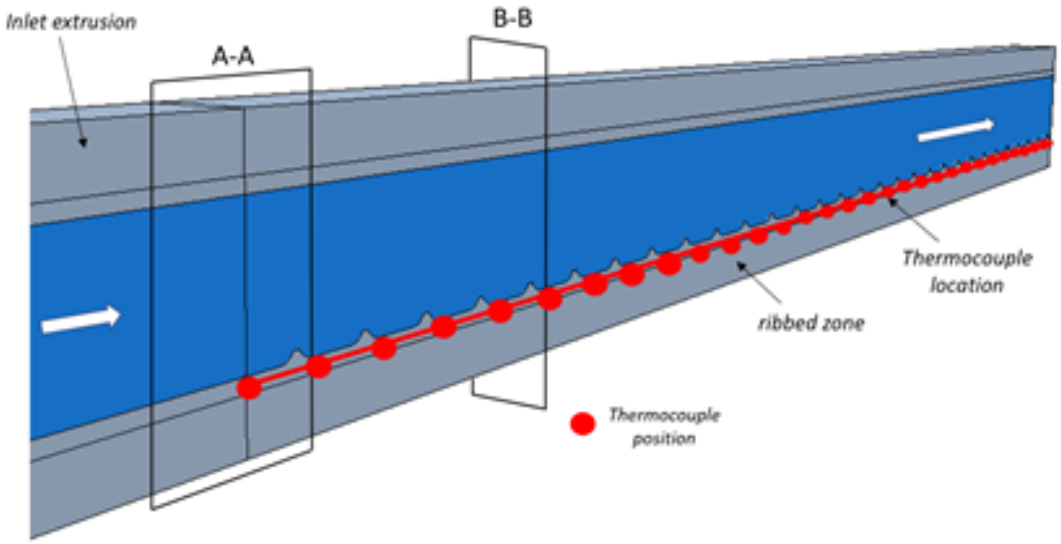


Fig. 4.12 Location of numerical probes corresponding to experimental measurement points along the channel. The figure also shows reference sections used for post-processing of velocity and temperature fields (reported in Appendix .1)

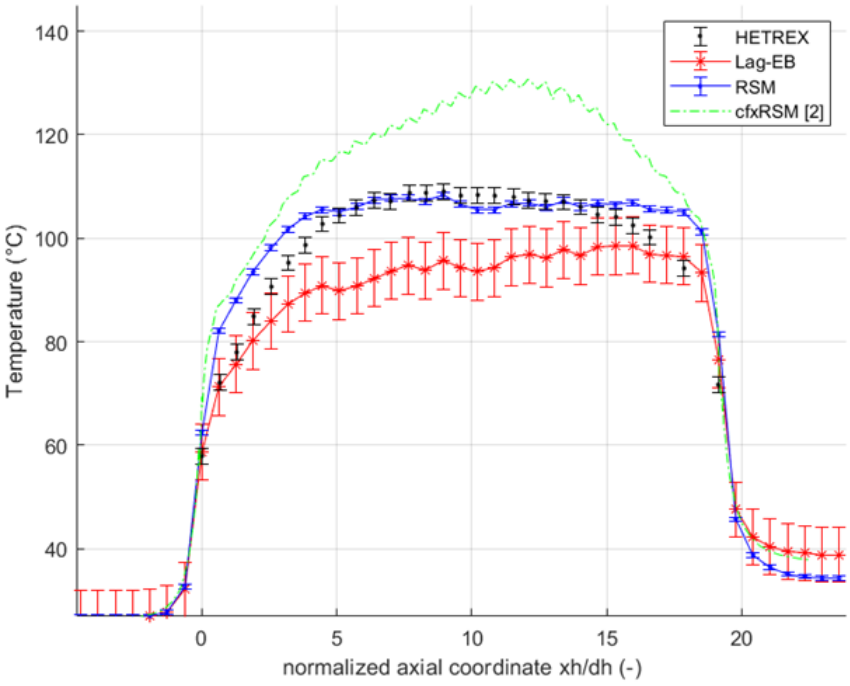


Fig. 4.13 Temperature profile along the axial coordinate at thermocouple locations: comparison between CFD predictions (Lag-EB and RSM), experimental data, and CFX results.

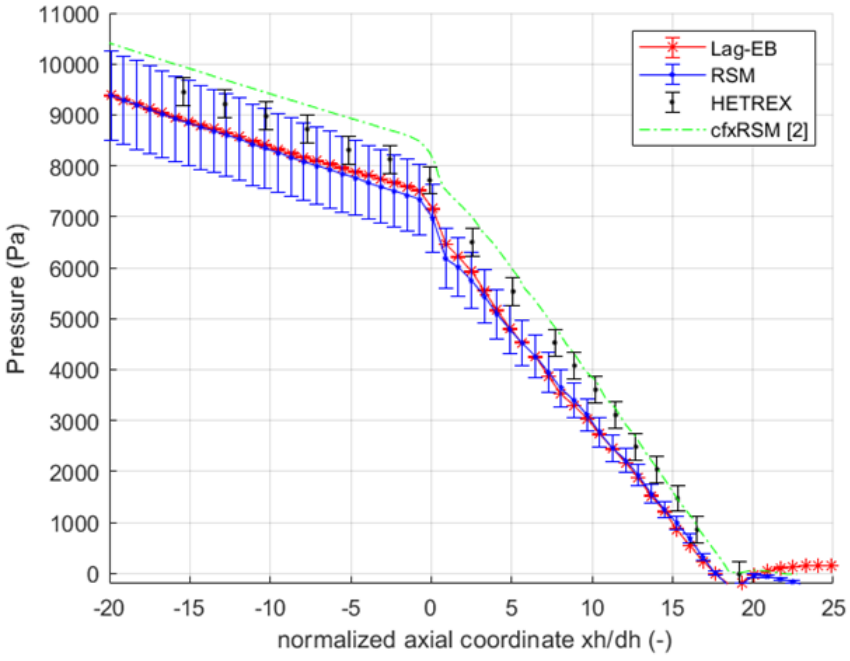


Fig. 4.14 Pressure profile along the axial coordinate: comparison between CFD predictions (Lag-EB and RSM), experimental data, and CFX results.

Regarding the pressure distribution, both turbulence models show a general tendency to underpredict the experimental values along the axial coordinate. Nevertheless, the RSM results exhibit a better agreement in terms of both trend and magnitude. When accounting for the numerical uncertainty bands derived from the grid convergence study, the experimental data lie within the uncertainty bounds of the CFD predictions, indicating consistency between model and measurements within the estimated uncertainty.

From a V&V perspective, it is important to underline that visual agreement between profiles is not sufficient to establish model validity. The assessment is instead based on the comparison error E and its associated validation uncertainty u_{val}, which provide a quantitative measure of the discrepancy between numerical predictions and experimental observations. The consistency of the model is therefore evaluated by verifying whether the observed errors remain within the estimated uncertainty bounds.

4.4 Model Credibility and Discussion

The application of the V&V methodology to the V-rib case highlights a higher level of complexity compared to the TPMS study of the previous chapter, due to the combined effects of turbulence, conjugate heat transfer, and modeling assumptions on thermal boundary conditions. As a result, the credibility of the numerical model is not governed solely by discretization errors, but also by the choice of turbulence closure and by the representation of the thermal driving mechanisms. The grid convergence study demonstrated that the numerical uncertainty strongly depends on both the selected QoI and the turbulence model. In particular, the RSM model exhibits a reduced sensitivity to grid refinement for thermal quantities, with relative uncertainties below 1% for the temperature increase, while showing a higher sensitivity for hydraulic quantities such as pressure drop. Conversely, the Lag-EB model provides more robust predictions for hydraulic QoIs, with limited grid sensitivity, but shows a higher dependence on mesh resolution for thermal quantities. This behavior reflects the intrinsic differences between the two modeling approaches: while RSM better captures turbulence anisotropy and heat transfer mechanisms, it introduces increased numerical stiffness and sensitivity to discretization.

The selection of the intermediate grid (case c) represents a compromise between computational cost and accuracy, allowing the propagation of quantified numerical uncertainties to the validation phase. The three QoIs were selected to provide complementary assessments of the numerical solution. Velocity offers an independent consistency check of the flow field, whereas pressure and temperature increase are directly related to the experimental quantities used in the subsequent validation. Their numerical uncertainties can therefore be directly propagated to the validation analysis. This aspect is crucial, as it enables a consistent comparison between CFD predictions and experimental measurements in terms of uncertainty bounds, rather than relying on qualitative agreement alone. From the validation standpoint, the comparison with HETREX-PT experimental data shows that the RSM turbulence model provides a more accurate representation of the temperature evolution along the channel, correctly capturing the overall trend and the characteristic plateau observed in the measurements. The Lag-EB model, on the other hand, systematically underestimates the temperature increase. For pressure predictions, both models tend to slightly underpredict the experimental values, although the RSM model again shows a better agreement in terms of trend and magnitude when uncertainty bands are taken into account.

Overall, the RSM turbulence model shows a satisfactory agreement with the experimental data in terms of the overall profile evolution, both for temperature and pressure. The comparison indicates that the main trends are correctly captured, with deviations that remain consistent with the estimated uncertainty levels. The Lag-EB model, while still reproducing the qualitative behaviour of the flow, exhibits larger systematic deviations, particularly in the thermal field. The assessment is therefore interpreted within the V&V framework in terms of agreement between predictions and measurements relative to the associated uncertainty, rather than through a strict pass/fail criterion. In this context, the results provide a quantitative characterization of model performance for the considered configuration and operating conditions, without implying a general validation beyond the present range of applicability.

Several sources of discrepancy can be identified. Among them, the assumption of a uniform heat flux over the heated section represents a significant simplification of the experimental conditions, where the actual heat flux distribution is not directly measured. The use of a half-domain based on geometric symmetry is an additional modeling assumption adopted to reduce computational cost. While consistent with the nominal configuration, its influence on possible asymmetric flow features was not

independently assessed through a full-domain simulation and therefore represents an additional limitation of the present verification and validation assessment. This introduces a modeling uncertainty that directly affects the temperature field and, consequently, the coupled thermo-fluid dynamics. In addition, the sensitivity of the results to the turbulence model highlights the importance of model-form uncertainty, which becomes dominant in complex flow configurations involving separation, recirculation, and strong anisotropy. Despite these limitations, the analysis demonstrates that the CFD model, when properly verified and validated, is able to reproduce the main physical trends of the system and to provide predictions that are consistent with the experimental data within the estimated uncertainty bounds. This supports its use as a complementary tool for the interpretation of experimental results and for the assessment of design-relevant quantities.

Additional geometric details, together with velocity and temperature fields obtained with both turbulence models, are reported in Appendix A, which complements the discussion by providing a more complete view of the flow structure and thermal development within the computational domain.

Chapter 5

CFD Assessment of Tritium Release in a ITER Process Systems

This chapter presents the application of the verification and validation (V&V) methodology to a transient multi-species CFD simulation of a radioactive release scenario in an ITER process room. Differently from the previous case studies, no experimental data are available for the configuration under investigation. As a consequence, a formal model validation cannot be performed and the analysis is limited to solution verification and numerical uncertainty quantification. This limitation is not merely procedural, but has direct implications on model credibility. In the absence of validation data, it is not possible to assess the predictive capability of the model with respect to reality. The analysis can only determine whether the numerical solution is consistent with the underlying discretization schemes and sufficiently independent from numerical parameters such as mesh resolution and time step. Therefore, the present study focuses on evaluating the numerical robustness of the model and on identifying potential sources of numerical uncertainty that may affect the reliability of the results.

The case study is based on a predefined CFD model provided in the framework of an industrial activity, where both the computational domain and the physical setup are fixed. The objective is to estimate the time evolution of the tritium concentration within the room and, in particular, to evaluate detection times at selected monitoring locations. From a V&V perspective, this represents a typical scenario in which the analyst has limited control over modeling assumptions and must rely on a

posteriori verification to assess the quality of the numerical predictions. The problem is inherently transient and characterized by strong coupling between convection, turbulent mixing, and species transport. These features make the numerical solution particularly sensitive to discretization choices in both space and time. As will be shown in the following sections, this leads to relatively large numerical uncertainties, which can be interpreted as an intrinsic difficulty of the problem rather than a deficiency of a specific numerical tool.

5.1 Problem Definition and Intended Use

The case study under investigation concerns the numerical simulation of a radioactive release scenario in the ITER Process Room #2, with the objective of estimating the spatial and temporal evolution of tritium concentration within the enclosure. The quantity of interest is the radioactive specific activity, expressed in GBq/m^3, evaluated at a set of predefined monitoring locations corresponding to the positions of a detection system. The model is employed to estimate detection times associated with the hazardous release under the prescribed operating conditions. Due to the absence of experimental data for this configuration, the analysis cannot include a validation step. Consequently, the assessment of the model is restricted to the verification of the numerical solution, with the aim of quantifying its numerical uncertainty and evaluating the robustness of the predicted quantities.

The computational domain consists of the fluid volume of the ITER process room, including the main internal obstacles such as the glove boxes, while smaller geometric details are neglected. The ventilation system (HVAC) plays a central role in the problem, as it governs the transport and dilution of the released species. Fresh air is supplied through five circular inlets located on one lateral wall, while six exhaust ducts are positioned on the opposite wall. A constant leakage of a nitrogen–tritium mixture is imposed on the lateral surface of one of the glove boxes. A schematic representation of the computational domain, including the tritium release location and monitoring points, is reported in Fig. 5.1. The figure also shows the decomposition of the domain for parallel computation.

The scenario corresponds to a constant release of tritium under operating HVAC conditions. Compared to the original setup described in [28], a modified initialization strategy is adopted: a steady-state simulation without tritium injection is

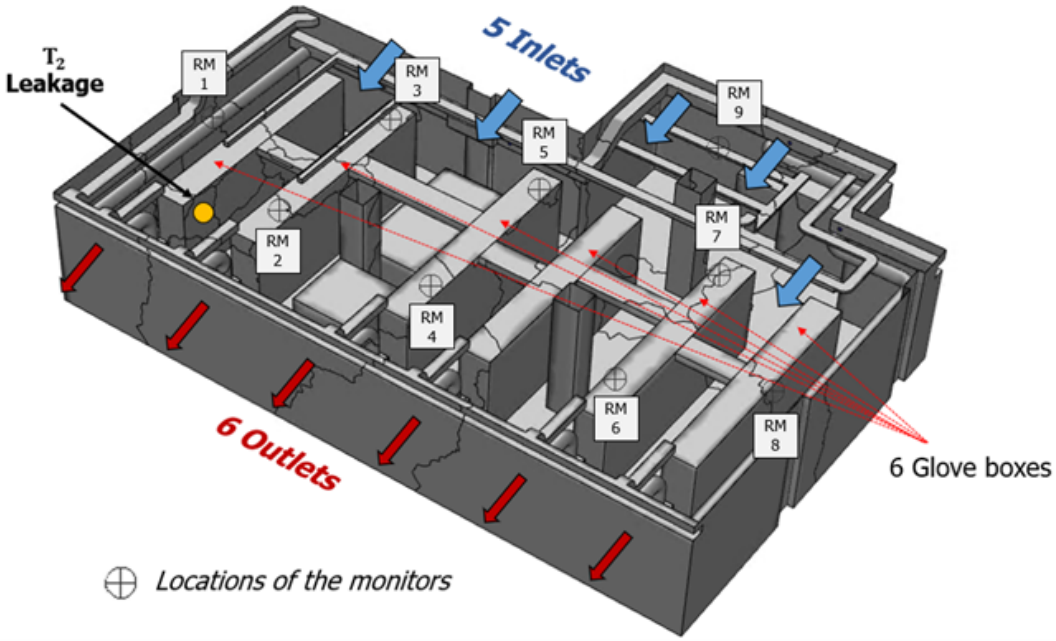


Fig. 5.1 Computational domain of the ITER Process Room #2, including tritium release location and monitoring points used for the evaluation of the QoI.

first performed to establish a converged velocity field, which is then used as initial condition for the transient simulations with active leakage. This approach ensures a clearer separation between flow development and species transport. The flow regime is highly turbulent, with a Reynolds number of the order of 10^5, and inherently unsteady due to the complex interaction between ventilation, obstacles, and buoyancy effects. This intrinsic unsteadiness plays a critical role in the definition of the QoI, which is evaluated as a time-averaged quantity in order to obtain statistically meaningful results.

Finally, it is important to stress that the absence of experimental data prevents any form of validation. As a consequence, the results obtained in this study cannot be interpreted as quantitatively predictive, but rather as numerically consistent estimates within the limits of the adopted modeling assumptions. The following sections will therefore focus on solution verification and on the assessment of numerical robustness, which represent the only means to build confidence in the simulation results for this case.

5.2 Numerical Model Description

The numerical model adopted in this study aims at reproducing the transport and dispersion of a nitrogen–tritium mixture within the ITER Process Room #2 under forced ventilation conditions. The problem is modeled as a turbulent, buoyancy-affected flow with species transport. The governing equations consist of the steady and unsteady Reynolds-Averaged Navier–Stokes (RANS) equations for mass and momentum conservation, coupled with the energy equation and with a scalar transport equation for the tritium concentration. The fluid is treated as an ideal gas, allowing density variations due to temperature and species concentration to be taken into account. Turbulence effects are modeled using two different closures, namely the k–ε RNG model and the k–ω SST model. The adoption of two turbulence models is intended to assess the sensitivity of the solution to turbulence closure assumptions, which represent a known source of modeling uncertainty in indoor airflow simulations. Species transport is modeled through a convection–diffusion equation, where the tritium concentration is treated as a passive scalar. Molecular diffusion is accounted for, while no chemical reactions are considered, consistently with the physical scenario of a non-reactive release. Boundary conditions are prescribed consistently with the reference study. The inlet flow is imposed as a velocity boundary condition with a magnitude of 13.6 m/s at a temperature of 17.3°C, corresponding to a total volumetric flow rate of approximately 3822 m^3/h (two air changes per hour). The incoming fluid is assumed to be pure air. Outlet ducts are treated as pressure outlets at atmospheric pressure. The tritium leakage is modeled as a velocity inlet with a magnitude of 1.0 m/s at 22°C, with a molar fraction of tritium equal to 2.424%, corresponding to a release rate of one mole per hour. Thermal boundary conditions are simplified by imposing a constant temperature of 22°C on all walls, floor, and ceiling. The glove boxes represent the only heat source in the domain, with a total thermal power of 1 kW per unit, implemented as a uniform heat flux on their external surfaces. A summary of the boundary conditions is reported in Fig. 5.2.

The numerical solution is obtained using a segregated approach, where the governing equations are solved sequentially. Pressure–velocity coupling is handled through the SIMPLE algorithm, while second-order discretization schemes are employed for all spatial terms to ensure improved accuracy. Transient simulations are carried out over a physical time of 600 s using a time step of 1 s, with 20 inner iterations per time step. Due to the strongly unsteady nature of the problem, the QoI

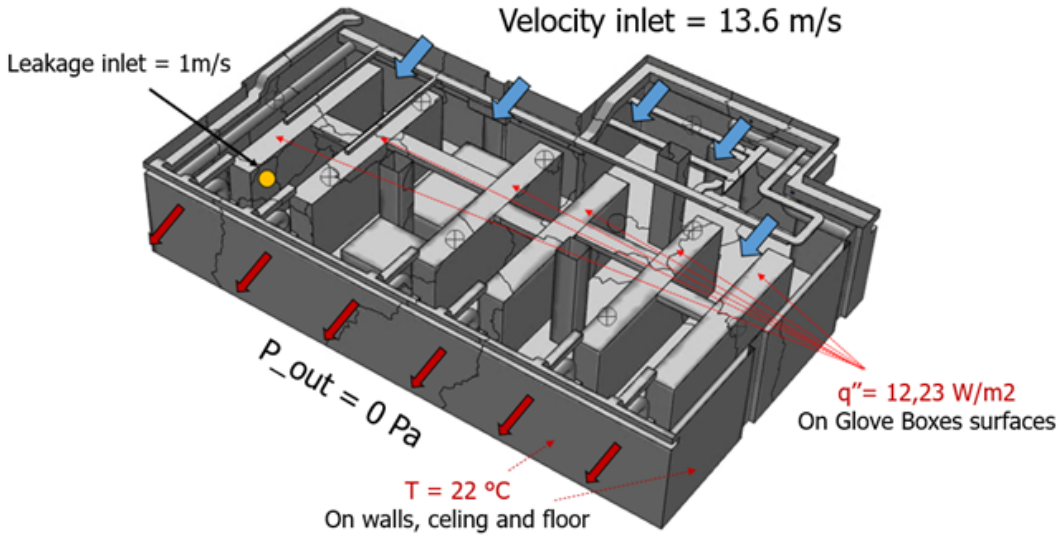


Fig. 5.2 Boundary conditions adopted for the CFD simulation of the ITER Process Room #2.

is evaluated as a time-averaged quantity over a sufficiently large number of iterations, introducing an additional source of uncertainty related to temporal resolution and statistical convergence. All simulations are performed in double precision to minimize round-off errors, which are therefore considered negligible compared to discretization and iterative uncertainties. The numerical setup described here is used consistently throughout the verification analysis presented in the following sections.

5.3 Solution Verification

The verification of the numerical solution for the present case study presents additional challenges compared to the previous applications, due to the intrinsically unsteady nature of the flow. The transport of tritium within the domain is governed by diffusion in the vicinity of the leakage and predominantly by advection induced by the HVAC system. The resulting flow field is highly turbulent ($\mathrm{Re} > 2 \times 10^5$) and inherently unsteady, leading to persistent fluctuations of the quantity of interest (QoI), the specific activity, at all monitoring locations. As a consequence, a formal steady-state solution is not reached, and the QoI exhibits oscillations around a mean value. In order to perform a consistent uncertainty quantification, a hybrid approach is adopted. A steady-state simulation with constant tritium release is first carried out to characterize the statistical behavior of the solution and to quantify numer-

ical uncertainties. This steady solution is then used as a reference to support the interpretation of the transient results.

Statistical characterization of the solution Given the absence of convergence to a steady value, the QoI is treated as a stochastic variable. The mean value μ and standard deviation σ are computed over the last $N = 1000$ iterations of the steady-state simulation:

$$\sigma = \sqrt{\frac{1}{N}\sum_{i=1}^{N}(\phi_i - \mu)^2} \tag{5.1}$$

where ϕ_i represents the instantaneous value of the specific activity at iteration i. Under this assumption, the QoI can be expressed within the interval

$$\phi \in [\phi_{\text{mean}} - \sigma \; ; \; \phi_{\text{mean}} + \sigma] \tag{5.2}$$

which provides an estimate of the temporal variability of the solution. The standard deviation and its normalized value with respect to the mean are reported for all monitoring points in Fig. 5.3. The results indicate that temporal fluctuations are significant, with normalized values in the range of approximately 8-15% for the k–ε RNG model and 10–15% for the k-ω SST model, with limited differences between the two turbulence closures.

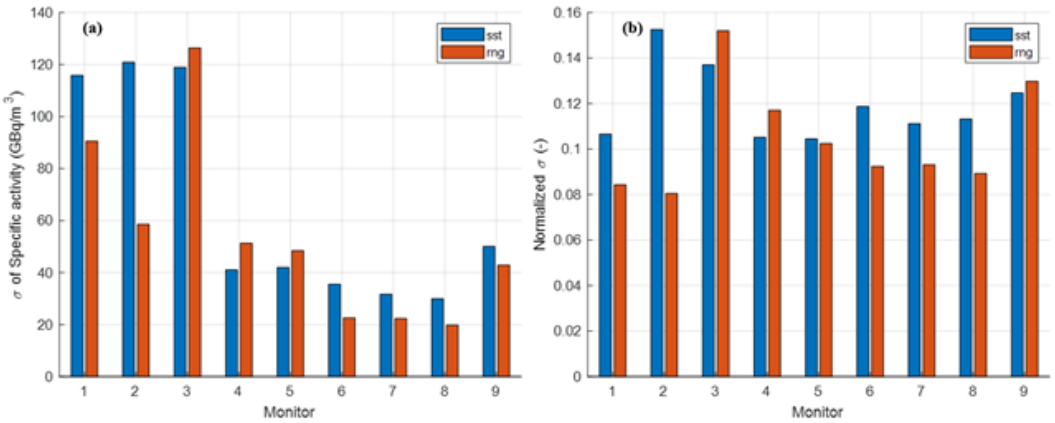


Fig. 5.3 Standard deviation of the specific activity at the monitoring locations, reported in absolute value (a) and normalized with respect to the mean value (b), for the two turbulence models, SST in blue and RNG in red.

Spatial discretization error The spatial discretization error is assessed through a grid refinement study performed on three unstructured meshes of increasing resolution. The computational grids are composed of tetrahedral cells, which are well suited for complex three-dimensional geometries. Local refinement is applied in regions of expected high gradients, namely in the proximity of the internal obstacles and around the tritium release location. In particular, a spherical refinement region of radius 6 m is introduced around the leakage source to adequately resolve the concentration gradients. The refinement strategy is based on a quasi-uniform refinement ratio between consecutive grids. According to the ASME V&V standards, for three-dimensional problems the refinement ratio should be at least equal to 1.25. In the present case, an average value of $r \approx 1.26$ is achieved. It is worth noting that, due to the use of unstructured meshes and localized refinements, the refinement ratio cannot be strictly uniform in all spatial directions. This limitation is typical of complex 3D configurations and represents a potential source of uncertainty in the evaluation of the discretization uncertainty.

The three computational grids are generated by progressively reducing the base cell size and the local refinement levels. The main mesh parameters are summarized in Table 5.1.

Table 5.1 Mesh parameters adopted for the grid refinement study.

	Grid 3	**Grid 2**	**Grid 1**
Cell base size (mm)	100	90	65
Refinement (obstacles) (mm)	80	50	35
Refinement (source) (mm)	80	50	35
Number of cells ($\times 10^6$)	4	8	17

The discretization error is quantified by applying the 5-steps procedure to the steady-state solution with active tritium release. The specific activity at the monitoring locations is evaluated for each grid and analyzed as a function of the representative grid size, normalized with respect to the finest grid. The results are reported in Fig. 5.4, separately for the two turbulence models considered. A consistent trend with grid refinement is observed for most monitoring points, although local deviations are present due to the combined effects of turbulence modeling and unstructured grid refinement.

A comparison between the two turbulence models on the finest grid highlights that the k–ε RNG model generally underpredicts the specific activity with respect

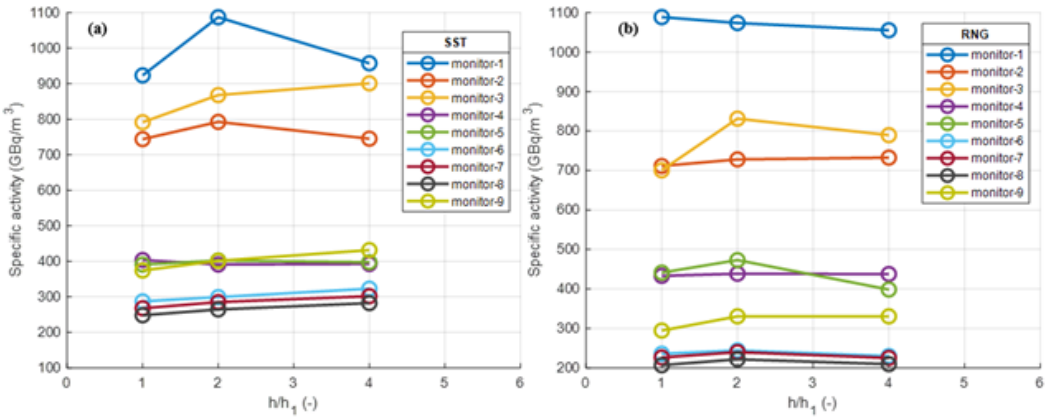


Fig. 5.4 Specific activity at monitoring locations as a function of normalized grid size for (a) k–ω SST and (b) k–ε RNG turbulence models.

to the k–ω SST model, except in proximity of the leakage region and in selected monitoring locations. This difference reflects the sensitivity of the solution to turbulence modeling, which represents an additional source of modeling uncertainty not explicitly quantified in the present analysis.

Numerical uncertainty estimation In the present framework, the numerical uncertainty u_{num} is defined by combining spatial discretization errors and the temporal variability of the solution, represented by the standard deviation σ. This approach reflects the fact that, in unsteady turbulent flows, temporal fluctuations constitute an intrinsic component of the numerical uncertainty. The steady-state solution is therefore used to quantify a conservative estimate of the numerical uncertainty, which is subsequently propagated to the transient simulations.

Applicability to transient simulations The use of steady-state statistics to estimate uncertainty in the transient simulations is justified by the following considerations:

- Tritium transport is dominated by advection, as indicated by the high Péclet number

$$\text{Pe} = \frac{Lv}{D} \approx 10^3 \div 10^6 \tag{5.3}$$

  where L is a characteristic length scale, v is the flow velocity, and D is the diffusion coefficient. This implies that fluctuations in the QoI are primarily driven by velocity fluctuations.

- The transient simulations are initialized from the time-averaged steady-state velocity field (without tritium), obtained by averaging the velocity field over a sufficiently long time interval. The initial condition therefore represents the mean flow field, while the statistical variability observed during the steady-state calculation is characterized as:

$$v_{\text{mean}} \pm \sigma_v \tag{5.4}$$

  For an approximately normal distribution, this interval corresponds to a coverage of approximately 68%; it is therefore used here as a measure of the characteristic variability of the flow rather than as a formal confidence interval.

- The tritium leakage represents a small perturbation with respect to the total HVAC mass flow rate. Therefore, it does not significantly alter the underlying flow field, and the velocity fluctuations observed in steady-state conditions remain representative during the transient.

- Iterative errors are not expected to introduce additional uncertainty in the transient simulations. On the contrary, they tend to decrease with smaller time steps, as convergence is enforced at each time level. For the adopted time step ($\Delta t = 1$ s) and number of inner iterations, the iterative error is considered negligible compared to discretization and temporal uncertainties.

Summary of numerical uncertainties The different contributions to the numerical uncertainty are combined to obtain an overall estimate of u_{num} for the quantity of interest. The spatial discretization uncertainty, evaluated on the finest grid, is in the range of 8-35% for the k-ω SST model and 1-22% for the k-ε RNG model. The time discretization uncertainty, quantified as the normalized standard deviation of the QoI around its mean value, is found to be in the range of 11-15% for the SST model and 8-15% for the RNG model. The overall numerical uncertainty is obtained by combining these contributions, resulting in relatively large uncertainty levels, particularly for the SST model. The results are summarized in Table 5.2.

In a conservative perspective, the upper bounds of the numerical uncertainty may be considered, leading to values up to approximately 50% for the SST model and 37% for the RNG model. These results highlight the strong impact of both

Table 5.2 Summary of numerical uncertainties for the finest grid and the two turbulence models. The total uncertainty u_{num} is obtained by conservatively summing the spatial discretization and observed temporal variability contributions.

	SST		RNG	
Quantity	**min**	**max**	**min**	**max**
$u_{\text{discr, space}}$ (%)	8	35	1	22
u_{time} (%)	11	15	8	15
u_{num} (%)	19	50	9	37

spatial resolution and intrinsic flow unsteadiness on the reliability of the numerical predictions.

Transient results with uncertainty propagation The temporal evolution of the specific activity is reported together with its corresponding uncertainty bounds for both turbulence models, as shown in Fig. 5.5.

From the time histories of the specific activities at different monitor location, the detection times corresponding to relevant thresholds (e.g. 1 DAC and detection limit) are evaluated. The results are summarized in Fig. 5.6, where the variability associated with the different turbulence models and the propagated uncertainties can be observed,.

It is worth noting that, for some monitoring locations, the detection threshold is not reached within the simulated time window, particularly for the RNG turbulence model. This aspect further highlights the sensitivity of the predicted quantities to modeling assumptions and numerical uncertainties. Overall, the results show that the predicted detection times are affected by significant uncertainty levels, which must be taken into account when interpreting the outcomes of the simulation. In the absence of experimental validation data, these uncertainty bounds represent the only quantitative measure of the reliability of the numerical predictions.

5.4 Model Assessment and Numerical Robustness

The primary monitored quantity is the specific activity measured at the monitoring probes as a function of time. The detection time is subsequently derived from this time-dependent signal according to the adopted detection criterion. Therefore,

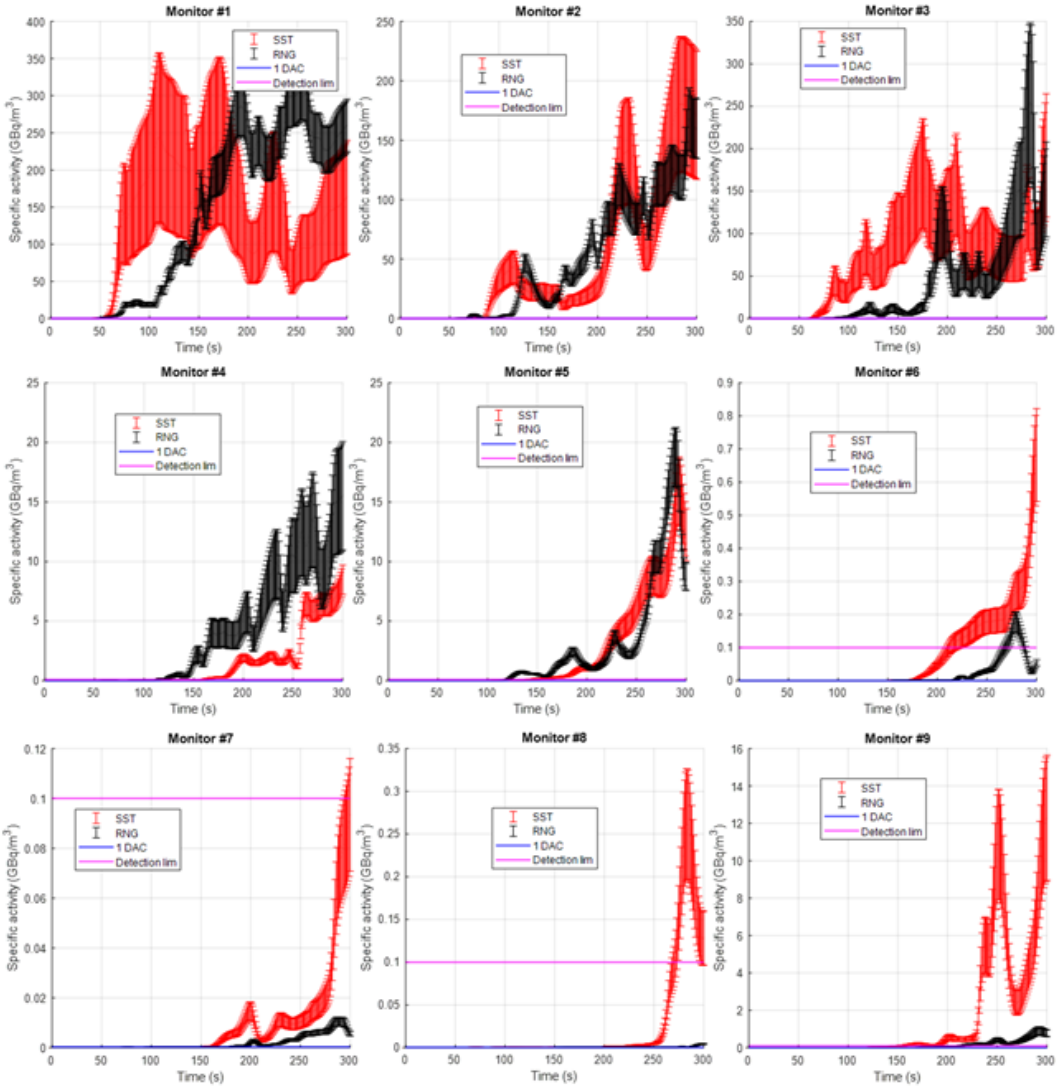


Fig. 5.5 Time evolution of the specific activity at the monitoring locations for the SST (red) and RNG (black) turbulence models. Uncertainty bands derived from the numerical uncertainty analysis are also reported.

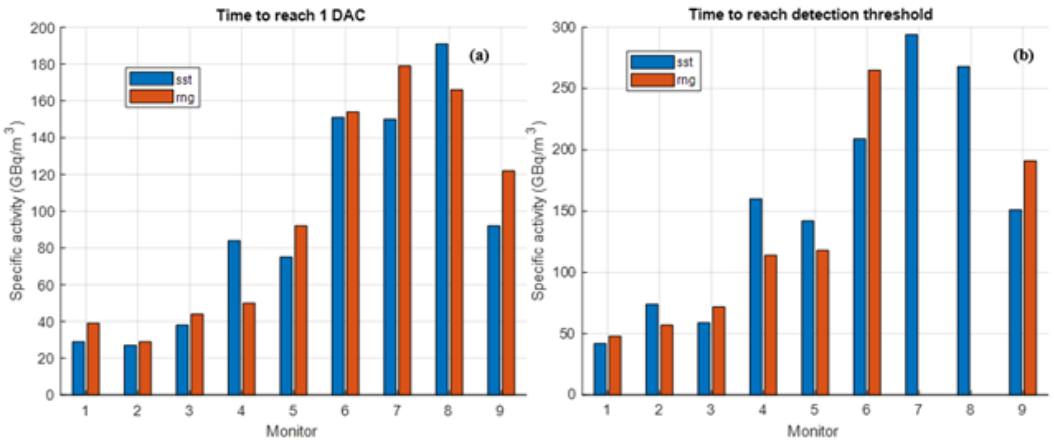


Fig. 5.6 Computed detection times corresponding to (a) 1 DAC and (b) detection threshold for the different monitoring locations.

specific activity represents the primary Quantity of Interest, while detection time is considered a derived metric used to characterize the transport and arrival of tritium at the monitoring locations. The assessment of the present numerical model is inherently limited by the absence of experimental data for the investigated configuration. As a consequence, a formal validation of the model cannot be performed and the predictive capability cannot be quantitatively established. The analysis is therefore restricted to the verification of the numerical solution and to the evaluation of its robustness.The verification results highlight that the problem is strongly affected by flow variability and by significant sensitivity to spatial resolution. The numerical uncertainty, quantified through the combination of spatial discretization and temporal variability, reaches values up to 50% for the SST model and 37% for the RNG model. A sensitivity assessment to the temporal discretization was also performed and did not result in appreciable changes in the monitored quantities; therefore, temporal discretization was not identified as a dominant source of uncertainty in the present analysis. These levels of uncertainty are considerably higher than those observed in the previous case studies and are primarily associated with the complex, turbulence-driven transport mechanisms governing the problem. From a numerical standpoint, the solution can be considered consistent, as the adopted discretization schemes and refinement strategies lead to coherent trends across the different grids. However, the relatively large GCI values and the persistent oscillations of the QoI indicate that the solution is only weakly grid-independent and strongly influenced by flow fluctuations. This limits the robustness of local predictions, particularly in

terms of detection times at specific monitoring locations. The comparison between turbulence models further confirms that modeling choices have a non-negligible impact on the results, introducing an additional source of variability that cannot be resolved within the present V&V framework. In this context, the agreement between different models cannot be interpreted as validation, but only as an indication of qualitative consistency. Overall, the study demonstrates that, in the absence of validation data, verification alone is not sufficient to establish quantitative predictive credibility. Nevertheless, the systematic application of the V&V methodology allows for a transparent quantification of numerical uncertainties and highlights the limitations of the simulation results. The model can therefore be used to provide indicative trends and order-of-magnitude estimates within the investigated configuration, but its predictions should not be interpreted as quantitatively validated, particularly when used for safety-related assessments such as detection time estimation.

Chapter 6

Multiphysics and Multiphase model of a lab scale PEM Fuel Cell

This chapter presents the application of the V&V methodology to a multiphysics and multiphase CFD problem, characterized by the strong coupling between fluid dynamics, electrochemistry, heat transfer, and species transport. Compared to the previous case studies, the level of complexity is further increased due to the presence of electrochemical reactions and phase change phenomena, which introduce additional sources of modeling uncertainty. The case study focuses on a lab-scale Proton Exchange Membrane Fuel Cell (PEMFC), a key technology for clean energy conversion, where hydrogen and oxygen are converted into electricity, heat, and water through electrochemical reactions. The layered structure of the cell, including membrane, catalyst layers, and porous transport media, is schematically reported in fig. 6.1. From a modeling perspective, the problem involves multiple interacting physical processes occurring at different spatial scales. In addition to fluid flow and heat transfer, the model must account for electrochemical reactions, charge transport, and water management within porous media. As a consequence, the V&V process must address not only discretization uncertainties, but also model uncertainties associated with electrochemical kinetics, transport properties, and multiphase behavior. In this context, particular attention is devoted to a code-to-code comparison between different CFD implementations of the same physical problem, enabling a structured assessment of predictive capability across three commercial and open-source platforms: STAR-CCM+ [27], ANSYS Fluent [29] and OpenFOAM [30].

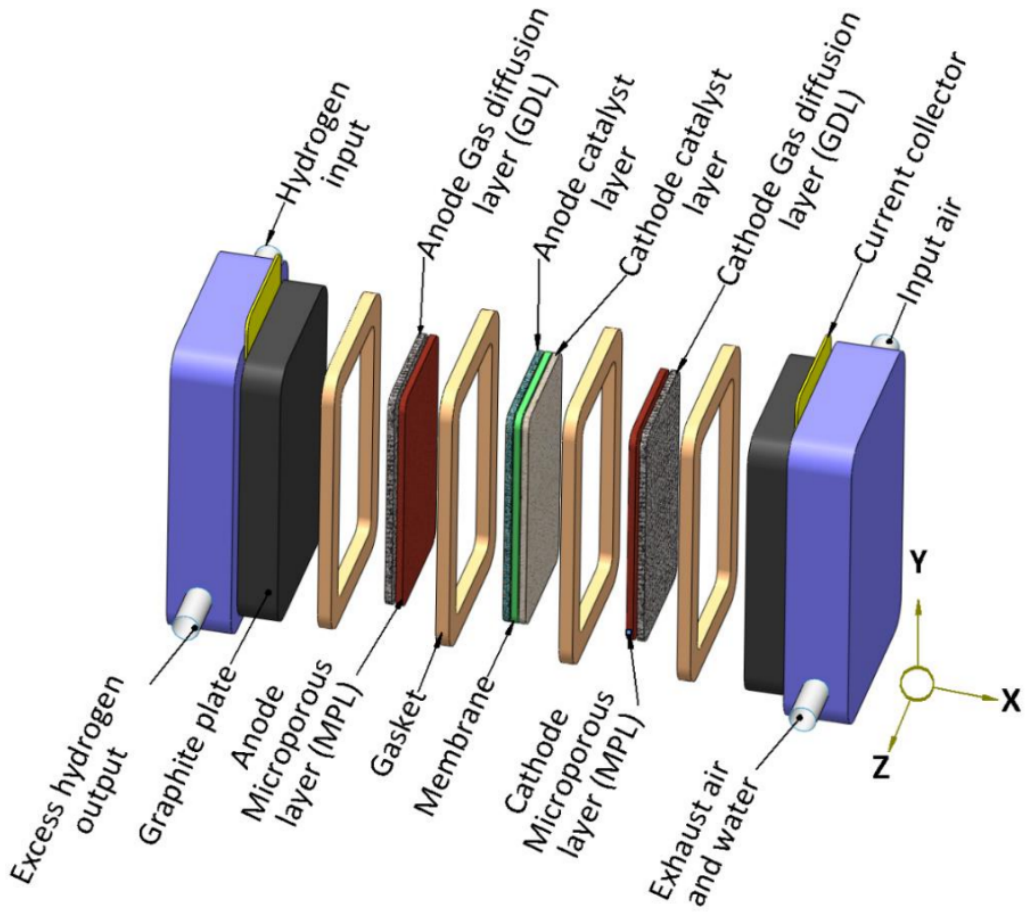


Fig. 6.1 Schematic representation of the PEM fuel cell structure, including membrane electrode assembly and flow field channels [1].

6.1 Problem Definition and Intended Use

The analysis is structured as a code-to-code comparison and Verification and Validation (V&V) study of a lab-scale PEM fuel cell, where three CFD implementations (STAR-CCM+, ANSYS Fluent and OpenFOAM) are evaluated under identical geometrical and operating conditions. The primary objective is to assess the consistency of the numerical predictions across different solver frameworks and to quantify their agreement with available experimental results. The analysis is carried out on a single PEMFC configuration operating under nominal conditions representative of low to moderate current density regimes, where multiphase transport effects remain limited but still non-negligible. Within this framework, two Quantities of Interest (QoIs) are identified: the mean current density, expressed in A/cm^2, and the mean liquid water saturation within the porous media. The first quantity represents a direct indicator of the electrochemical performance of the cell and can be validated against experimental measurements. The second one provides insight into water management within the cell, which strongly affects performance but is not directly accessible from the available experimental dataset. As a consequence, the V&V process is applied differently to the two QoIs. A full verification and validation procedure is carried out for the current density, enabling a quantitative comparison with experiments. In contrast, the analysis of liquid water saturation is limited to solution verification and code-to-code comparison, with no direct validation step. Compared to the previous test cases, the PEMFC represents a significantly more complex multiphysics problem, where fluid flow, heat transfer, species transport, phase change, and electrochemical reactions are strongly coupled across multiple spatial scales and heterogeneous domains. In particular, the presence of porous media, the coexistence of liquid and vapor phases, and the coupling between charge transport and reaction kinetics introduce additional sources of modeling uncertainty and increase the sensitivity of the solution to both numerical and model-form choices. Within this context, even small differences in the implementation of sub-models or numerical schemes may lead to non-negligible discrepancies in the predicted quantities of interest. This increased level of complexity makes the application of a rigorous V&V framework particularly critical. The code-to-code comparison is not only used to assess consistency across different CFD platforms, but also to identify the impact of solver-specific formulations on the prediction of coupled transport and electrochemical phenomena. At the same time, the availability of experimental data

of the PEMFC performance enables a quantitative validation of the electrochemical response, providing a reference to assess model credibility for at least one of the selected QoIs.

The electrochemical model adopted in this work corresponds to the native implementations available in the three software environments. The kinetic parameters are consistently aligned across all simulations, and the models are developed under the same set of physical assumptions, ensuring that differences in the results can be attributed to solver-specific formulations and numerical implementations rather than to input inconsistencies. In this sense, the present study isolates the effect of the numerical framework on the predictive capability of the models, rather than comparing different physical descriptions. The intended use of the numerical models is therefore to evaluate their predictive consistency in a strongly coupled multiphysics environment and to quantify the level of confidence associated with the computed QoIs. In particular, the V&V procedure provides a structured approach to assess numerical uncertainty, distinguish between verification and validation domains, and support a critical interpretation of the results in light of the limitations imposed by both the modeling assumptions and the available experimental data.

6.2 Numerical Model Description

The numerical models implemented in STAR-CCM+, ANSYS Fluent, and OpenFOAM are built to reproduce the same PEMFC configuration under identical geometrical and operating conditions, ensuring a consistent basis for the subsequent Verification and Validation (V&V) analysis. All solvers rely on a finite-volume discretization of the governing conservation equations for mass, momentum, energy, species transport, and electric charge. The corresponding formulations are reported in tables 6.1 and 6.2, with a unified set of modeling assumptions:

- Laminar flow regime.
- Steady-state operation.
- Ideal gas behavior for gaseous species.
- Homogeneous and isotropic porous media (GDL, MPL, CL).

- Nafion membrane permeable only to water.
- Local thermodynamic equilibrium between liquid and vapor phases.

Within this framework, all transport and electrochemical phenomena are coupled through volumetric or interfacial source terms. These terms represent the core of the multiphysics coupling and include electrochemical reaction rates, phase change effects, porous resistance contributions, and species generation/consumption. A unified summary of all source terms appearing in the governing equations is reported in table 6.3, where the contributions are organized by equation and by cell region (channels, porous media, and catalyst layers).

From a modeling perspective, the main structural difference between the solvers lies in the treatment of multiphase flow and in the representation of the ionomer phase within the catalyst layers. In OpenFOAM, the PEMFC model is implemented using the *openFuelCell* library, which adopts an Euler-Euler formulation where gas and liquid phases are treated as interpenetrating continua, each governed by its own conservation equations. In contrast, STAR-CCM+ and ANSYS Fluent employ a Mixture Multi-Phase (MMP) formulation, where a single set of transport equations is solved for the mixture and phase interaction effects are included through additional closure relations and source terms. Concerning the ionomer phase and the spatial representation of electrochemical reactions, in STAR-CCM+, the catalyst layer is modeled through a lumped interfacial (2D) formulation at the CL/MEM boundary, without explicitly resolving the ionomer phase within the catalyst layer volume. Conversely, in Fluent and OpenFOAM the ionomer is explicitly resolved as a distributed phase within the three-dimensional catalyst layer, allowing volumetric description of proton transport and electrochemical reactions.

Species transport is described through advection-diffusion equations as reported in tables 6.1 and 6.2. In porous media, diffusion dominates and is modeled using effective diffusion coefficients that account for microstructural effects. In all solvers, species source terms include electrochemical consumption/production as well as phase exchange mechanisms, consistently coupled with the multiphase formulation. Water transport in the ionomer phase represents a key aspect of the PEMFC physics. It is governed by the competition between electro-osmotic drag and back diffusion, combined with sorption and desorption processes between gas-phase and dissolved water. Although the governing formulation is consistent across all solvers, differences arise in its spatial representation within the catalyst layer, as discussed in section .2.

The electrochemical behavior is modeled using Butler-Volmer kinetics, where the local current density is expressed as a function of activation overpotential and reactant concentrations. While the same kinetic formulation is used in all three codes, the spatial discretization differs: Fluent and OpenFOAM adopt a volumetric implementation within the catalyst layers, whereas STAR-CCM+ applies an interfacial formulation at the CL/MEM boundary. This leads to different numerical representations of the same physical mechanism, which is one of the key aspects investigated in the present V&V study.

Overall, the numerical framework ensures that all models are built upon a common physical basis, while explicitly preserving solver-specific implementations. This separation allows a consistent code-to-code comparison, in which observed discrepancies can be attributed to differences in numerical treatment rather than to inconsistencies in the physical model definition.

Table 6.1 Set of governing equations used to describe multiphase transport and electrochemical charge conservation in the PEMFC model, common to STAR-CCM+ and ANSYS Fluent. Equations are expressed in a generalized steady-state multiphase formulation. [2, 3].

	Equation
Mass	$\nabla(\rho_{\text{mix}}\vec{u}_{\text{mix}}) = S_m$
Momentum	$\nabla(\chi\rho_{\text{mix}}\vec{u}_{\text{mix}}\vec{u}_{\text{mix}}) = -\nabla p + \nabla(\chi\tau) + \chi S_P + S_U$
Species	$\nabla(\rho_{\text{mix}}Y_i\vec{u}_{\text{mix}}) = \nabla(\rho D_i^{\text{eff}}\nabla Y_i) + S_i$
Charge	$\nabla(\sigma_{\text{mem}}^{\text{eff}}\nabla\Phi_{\text{mem}}) + S_{\Phi_{\text{mem}}} = 0$ $\nabla(\sigma_{\text{sol}}^{\text{eff}}\nabla\Phi_{\text{sol}}) + S_{\Phi_{\text{sol}}} = 0$
Energy	$\nabla\left[(\rho_{\text{mix}}c_p)^{\text{eff}}\vec{u}_{\text{mix}}T\right] = \nabla(k^{\text{eff}}\nabla T) + S_T$

Table 6.2 Set of governing equations used to describe multiphase transport and electrochemical charge conservation in the OpenFOAM PEMFC model. [4].

	Equation
Mass	$\nabla\cdot(\alpha_\phi\rho_\phi\mathbf{U}_\phi) = S_\phi$
Momentum	$\nabla\cdot(\alpha_\phi\rho_\phi\mathbf{U}_\phi\mathbf{U}_\phi) + \nabla\cdot(\alpha_\phi\mu_\phi\nabla\mathbf{U}_\phi) = -\alpha_\phi\nabla p + \alpha_\phi\rho_\phi\mathbf{g} + \mathbf{M}_\phi$
Species	$\nabla(\alpha_\phi\rho_\phi\mathbf{U}_\phi Y_i) = \nabla\cdot(\alpha_\phi\rho_\phi D_i^{eff}\nabla Y_i) + \alpha_\phi S_i$
Charge	$\nabla\cdot(\sigma_E\nabla\varphi_E) = J_E$ $\nabla\cdot(\sigma_I\nabla\varphi_I) = J_I$

Table 6.3 Source terms for the governing equations in the PEMFC domains.

Mass Source Terms		
Part	**Term**	**Expression**
CL	S_m	$\sum_i S_i = \sum_i (S_\mathrm{react,i} + S_\mathrm{prod,i} + S_\mathrm{ads/des,i})$
Species Source Terms		
CL Anode	$S_{reactant}$	$-\frac{j_a}{2F} M_{\mathrm{H_2}}$
	$S_{ads/des}$	$\nabla \left(\frac{n_e^a \sigma_e^\mathrm{eff} \nabla \Phi_e}{F} \right) M_{\mathrm{H_2O}}$
CL Cathode	S_reactant	$-\frac{j_c}{4F} M_{\mathrm{O_2}}$
	S_product	$\frac{j_c}{2F} M_{\mathrm{H_2O}}$
	$S_{ads/des}$	$\nabla \left(\frac{n_e^c \sigma_e^\mathrm{eff} \nabla \Phi_e}{F} \right) M_{\mathrm{H_2O}}$
Momentum Source Terms		
Part	**Term**	**Expression**
pl: CL, GDL, MPL	S_P	$\left(-\frac{\mu_\mathrm{n}}{K_\mathrm{pl} \cdot \alpha_\mathrm{m}^3} \right) \vec{u}_\mathrm{pl}$
pl: CL, GDL, MPL	S_U	$\alpha_\mathrm{n} \alpha_\mathrm{m} \cdot \sigma \cos(\theta_\mathrm{pl}) \sqrt{\left(\frac{\chi}{K}\right)_\mathrm{pl}} \nabla(J(\alpha_\mathrm{n}))$
Energy Source Terms		
Part	**Term**	**Expression**
CL Anode	S_T	$j_\mathrm{an} \lvert \eta_\mathrm{act} \rvert + \frac{j_\mathrm{ele}^2}{\kappa^\mathrm{eff}} + \frac{j_\mathrm{ion}^2}{\sigma^\mathrm{eff}}$
CL Cathode	S_T	$j_\mathrm{cat} \lvert \eta_\mathrm{act} \rvert + \frac{j_\mathrm{ele}^2}{\kappa^\mathrm{eff}} + \frac{j_\mathrm{ion}^2}{\sigma^\mathrm{eff}} + \frac{j_\mathrm{cat} T \Delta S}{2F}$
GDL/MPL/solids	S_T	$\frac{j_\mathrm{ele}^2}{\kappa^\mathrm{eff}}$
MEM	S_T	$\frac{j_\mathrm{ion}^2}{\sigma^\mathrm{eff}}$
Charge Conservation Source Terms		
Part	**Term**	**Expression**
CL Anode	S_{Φ_sol}	$-j_\mathrm{an}$
	S_{Φ_mem}	j_an
CL Cathode	S_{Φ_sol}	j_cat
	S_{Φ_mem}	$-j_\mathrm{cat}$

6.3 Application of the V&V Methodology

The verification and validation procedure described in Chapter 2 is applied to the PEMFC case study in order to assess the reliability of the three CFD models and to quantify the associated numerical and validation uncertainties. The analysis is performed consistently across STAR-CCM+, ANSYS Fluent and OpenFOAM. Code verification is not addressed, as the solvers are assumed to be previously verified. The focus is therefore placed on solution verification and validation.

Quantities of interest Two quantities of interest are considered. The primary QoI is the mean current density, expressed in A/cm^2, which represents the electrochemical performance of the cell and can be directly compared with experimental measurements. The second QoI is the mean liquid water saturation within the porous media, which provides insight into water management but is not available from the experimental dataset. The current density is evaluated differently depending on the solver formulation: in Fluent and OpenFOAM it is computed as a volumetric average within the catalyst layers, while in STAR-CCM+ it is evaluated as a surface quantity at the CL/MEM interface, consistently with the underlying electrochemical model.

Solution Verification Solution verification is carried out through a systematic grid refinement study following the five-step procedure described in Chapter 2. Given the zero-gradient configuration of the PEMFC [31], variations along the channel direction are negligible. Therefore, grid refinement is applied exclusively in the through-plane direction and limited to the porous regions, where the relevant transport and electrochemical processes take place. The computational grids have been generated using the *blockMesh* utility in OpenFOAM and subsequently imported into STAR-CCM+ and ANSYS Fluent as separate *.msh* files (one for each domain region). The use of identical meshes across all solvers ensures a consistent basis for the code-to-code comparison. The grid is composed of structured hexahedral elements and is conformal across all regions of the computational domain. As shown in fig. 6.2, refinement is concentrated in the porous layers along the through-plane direction in order to accurately resolve gradients in species concentration and electric potential, while the discretization in the channels and solid regions is kept unchanged.

The representative grid size h_i adopted for all quantities of interest is defined as

$$h_i = \frac{1}{N_i} \tag{6.1}$$

where N_i is the total number of computational cells in the through-plane direction and the subscript i identifies the grid level, with $i = 1$ corresponding to the finest grid and $i = 4$ to the coarsest. The refinement ratio between two consecutive grids, for example between grids 1 and 2, is defined as

$$r_{21} = \frac{h_2}{h_1}. \tag{6.2}$$

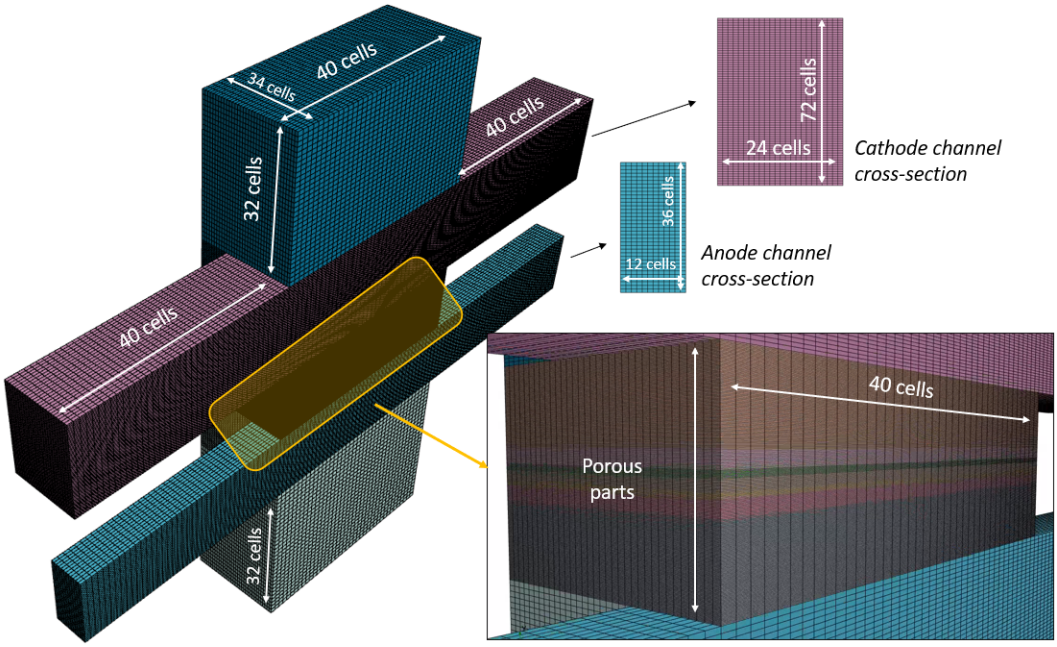


Fig. 6.2 Details of the computational grid of the PEMFC segment common to the three software. Grid refinement is performed only in the porous zone in the through-plane direction.

Four progressively coarsened grids are generated by systematically reducing the number of cells in the through-plane direction of each porous layer, while preserving the same geometric thickness. The number of cells adopted in each region is reported in table 6.4, while the corresponding grid sizes h_i and refinement ratios r_{ji} are reported in table 6.5. A visual comparison of the through-plane grid distributions is provided in Fig. 6.3.

Table 6.4 Number of computational cells in the through-plane direction adopted for each grid.

Part	**Thickness** [μm]	**Number of cells**			
		g1	**g2**	**g3**	**g4**
GDL_{cat}	117	174	116	83	50
MPL_{cat}	22	31	21	15	9
CL_{cat}	10	15	11	8	5
Membrane	15	21	14	10	6
CL_{an}	7	10	7	5	3
MPL_{an}	22	31	21	15	9
GDL_{an}	117	174	116	83	50
Total	**310**	**456**	**306**	**219**	**132**

Table 6.5 Representative grid size and refinement ratios for the grid convergence study.

	g1	**g2**	**g3**	**g4**
h_i (-)	2.19	3.27	4.57	7.58
r_{ji} (-)	–	1.49	1.40	1.66

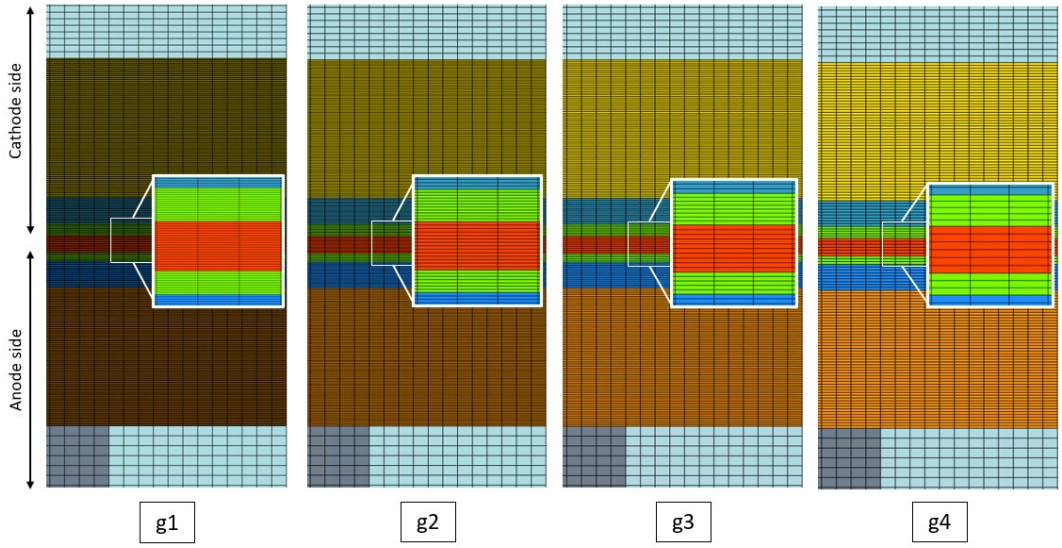


Fig. 6.3 Through-plane cross-sections of the different computational grid refinements adopted in the solution verification.

The analysis is performed at the operating point corresponding to a cell voltage of 0.7 V and the results of the solution verification procedure are summarized in Table 6.6, where the metrics are reported for both QoIs and for all solvers. Fluent shows a consistent convergence behavior, with observed orders close to the theoretical second-order accuracy and low numerical uncertainties (below 0.2% for both QoIs). STAR-CCM+ exhibits acceptable convergence for the current density on the finest grid set, while the liquid saturation shows inconsistent behavior, with observed orders outside the expected range. The very low numerical uncertainty obtained for the current density in STAR-CCM+ is attributed to the two-dimensional treatment of electrochemical reactions at the CL/MEM interface, which is not affected by through-plane grid refinement. OpenFOAM with the Euler-Euler multiphase model exhibits non-monotonic convergence for both QoIs, with unrealistic values of the observed order p. Accordingly, the grid-convergence results that do not satisfy the conditions required by the adopted V&V procedure are not considered applicable for the estimation of the corresponding discretization uncertainty. As shown in fig. 6.4,

this behavior is associated with a significant overprediction of liquid water saturation compared to the other solvers. To further investigate this issue, an additional set of simulations is performed using a single-phase formulation, which restores a consistent convergence behavior for the current density but prevents a direct code-to-code comparison. The normalized trends of the QoIs as a function of grid refinement are reported in Fig. 6.5, highlighting the different convergence behaviors across the solvers.

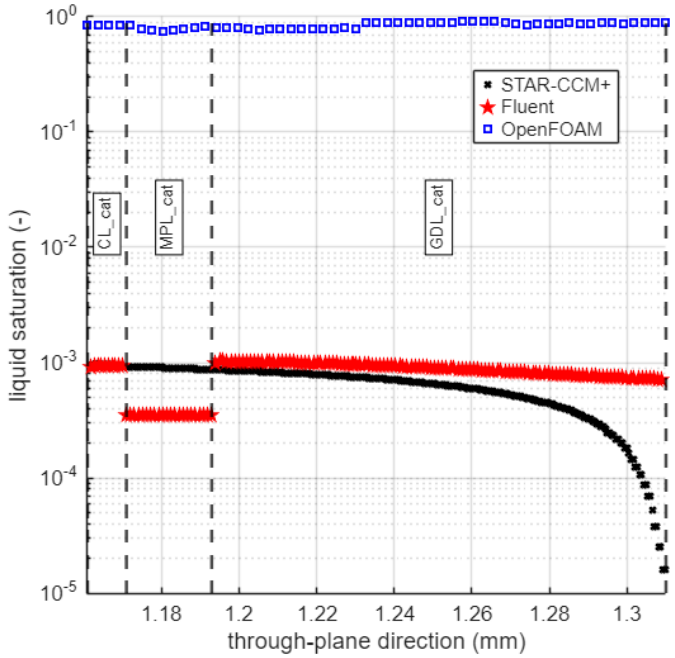


Fig. 6.4 Local profiles of liquid water saturation along the cathode porous layers for Fluent (red), STAR-CCM+ (black), and OpenFOAM multi-phase model (blue).

Validation and Uncertainty Quantification In the second part of the analysis, the numerical model is assessed against experimental data in order to evaluate its predictive capability under realistic operating conditions. The validation is performed on a configuration representative of a single PEMFC segment, consistently with the modeling assumptions adopted in the previous sections.

The quantity of interest selected for validation is the mean current density, extracted from the polarization curve as a function of the imposed cell voltage. This represents the only global measurable quantity available from the experimental campaign for the present case. In contrast, internal fields such as species concentrations,

electric potential distribution, and liquid water saturation within the porous layers are not experimentally accessible and therefore cannot be directly validated. As a consequence, the validation exercise is limited to integral quantities, while local discrepancies inside the cell cannot be explicitly assessed. The validation point is defined at a cell voltage of 0.7 V, corresponding to a representative operating condition in the ohmic region of the polarization curve. This choice is consistent with the verification analysis, allowing the direct propagation of the numerical uncertainty previously quantified.

All simulations are performed using the computational grid identified during the solution verification step, ensuring that discretization errors are properly controlled. The same geometry, material properties, and boundary conditions described in the modeling section are retained without any parameter tuning or calibration against the validation dataset, in accordance with the V&V best practices. The comparison between numerical predictions and experimental data is performed on the polarization curve, by extracting the simulated current density at the validation voltage and comparing it with the corresponding experimental value. Additional comparisons over the full polarization curve are also considered to provide a broader assessment of the model behavior across different operating regimes. Regarding the uncertainty quantification, the experimental uncertainty associated with the current density measurements is assumed equal to 5%, based on the available information from the experimental campaign. The numerical uncertainty u_{num} is directly obtained from the grid convergence study. A rigorous estimation of the input uncertainty would require a sensitivity analysis over a large number of model parameters, including electrochemical kinetics, transport properties, and material characteristics. However, due to the high dimensionality of the parameter space and the lack of detailed information on the associated uncertainties, this contribution is not explicitly quantified. Instead, input-related uncertainties are implicitly included in the model discrepancy. As a result, the validation uncertainty is evaluated by combining only numerical and experimental contributions. The validation results, expressed in terms of comparison error and associated uncertainty, are summarized in Table 6.7. The comparison is performed separately for each solver in order to highlight possible differences arising from numerical implementation and model formulation. Figure **??** reports the comparison between numerical and experimental polarization curves, while Fig. **??** shows the corresponding comparison error at the validation point together with the associated uncertainty bounds.

From a qualitative standpoint, the different solvers show varying levels of agreement with the experimental data across the polarization curve. In the ohmic region, the predictions are generally consistent, indicating a coherent representation of transport phenomena and electrical conduction. Larger discrepancies may be observed in the high-voltage region, where the solution is more sensitive to the electrochemical kinetics and to the numerical treatment of thin reactive layers. It is important to emphasize that graphical agreement alone is not sufficient to assess model validity. The validation assessment is based on the comparison error evaluated at the selected operating point and its consistency with the associated uncertainty bounds. This allows distinguishing between discrepancies attributable to uncertainty and those related to potential model deficiencies. The differences observed among the solvers are discussed in detail in the following section.

6.4 Model Credibility and Discussion

The application of the verification and validation (V&V) methodology to the present PEMFC case study provides a structured framework to assess the credibility of the numerical results beyond a purely qualitative comparison with experimental data. The analysis highlights how the predictive capability of the model is not solely determined by the choice of the CFD software, but rather by the consistency between numerical methods, physical modeling assumptions, and the level of verification evidence supporting the simulation outcomes. From the solution verification perspective, significant differences emerge among the investigated tools. ANSYS Fluent exhibits the most consistent numerical behaviour, with observed orders of convergence close to the expected theoretical value for both quantities of interest. STAR-CCM+ shows satisfactory performance for the current density prediction, while a degradation in convergence behaviour is observed for liquid saturation, suggesting a reduced numerical accuracy for multiphase transport. A more critical behaviour is observed for OpenFOAM when the Euler–Euler multiphase formulation implemented in the *openFuelCell* framework is adopted.In this configuration, the solution does not satisfy the grid convergence requirements, as indicated by non-physical observed orders of convergence; consequently, the corresponding discretization uncertainty cannot be reliably estimated. This result points to numerical instabilities associated with the multiphase formulation under the investigated operating conditions, ultimately

preventing a reliable estimation of the discretization error. However, when the model is simplified to a single-phase formulation, OpenFOAM recovers a consistent convergence behaviour, with observed orders close to the theoretical expectation. This outcome clearly indicates that model credibility depends primarily on the compatibility between the numerical formulation and the underlying physical assumptions, rather than on the software itself. Validation is performed at a reference operating point corresponding to a cell voltage of 0.7 V, consistently with the availability of experimental data. The analysis is based on the comparison error E and the associated validation uncertainty u_{val}, in accordance with the V&V framework. It is important to stress that only the current density can be validated, as no experimental measurements are available for liquid water saturation in the porous media. The liquid water saturation is therefore considered only within the solution verification and code-to-code comparison framework, and no validation claim is made for this quantity. This limitation represents a relevant constraint, as it prevents a direct assessment of the multiphase transport model, which remains only indirectly evaluated through its impact on the current density prediction. The validation results show that, in the ohmic region, all solvers provide comparable predictions, with modeling errors generally within -30%. This indicates a consistent representation of transport processes, such as ionic and electronic conduction, across the different tools. In contrast, larger discrepancies are observed in the kinetic region, where the modeling error increases significantly. OpenFOAM (single-phase) exhibits the largest deviations, while Fluent shows intermediate discrepancies. STAR-CCM+ provides the most accurate predictions in this regime, with relatively smaller errors. Despite the large relative differences, it is worth noting that the corresponding absolute errors remain limited due to the low magnitude of the current density in this region.

These discrepancies highlight the sensitivity of the solution to the electrochemical modeling, suggesting that differences in the implementation of kinetic expressions, as well as in the numerical treatment of thin layers such as catalyst layers and membrane interfaces, play a dominant role. This aspect is particularly critical in PEMFC simulations, where multiple coupled physical phenomena coexist and interact at different scales. Another important aspect emerging from the analysis concerns the role of input uncertainty. In the present work, input uncertainties are not explicitly quantified due to the large number of parameters involved and the lack of detailed uncertainty estimates. As a consequence, they are implicitly embedded within the modeling error. While this approach simplifies the analysis,

it also limits the interpretability of the validation results, as it becomes difficult to distinguish between discrepancies arising from model inadequacy and those related to uncertain input parameters. From a V&V standpoint, it is essential to emphasize that reducing the comparison error through parameter tuning does not constitute validation. Calibration and validation must remain distinct processes. Calibration aims at adjusting model parameters to reproduce a given dataset, whereas validation evaluates the predictive capability of the model against independent experimental data. Failing to maintain this separation compromises the credibility of the model and prevents a rigorous assessment of its reliability. Overall, the results of this case study underline that achieving credible PEMFC simulations requires a balanced combination of accurate physical modeling, robust numerical methods, and systematic verification and validation procedures. The analysis demonstrates that even advanced multiphase models may lead to unreliable results if not properly verified, while simpler modeling approaches can provide credible predictions when supported by consistent numerical behaviour. Finally, the study highlights the importance of adopting standardized V&V practices and benchmark configurations to enable meaningful comparisons between different modeling approaches and software tools. Future work should focus on the explicit quantification of input uncertainties, the improvement of multiphase transport models, and the validation against independent experimental datasets. Such efforts are essential to strengthen the predictive capability of PEMFC simulations and to support their use in design and optimization applications.

Table 6.6 Metrics of the 5-steps procedure of the solution verification considering the current density (A/cm^2) and liquid saturation (-) of the PEMFC under investigation.

	Current density (A/cm^2)				**Liquid saturation**		
Metric	**STAR-CCM+**	**Fluent**	**OpenFOAM 2-phase**	**OpenFOAM 1-phase**	**STAR-CCM+**	**Fluent**	**OpenFOAM 2-phase**
p_{123} (-)	2.11	2.33	11.8	1.91	0.35	1.60	−0.61
p_{234} (-)	12.6	1.98	−12.4	1.80	10.2	2.71	3.25
ϕ_{ext} (A/cm^2)	1.30	1.13	~~1.57~~	1.27	~~0.0012~~	0.0158	~~0.0480~~
ε_{ext} (A/cm^2)	3.8×10^{-5}	1.3×10^{-3}	~~9.9×10^{-5}~~	2.2×10^{-3}	~~9.5×10^{-5}~~	2.2×10^{-5}	~~1.79×10^{-2}~~
ε_{ext} (%)	0.003	0.12	~~0.006~~	0.17	~~7.91~~	0.14	~~37.37~~
ε_{21} (A/cm^2)	5.0×10^{-5}	2.0×10^{-3}	~~1.1×10^{-2}~~	2.5×10^{-3}	~~1.4×10^{-5}~~	2.0×10^{-5}	~~1.86×10^{-2}~~
ε_{21} (%)	0.003	0.18	~~0.68~~	0.20	~~1.28~~	0.13	~~62.01~~
GCI_{21} (%)	0.003	0.14	~~0.008~~	0.22	~~10.7~~	0.18	~~−359~~

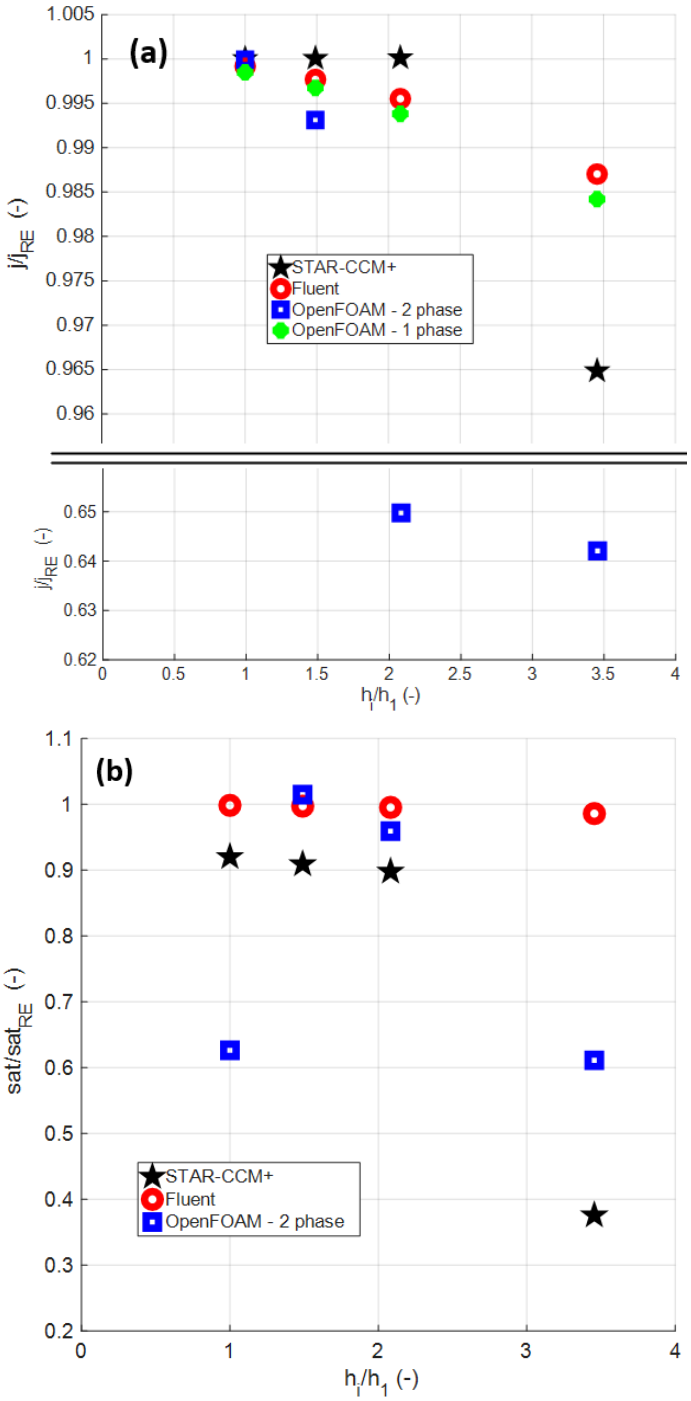


Fig. 6.5 Current density (a) and liquid saturation (b) normalized to the respective extrapolated values for Fluent (red), OpenFOAM (blue and green) and STAR-CCM+ (black). In OpenFOAM current density has been computed with a single phase model (green) and two phase model (blue).

Table 6.7 Validation uncertainties and comparison errors computed for the current density at the validation point of $0.7V$ for the three software.

Metric	**STAR-CCM+**	**Fluent**	**OpenFOAM 1-phase**
u_{num} (%)	0.003	0.14	0.22
u_D (%)	5.0	5.0	5.0
u_{val} (%)	5.0	5.0	5.0
ϕ_{exp} (A/cm^2)	1.5		
ϕ_{CFD} (A/cm^2)	1.30	1.13	1.43
E (A/cm^2)	-0.20	-0.37	-0.07
E (%)	-13.5	-24.7	-4.5

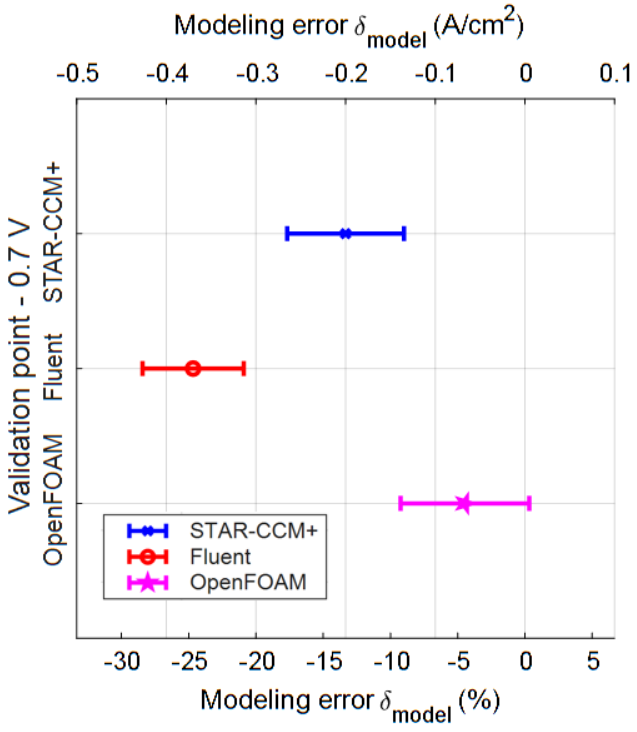


Fig. 6.6 Comparison error computed at the validation point for STAR-CCM+ (blue), Fluent (red) and OpenFOAM (magenta). Modeling error expressed in absolute value on top axis and in percentage terms on the bottom axis.

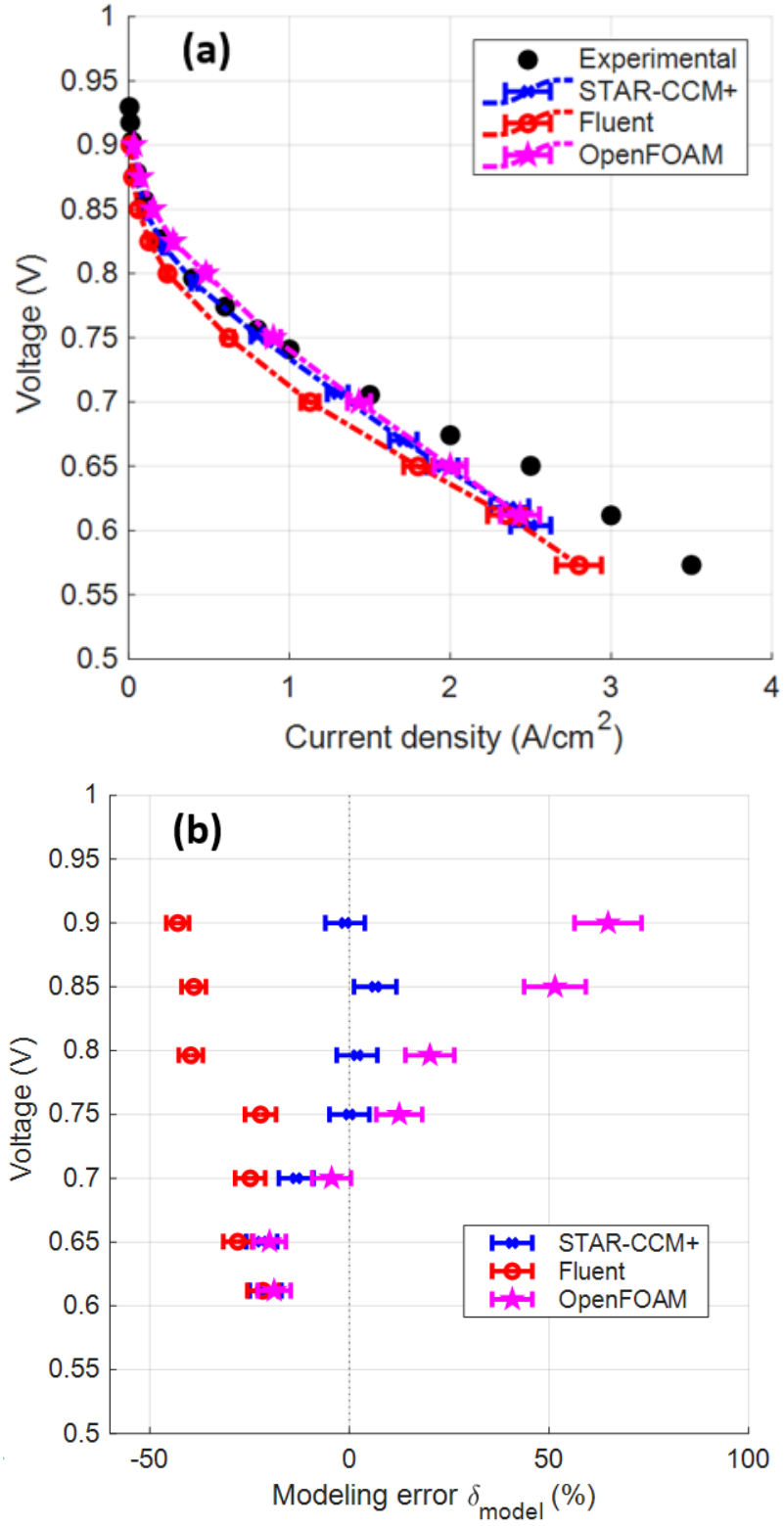


Fig. 6.7 Polarization curve (a), provided with validation uncertainty, and modeling error δ_{model} (b) computed with the most refined grid with the different solvers for the whole polarization curve.

Chapter 7

Discussion and Conclusions

The four case studies considered in this work: the TPMS structures for heat transfer applications, the V-rib turbulence promoter, the transport of tritium in confined environments, and the PEM fuel cell (PEMFC), are not intended as independent application cases, but as complementary testbeds to investigate the applicability of verification and validation (V&V) principles to CFD models of progressively increasing physical and numerical complexity. Despite the diversity in governing physics and numerical formulations, a clear and recurring outcome emerges: model credibility is never determined by a single dominant source of error, but by the combined effect of discretization uncertainty, model-form assumptions, and uncertainty in reference data. In the cases where experimental data are available, meaningful validation is only possible when numerical predictions are interpreted within a quantified uncertainty framework.

Across the validated applications, modelling assumptions and physical representation become increasingly important once numerical convergence is sufficiently controlled, although the relative contribution of each uncertainty source depends strongly on the specific problem and intended use. Discretization errors can become secondary once numerical convergence is sufficiently controlled, whereas modelling assumptions and uncertainties in the physical representation may then become the main limiting factors. This behaviour is observed regardless of physical complexity, from heat transfer-dominated configurations to fully coupled multiphysics systems. Taken together, the four studies therefore provide a common methodological perspective on how V&V can be used to identify, quantify, and interpret the limitations

of CFD predictions rather than simply to establish whether a model is “validated” or “not validated”.

In the TPMS case, geometric idealisation and manufacturing-induced deviations are the primary sources of discrepancy with respect to experimental data. The analysis shows that even small departures from the nominal geometry, inherent to additive manufacturing, can significantly alter pressure drop and heat transfer characteristics, particularly in low-Reynolds-number regimes. Predictive accuracy is therefore strongly linked to geometric fidelity rather than numerical refinement.

In the V-rib configuration, turbulence modelling and thermal boundary conditions represent the dominant sources of uncertainty. While grid refinement ensures numerical convergence, it does not reduce discrepancies arising from incomplete physical modelling. The Reynolds Stress Model provides improved agreement for thermal fields, highlighting the importance of turbulence anisotropy and secondary flow structures in heat transfer prediction.

In the tritium release case, the analysis focuses on transport and dispersion in confined environments under transient flow conditions. The results highlight a strong sensitivity to flow variability and spatial resolution, leading to relatively large numerical uncertainties in the predicted transport behaviour. In the absence of experimental data for the investigated configuration, the assessment is therefore limited to verification and sensitivity considerations.

In the PEMFC case, the complexity of coupled electrochemical, thermal, and multiphase phenomena leads to strong dependence on both physical modelling and numerical implementation. Differences in multiphase formulation and electrochemical source terms result in significant variability across CFD platforms. Validation is further limited by the lack of experimental data for distributed quantities such as liquid water saturation, restricting the analysis to integrated quantities such as current density.

A recurring hierarchy of error sources emerges across the four cases, although its relative importance depends on the physical problem and on the intended use of the model. When numerical convergence is sufficiently controlled, modelling assumptions, geometric fidelity, and uncertainties in the reference or input data may become more important than further mesh refinement. This is particularly evident in the V-rib and PEMFC configurations, where physical modelling choices govern predictive accuracy, while in TPMS systems geometric fidelity plays an equivalent

role. Overall, the results demonstrate that CFD model credibility is inherently conditional and must always be interpreted with respect to the intended application. A model may be suitable for empirical correlation development, require careful physical calibration in conjugate heat transfer problems, or provide only partial predictive capability in fully coupled multiphysics systems. The V&V framework does not provide a binary validation outcome, but a structured quantification of the limits of applicability of numerical models. This aspect is particularly critical in safety-relevant applications involving the transport and release of radioactive species such as tritium in confined environments, where conservative interpretation of CFD results is required due to the potential impact of local concentration errors.

Beyond the individual applications, several methodological considerations can be generalized to CFD studies involving different physical systems. First, verification and validation should be regarded as an iterative process rather than as a final step performed after the numerical model has been developed. The identification of dominant uncertainty sources can in fact guide subsequent modelling choices, mesh refinement, experimental design, and the definition of the quantities of interest. Second, the level of V&V effort should be proportional to the intended use of the model: not all applications require the same degree of verification detail or experimental validation. Finally, the interpretation of uncertainty should remain closely connected to the engineering decision supported by the simulation. A relatively large uncertainty may be acceptable for the identification of qualitative trends or preliminary design, while the same uncertainty may be unacceptable for safety-critical predictions or local quantities used for design margins. These considerations are not specific to the physical systems investigated in this thesis and can be extended to a broad range of CFD applications.

Future developments should focus on extending the present methodology in three main directions. First, input and model-form uncertainties should be quantified more explicitly, particularly for complex multiphysics problems where they may dominate the overall uncertainty budget. Second, the integration of V&V activities with more systematic uncertainty propagation and sensitivity analysis could provide a more efficient allocation of computational and experimental resources. Third, further benchmark and validation datasets covering different physical regimes would be valuable to enable more systematic comparisons between modeling approaches and CFD software. These developments would also support the progressive integration

of V&V procedures into engineering workflows, where the level of analysis can be adapted to the intended use and required confidence of the simulation.

In conclusion, the results of this thesis show that systematic verification and validation is not merely a procedure for assessing the accuracy of individual CFD models, but a general methodology for understanding their predictive capabilities and limitations. Across the four case studies, the V&V framework provides a common basis to distinguish numerical errors from modeling assumptions and uncertainties in reference data, and to relate these sources of uncertainty to the intended use of the model. Its value therefore extends beyond the specific applications investigated here: when appropriately tailored to the physical problem and engineering objective, V&V can support more transparent, efficient, and defensible use of CFD as a predictive engineering tool.

References

[1] H. Pourrahmani, M. Siavashi, A. Yavarinasab, M. Matian, N. Chitgar, L. Wang, and J. Van Herle. A review on the long-term performance of proton exchange membrane fuel cells: From degradation modeling to the effects of bipolar plates, sealings, and contaminants. *Energies*, 15(14):5081, 2022.

[2] A. d'Adamo, M. Haslinger, G. Corda, J. Höflinger, S. Fontanesi, and T. Lauer. Modelling methods and validation techniques for cfd simulations of pem fuel cells. *Processes*, 9(4):688, 2021.

[3] Kui Jiao and Xianguo Li. Water transport in polymer electrolyte membrane fuel cells. *Progress in Energy and Combustion Science*, 37(3):221–291, 2011.

[4] Shidong Zhang, Steffen Hess, Holger Marschall, Uwe Reimer, Steven Beale, and Werner Lehnert. openfuelcell2: A new computational tool for fuel cells, electrolyzers, and other electrochemical devices and processes. *Computer Physics Communications*, 298:109092, 2024.

[5] Amedeo Grimaldi. *Modelling and experimental analysis of PEM fuel cells under dynamic real-world conditions focusing on the design of an air humidifier*. PhD thesis, Politecnico di Milano, 2021.

[6] R. Bock, A. D. Shum, X. Xiao, H. Karoliussen, et al. Thermal conductivity and compaction of gdl-mpl interfacial composite material. *Journal of The Electrochemical Society*, 165(F7):F514–F525, 2018.

[7] P. Sarkezi-Selsky, H. Schmies, A. Latz, and T. Jahnke. Lattice boltzmann simulation of liquid water transport in gas diffusion layers of proton exchange membrane fuel cells: Impact of gas diffusion layer and microporous layer degradation on effective transport properties. *Journal of Power Sources*, 556:232415, 2023.

[8] William L. Oberkampf and Timothy G. Trucano. Verification and validation in computational fluid dynamics. *Progress in Aerospace Sciences*, 38(3):209–272, 2002.

[9] Patrick J. Roache. *Fundamentals of verification and validation*. Hermosa Publishing, 2009.

[10] L. Eça and M. Hoekstra. On the influence of the iterative error in the numerical uncertainty of ship viscous flow calculations. In *Proceedings of the 26th Symposium on Naval Hydrodynamics*, 2006. Held 2004.

[11] ASME Committee V&V 20. Standard for verification and validation in computational fluid dynamics and heat transfer, 2009. ASME V&V 20-2009.

[12] Valerio Gaioni. A practical verification and validation procedure for computational fluid dynamics. Master's thesis, Universidad Politécnica de Madrid, 2020.

[13] L. Savoldi, A. Cammi, W. Ferretto, A. Quamori Tanzi, and L. Marocco. Use of triply periodic minimal surface lattices for heat transfer applications: A systematic literature investigation. *Energies*, 19:833, 2026.

[14] E. Gajetti, G. Boccardo, L. Savoldi, and L. Marocco. Hydrodynamic characterization of gyroid, diamond and split-p triply periodic minimal surfaces as porous medium. *International Journal of Heat and Mass Transfer*, 252:127439, 2025.

[15] L. Savoldi, A. Cammi, E. Gajetti, and L. Marocco. Investigating the reynolds analogy for triply periodic minimal surfaces in low-reynolds flow regime.

[16] E. Gajetti, M. Bonesso, A. Bruschi, F. Fanale, S. Garavaglia, G. Granucci, A. Moro, A. Pepato, A. Romano, and L. Savoldi. A new efficient mirror cooling for the transmission line of fusion reactor ech systems based on triply periodic minimal surfaces. *IEEE Transactions on Plasma Science*, 52:3765–3771, 2024.

[17] A. Quamori Tanzi, A. Cammi, L. Marocco, and L. Savoldi. Design of a 10 mw/m^2-heat-flux removal system for a w7-x divertor tile using triply periodic minimal surfaces. *Case Studies in Thermal Engineering*, 63:105405, 2024.

[18] A. Quamori Tanzi, A. Cammi, W. Ferretto, L. D. Marocco, L. Molinaroli, A. Trotta, L. Savoldi, and M. Group. A modular approach for the design of a salt-to-salt heat exchanger with 3d-printed triply periodic minimal surfaces for future fusion machines. *IEEE Transactions on Plasma Science*, 2026. to appear.

[19] R. Diperna, A. Di Benedetto, S. De Palo, F. Giuffrida, V. Lavopa, M. Moretto, B. Puddu, A. Quaranta, and L. Savoldi. Optimization of a lightweight gyroid-based heat exchanger for space applications. In *International Conference on Fluid Flow and Thermal Science*, 2026.

[20] E. Gajetti, A. Bruschi, F. Fanale, W. Ferretto, G. Granucci, A. Lucchini, L. Marocco, A. Romano, and L. Savoldi. Design, manufacturing and experimental characterization of a first-of-a-kind dtt ech mirror equipped with tpms. *IEEE Transactions on Plasma Science*, 2025. submitted.

[21] A. Mortazavi, A. L. Ávila Marín, H. Ebadi, E. Gajetti, C. Piatti, L. Marocco, and L. Savoldi. Experimental investigation of triply periodic minimal surfaces for high-temperature solar receivers. *Case Studies in Thermal Engineering*, 60:104771, 2024.

[22] C. Piatti, L. Savoldi, and N. Fathi. Numerical assessment of hydraulic properties of triply periodic minimal surfaces structures. In *ASME Verification, Validation, and Uncertainty Quantification Symposium*, page V001T07A001, Baltimore, Maryland, USA, 2023. ASME.

[23] C. Piatti, A. Hicks, E. Gajetti, C. Ward, M. Pourghasemi, L. Marocco, L. Savoldi, and N. Fathi. Verification and validation of turbulence modeling of flow through triply periodic minimal surfaces porous structures. In *ASME Verification, Validation, and Uncertainty Quantification Symposium*, page V001T02A002, College Station, Texas, USA, 2024. ASME.

[24] C. Piatti, V. Gentile, W. Ferretto, L. Marocco, A. Lucchini, and L. Savoldi. Hydraulic characterization of solar receivers samples with tpms lattices. *Results in Engineering*, 2026. submitted.

[25] A. Mortazavi, H. Ebadi, C. Piatti, E. Gajetti, L. Marocco, and L. Savoldi. Numerical modelling of solar receivers equipped with tpms structures. In *SolarPACES Conference Proceedings*, volume 3, 2025.

[26] EUROfusion Work Package Breeding Blanket. R&d on helium cooled first wall thermal-hydraulics. Technical Report WPBB-DEL-BB-8.3.2-T002-D001, EUROfusion, 2021. Project WPBB, Deliverable ID1 BB-8.3.2-T002-D001. Project Leader: L. V. Boccaccini; Task Coordinator: Z. Vizvary; RU of TC: CCFE.

[27] Siemens Digital Industries Software. Simcenter star-ccm+, version 2310, 2023.

[28] Fusion for Energy (F4E). Technical report for room #02 tritium detection within the process rooms. Technical Report 17213 / TRP_002 Ed. 3.0A, Fusion for Energy (F4E), November 2012.

[29] ANSYS Inc. Ansys fluent release 2306 documentation, 2023.

[30] OpenFOAM Foundation. *OpenFOAM User Guide, Version 2306*. The OpenFOAM Foundation Ltd., 2023. Available at: https://www.openfoam.com/documentation/user-guide.

[31] Elena Colombo, Delio Casadei, Andrea Baricci, and Andrea Casalegno. An open-source zero-gradient cell hardware to improve and accelerate durability testing of pem fuel cells. *HardwareX*, 16:e00495, 2023.

[32] Margherita Bulgarini, Augusto Della Torre, Andrea Baricci, Amedeo Grimaldi, Luca Marocco, Riccardo Mereu, Gianluca Montenegro, and Angelo Onorati. Computational fluid dynamic investigation of local flow-field conditions in lab polymer electrolyte membrane fuel cells to identify degradation stressors and performance enhancers. *Energies*, 17(15):3643, 2024.

[33] F.A.L. Dullien. *Porous Media: Fluid Transport and Pore Structure*. Academic Press, San Diego, CA, USA, 2nd edition, 1992.

[34] M. C. Leverett. Capillary behavior in porous solids. *Transactions of the American Institute of Mining, Metallurgical, and Petroleum Engineers*, 142:151–169, 1941.

[35] Edward N. Fuller, Paul D. Schettler, and J. Calvin Giddings. A new method for prediction of binary gas-phase diffusion coefficients. *Industrial & Engineering Chemistry*, 58(5):19–27, 1966.

[36] T. E. Springer, T. A. Zawodzinski, and S. Gottesfeld. Polymer electrolyte fuel cell model. *Journal of The Electrochemical Society*, 138(8):2334, 1991.

[37] H. Wu, X. Li, and P. Berg. On the modeling of water transport in polymer electrolyte membrane fuel cells. *Electrochimica Acta*, 54:6913–6927, 2009.

[38] Francesco Verducci, Amedeo Grimaldi, Elena Colombo, Andrea Casalegno, and Andrea Baricci. Dynamic modeling of polymer electrolyte membrane fuel cells under real-world automotive driving cycle with experimental validation on segmented single cell. *Renewable Energy*, 234:121194, 2024.

[39] Viktor Hacker and Shigenori Mitsushima, editors. *Fuel Cells and Hydrogen: From Fundamentals to Applied Research*. Elsevier, Amsterdam, 1st edition, 2018.

[40] Shingo Jomori, Nobuhiro Nonoyama, and Toshiaki Yoshida. Analysis and modeling of pemfc degradation: Effect on oxygen transport. *Journal of Power Sources*, 215:18–27, 2012.

[41] Alireza Goshtasbi, Pablo García-Salaberri, Jixin Chen, Krishan Talukdar, Daniel G. Sanchez, and Tulga Ersal. Through-the-membrane transient phenomena in pem fuel cellls: A modeling study. *Journal of The Electrochemical Society*, 166(7):F3154, 2019.

.1 Appendix A - V-rib Geometry and CFD Results

This appendix collects the main geometric features and numerical results obtained for the V-rib configuration. The geometry is derived from the experimental setup used in the HETREX-PT campaign and reproduced in the numerical model based on the available CAD representation and technical drawings of the test section. A simplified representation of the ribbed channel and of the corresponding computational domain is reported in Figures 1 and 2.

The simulations include both turbulence models considered in the study (RSM and Lag-EB), and all fields are reported using consistent color scales to allow direct qualitative comparison. In particular, differences in velocity and temperature distributions are highlighted to support the discussion presented in the main text.

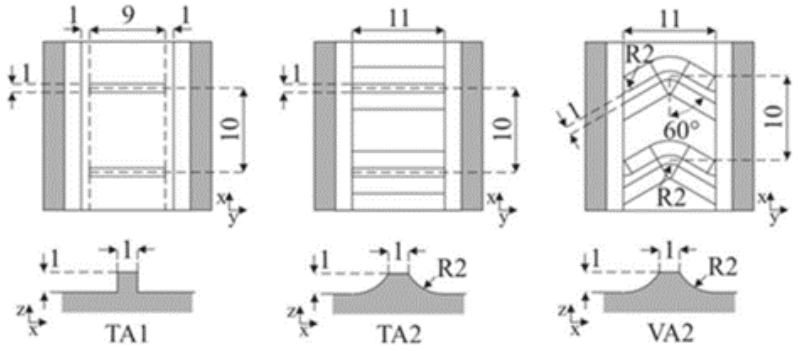


Fig. 1 V-rib geometry with main geometric parameters and rib orientation as implemented in the numerical model based on the experimental design specifications.

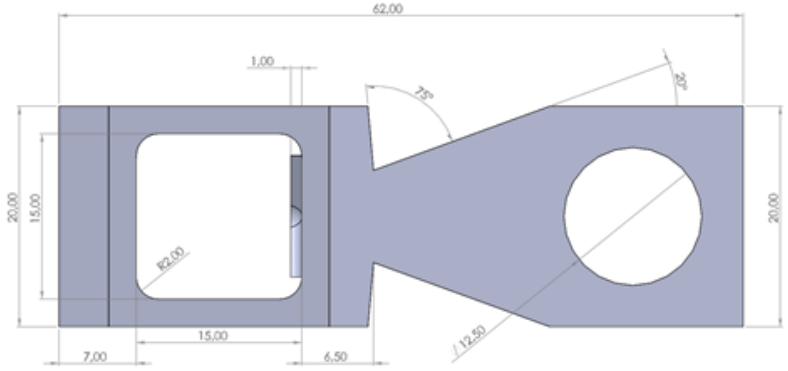


Fig. 2 Section view of the computational domain derived from the experimental test section. The modeled configuration reproduces the main features of the HETREX-PT setup, including the heated channel and flow direction.

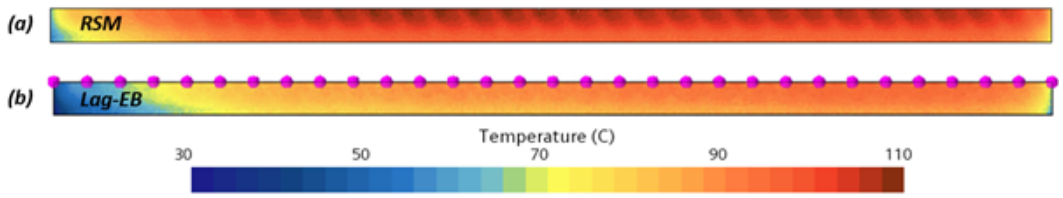


Fig. 3 Temperature field at the heated wall computed with RSM (a) and Lag-EB (b). The comparison highlights differences in thermal spreading and local heat transfer enhancement induced by the turbulence closure.

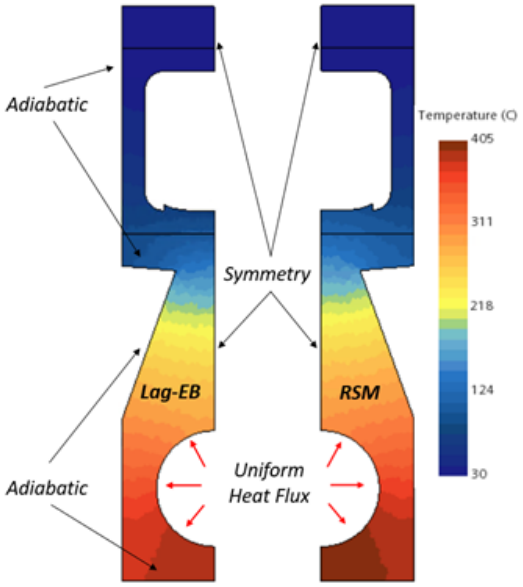


Fig. 4 Temperature distribution on a representative cross-section of the channel computed with RSM (a) and Lag-EB (b), showing differences in thermal mixing and boundary layer development.

The results reported in this appendix provide additional insight into the flow structure and thermal development within the V-rib channel. The velocity field shows a strong dependency on the turbulence model: the Lag-EB model predicts a more concentrated high-velocity region shifted away from the ribbed wall, while the RSM model produces a more diffused and laterally redistributed flow pattern, with a tendency toward a more uniform, non-circular core region. These differences directly influence the near-wall transport mechanisms and therefore the predicted heat transfer behavior.

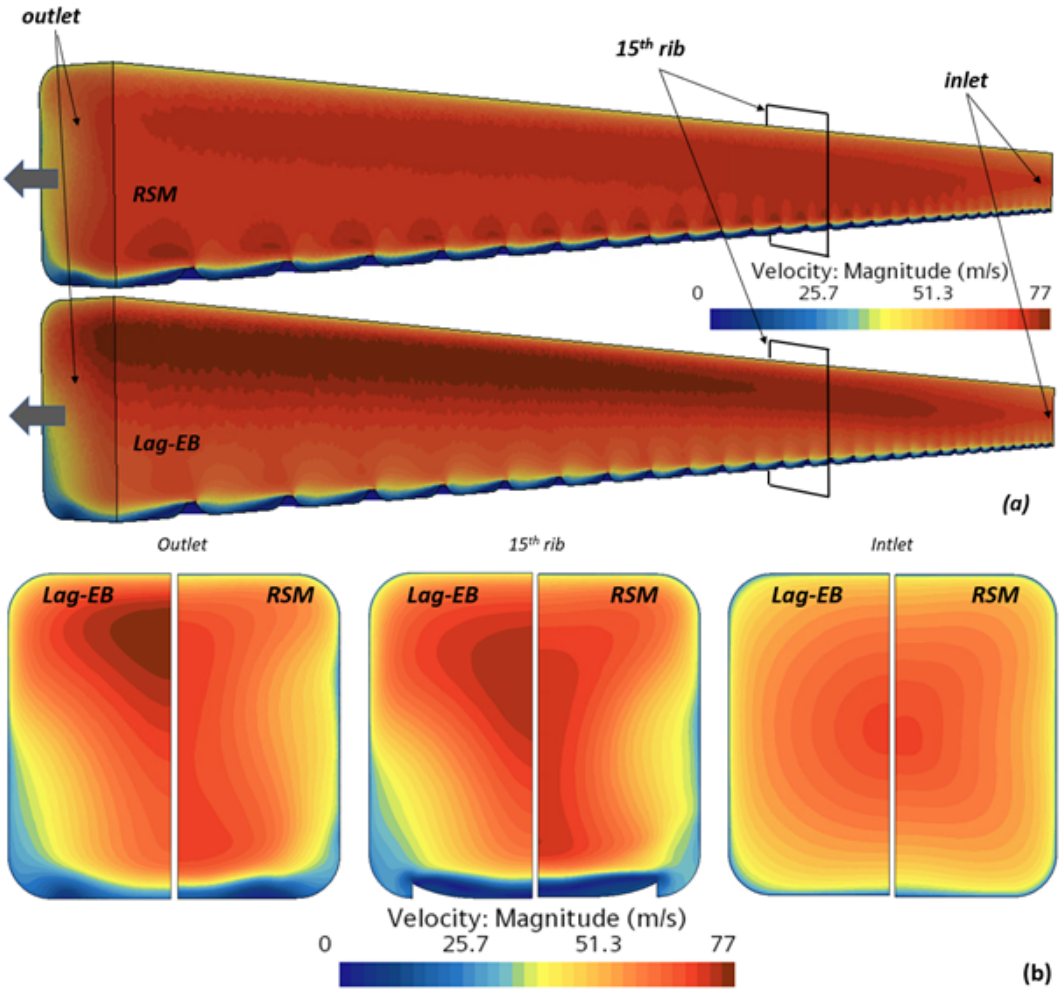


Fig. 5 Velocity field computed with RSM and Lag-EB turbulence models. Top: full domain representation. Bottom: selected cross-sections at inlet (right), mid-plane (center), and outlet (left), illustrating differences in flow redistribution induced by the rib structures.

.2 Appendix 2 - PEM Fuel Cell Physics and Numerical Implementation

This appendix summarizes the main physical models adopted for the PEM fuel cell simulations, with particular focus on multiphase transport, species conservation, and ionomer water content modeling. The formulation is presented in a general framework, while specific implementation details in different CFD solvers are discussed where relevant.

Multiphase flow modeling

Euler–Euler multiphase approach

A general Euler–Euler multiphase formulation can be adopted to describe gas–liquid transport in porous and free-flow regions. In this framework, gas and liquid phases are treated as interpenetrating continua, each governed by its own set of mass and momentum conservation equations. Interphase interactions are modeled through closure relations accounting for capillary pressure, relative permeability, and phase change phenomena such as condensation and evaporation. This formulation allows a detailed resolution of phase dynamics at the cost of increased computational effort. A more efficient alternative is the mixture-based formulation described in the following section [32].

Mixture multi-phase model

In PEM fuel cells, water may exist in multiple forms: liquid and vapor in gas channels and porous media, and dissolved water within the ionomer phase of the membrane. In the mixture multi-phase (MMP) approach, liquid and vapor phases are assumed to be in local thermodynamic equilibrium and are treated as a single effective fluid with density ρ_{mix} and velocity $\mathbf{u}_{\text{mix}}$, while phase fractions are tracked separately. This approach is suitable for low liquid saturation regimes, such as those considered in the present work, but may become less accurate in highly saturated conditions [2]. The mixture mass conservation equation includes a source term S_m, representing electrochemical reactions and sorption/desorption mechanisms:

$$S_m = \sum_i S_i = \sum_i \left(S_{\text{reactants},i} + S_{\text{products},i} + S_{\text{ads/des},i} \right) \tag{1}$$

The momentum equation includes porous media resistance through a Darcy–Forchheimer formulation [33]:

$$S_P = -\left(P_{\text{vis}} + P_{\text{in}} \cdot |\mathbf{u}_{\text{mix}}| \right) \mathbf{u}_{\text{mix}} \tag{2}$$

In low-velocity regimes, the inertial contribution is neglected. The viscous resistance is defined as:

$$P_{\text{vis},n} = \frac{\mu_n}{K_{\text{pl}} \cdot \alpha_n^3} \tag{3}$$

where μ_n is the phase viscosity, α_n is the volume fraction, and K_{pl} is the permeability of the porous layer.

Capillary effects are modeled through a Leverett-type formulation [34]:

$$S_U = \alpha_n \alpha_m \cdot \sigma \cos(\theta_{\text{pl}}) \sqrt{\left(\frac{\chi}{K} \right)_{\text{pl}}} \nabla(J(\alpha_n)) \tag{4}$$

with the Leverett function defined as:

$$J(\alpha_n) = 1.417(1-\alpha_n) - 2.120(1-\alpha_n)^2 + 1.263(1-\alpha_n)^3 \tag{5}$$

Here σ is the surface tension, θ the contact angle, and χ the porosity.

Species transport

Species conservation is governed by advection–diffusion equations (see governing equations in Chapter 6.1). In porous media, transport is dominated by diffusion, modeled via Fick's law using effective diffusion coefficients D_i^{eff}, computed from kinetic theory correlations [35].

Source terms S_i account for electrochemical production/consumption and water sorption/desorption processes in the catalyst layers.

Water content transport in the ionomer phase

In the ionomer phase, water transport is described in terms of water content λ, defined as:

$$\lambda = C_{\mathrm{H_2O^+}} \left(\frac{EW}{\rho} \right)_{\mathrm{mem}} \tag{6}$$

The governing transport equation reads:

$$\nabla \left(\frac{i_+}{F} n_d \right) = \frac{\rho_{\mathrm{mem}}}{EW} \nabla \cdot \left(D^{\mathrm{eff}}_{\mathrm{mem}} \nabla \lambda \right) + S_\lambda \tag{7}$$

The first term on the left-hand side represents electro-osmotic drag, while the diffusion term on the right-hand side accounts for back diffusion due to concentration gradients.

The electro-osmotic drag coefficient is given by [36]:

$$n_d = \frac{2.5\lambda}{22} \tag{8}$$

The effective diffusion coefficient is:

$$D^{\mathrm{eff}}_{\mathrm{mem}} = \begin{cases} 3.1 \cdot 10^{-7} \lambda (e^{0.28\lambda} - 1) e^{-2436/T} & 0 \leq \lambda \leq 3 \\ 4.2 \cdot 10^{-8} \lambda (161 e^{-\lambda} + 1) e^{-2436/T} & 3 \leq \lambda \leq 17 \end{cases} \tag{9}$$

Sorption/desorption between gas and ionomer phases is modeled as:

$$\mathrm{H_2O_{gas}} \longleftrightarrow \mathrm{H_2O_{dissolved}} \tag{10}$$

with source term:

$$S_\lambda = k_{gd} \cdot \frac{\rho_{\mathrm{mem}}}{EW} (\lambda_{eq} - \lambda) \tag{11}$$

where equilibrium water content is:

$$\lambda_{eq} = 0.043 - 17.81a - 39.85a^2 + 36a^3 \tag{12}$$

and k_{gd} is a constant sorption coefficient.

In general CFD implementations, this mechanism may be treated either as a surface source term at the CL/membrane interface or distributed volumetrically within the catalyst layer, depending on how the ionomer phase is represented in the numerical model.

Electrochemical model

Different CFD platforms implement the electrochemical description of PEM fuel cells using distinct strategies. Fluent provides a dedicated *PEM Fuel Cell* module, OpenFOAM relies on the open-source library *openFuelCell2* developed by Zhang et al. [4], while STAR-CCM+ requires the use of specific add-on modules such as *Electrochemical Reactions* and *Electrochemistry*. Among these, OpenFOAM is the only fully open-source platform, which facilitates the implementation of additional physics. Fluent allows limited user customization through the *pemfc_user.c* interface, whereas STAR-CCM+ supports User Defined Functions (UDFs) through the graphical interface, which can restrict modeling flexibility. Regarding water production, Fluent and OpenFOAM generate water from the ORR **??** directly in the ionomer phase within the catalyst layers [37]. In STAR-CCM+, water is instead produced in both gas and liquid phases inside the catalyst layer region, without direct generation in the membrane.

Similarly, the half-cell reactions are distributed over the entire catalyst layer volume in Fluent and OpenFOAM, while STAR-CCM+ adopts a lumped formulation at the CL/MEM interface, where the ionomer phase within the catalyst layer is not explicitly resolved. A brief discussion of the lumped approach proposed by Verducci et al. [38], used to account for ionomer-related resistances not explicitly modeled in STAR-CCM+, is provided in section .2.

Electrochemical kinetics

The driving force of the electrochemical reactions is the local activation overpotential, defined as:

$$\eta_{\mathrm{AN}} = \phi_{\mathrm{sol}} - \phi_{\mathrm{ionomer}} - U_{\mathrm{eq,AN}} \tag{13a}$$

$$\eta_{\mathrm{CAT}} = \phi_{\mathrm{sol}} - \phi_{\mathrm{ionomer}} - U_{\mathrm{eq,CAT}} \tag{13b}$$

where ϕ_{sol} and ϕ_{ionomer} denote the electric potentials in the solid and ionomer phases, respectively. In STAR-CCM+, these quantities are evaluated at the CL/MEM interface, whereas in Fluent and OpenFOAM they are computed over the entire catalyst layer volume.

The equilibrium potential U_{eq} is typically obtained from the Nernst equation [39], accounting for reactant activities. In the present work, it is approximated using a linear temperature dependence:

$$U_{\mathrm{eq}} = E^0 - \beta(T - T^0) \tag{14}$$

where E^0 and T^0 are the standard potential and reference temperature, respectively, and $\beta = 0.00089$ V/K is taken from [5].

The electrochemical reaction rates are expressed through Butler–Volmer kinetics:

$$j_{\mathrm{an}} = j_{0,\mathrm{an}} \left(\frac{C_{\mathrm{H_2}}}{C_{\mathrm{H_2,ref}}} \right)^{\gamma_{\mathrm{an}}} \left[\exp\left(\frac{-\alpha_{\mathrm{an}}^{\mathrm{an}} F \eta_{\mathrm{an}}}{R_g T} \right) - \exp\left(\frac{-\alpha_{\mathrm{cat}}^{\mathrm{an}} F \eta_{\mathrm{an}}}{R_g T} \right) \right] \tag{15a}$$

$$j_{\mathrm{cat}} = j_{0,\mathrm{cat}} \, (1 - \theta_{\mathrm{PtOx}}) \exp\left(\frac{-\omega \theta_{\mathrm{PtOx}}}{R_g T} \right) \left(\frac{C_{\mathrm{O_2}}}{C_{\mathrm{O_2,ref}}} \right)^{\gamma_{\mathrm{cat}}} \exp\left(\frac{-\alpha_{\mathrm{cat}}^{\mathrm{cat}} F \eta_{\mathrm{cat}}}{R_g T} \right) \tag{15b}$$

Platinum oxide formation at the cathode is included in the cathodic reaction through the simplified model proposed by Jomori et al. [40].

In Fluent and OpenFOAM, the current densities $j_{\mathrm{an/cat}}$ and exchange current densities $j_{0,\mathrm{an/cat}}$ are expressed in $[\mathrm{A/m^3}]$ due to the volumetric formulation of the catalyst layers. To ensure consistency with STAR-CCM+, these values are converted

using the catalyst layer thickness:

$$j_{0,\mathrm{STAR}} = j_{0,\mathrm{Fluent}} \cdot \delta_{\mathrm{CL}} = j_{0,\mathrm{OF}} \cdot \delta_{\mathrm{CL}} \tag{16}$$

This ensures consistency in the total generated current:

$$\begin{aligned} I &= \int_{\mathrm{V_{an/cat}}} j_{\mathrm{an/cat,\ Fluent}} \cdot dV = \\ &= \int_{\mathrm{V_{an/cat}}} j_{\mathrm{an/cat,\ OF}} \cdot dV = \\ &= \int_{\mathrm{S_{CL/MEM}}} j_{\mathrm{an/cat,\ STAR}} \cdot dS \end{aligned} \tag{17}$$

The performance of a PEMFC is evaluated through the average current density j, defined as:

$$j = \frac{I}{A_{\mathrm{FC}}} \tag{18}$$

The polarization curve, relating cell voltage to average current density, represents the main performance indicator of the system. The parameters used in eq. (15), common to all three software platforms, are summarized in Table 1.

Table 1 Parameters used in the Butler–Volmer equations (15).

Parameter	**Symbol**	**Unit**
Local current density	j_{an}, j_{cat}	A/m^3
Exchange current density	$j_{0,\mathrm{an}}$, $j_{0,\mathrm{cat}}$	A/m^3
Activation overpotential	η_{an}, η_{cat}	V
Concentration of H_2 / O_2	$C_{\mathrm{H_2}}$, $C_{\mathrm{O_2}}$	mol/m^3
Reference concentration	$C_{\mathrm{H_2,ref}}$, $C_{\mathrm{O_2,ref}}$	mol/m^3
Pressure coefficients	γ_{an}, γ_{cat}	-
Charge transfer coefficient	α_{an}, α_{cat}	-
Faraday constant	F	C/mol
Universal gas constant	R	J/(mol·K)
Oxidized Pt coverage	θ_{PtOx}	-
Temkin energy parameter	ω	J/mol

Electrical and ionic conductivities

The effective electrical conductivity σ_{el}^{eff} in the charge conservation equation (table 6.1) and in the material properties (table 4) is calculated differently in each software. Specifically, in Fluent

$$\sigma_{el,Fluent}^{eff} = \sigma_{el,Fluent}, \tag{19}$$

in OpenFOAM

$$\sigma_{el,OF}^{eff} = \frac{1}{1-\chi} \cdot \sigma_{el,OF}, \tag{20}$$

and in STAR-CCM+

$$\sigma_{el,STAR}^{eff} = \frac{\tau}{1-\chi} \cdot \sigma_{el,STAR}, \tag{21}$$

where σ_{el} are the solid-phase electrical conductivities of the porous components. In OpenFOAM the effective electrical conductivity depends on the medium porosity χ, whereas in STAR-CCM+ it depends on both porosity and tortuosity τ. The isotropic solid-phase conductivities σ_{el} are imposed to ensure consistent σ_{el}^{eff} across all models:

$$\sigma_{el,Fluent}^{eff} = \sigma_{el,OF}^{eff} = \sigma_{el,STAR}^{eff} = \sigma_{el}^{eff}. \tag{22}$$

The ionic conductivity σ_{ion} in the charge conservation equation is computed following Springer et al. [36], corrected by a factor $\varepsilon_{ion}^{1.5}$ to account for the ionomer fraction present in the CLs according to Goshtasbi et al. [41]:

$$\sigma_{mem} = \varepsilon_{ion}^{1.5} \cdot (0.541 \cdot \lambda - 0.326) \cdot \exp\left[1268 \cdot \left(\frac{1}{303} - \frac{1}{T}\right)\right]. \tag{23}$$

The ionomer fraction ε_{ion} is equal to 1 in the membrane, $0 < \varepsilon_{ion} < 1$ in the CLs for Fluent and OpenFOAM, and zero in STAR-CCM+ due to the absence of an ionomer phase in the catalyst layers.

Since STAR-CCM+ does not explicitly account for the ionomer phase in the CLs, the ionic resistance present in these layers is not naturally captured. To quantify this contribution, a lumped resistance approach following Verducci et al. [38] is adopted. In this approach, the anode CL ionic resistance is considered negligible, while the cathode CL resistance is calculated based on the effective ionic conductivity of the membrane and the geometric thickness of the CL. The lumped cathode CL

resistance is then incorporated in the STAR-CCM+ model by modifying the potential drop between the CL/MEM interface and the solid phase, effectively recovering the missing ionic voltage loss. This ensures that the electrochemical response of STAR-CCM+ is aligned with Fluent and OpenFOAM without altering the underlying 2D interface reaction formulation.

Computational domain

The computational domain of the case study selected for the benchmark consists of a portion of the parallel flow field-design PEMFC presented by Colombo et al. [31], named *zero-gradient*. This configuration assumes that all operating parameters are uniform along the channel direction, allowing the analysis to focus on the through-plane direction only. Taking advantage of the flow design and symmetry, only a half-channel segment of 1 mm length is considered in the present work, in order to reduce the computational cost. Inlet and outlet channel extrusions are included to ensure fully developed flow conditions at both ends of the PEMFC domain, following standard CFD practice. The computational domain and its dimensions are reported in fig. 6 and table 2, respectively.

Table 2 Computational domain thickness in μm.

Part name	**Thickness** $[\mu m]$
Cathode plate	600
Fluid channel$_{cat}$	400
GDL$_{cat}$	117
MPL$_{cat}$	22
CL$_{cat}$	10
Membrane	15
CL$_{an}$	7
MPL$_{an}$	22
GDL$_{an}$	117
Fluid channel$_{an}$	300
Anode plate	700
Total	2310

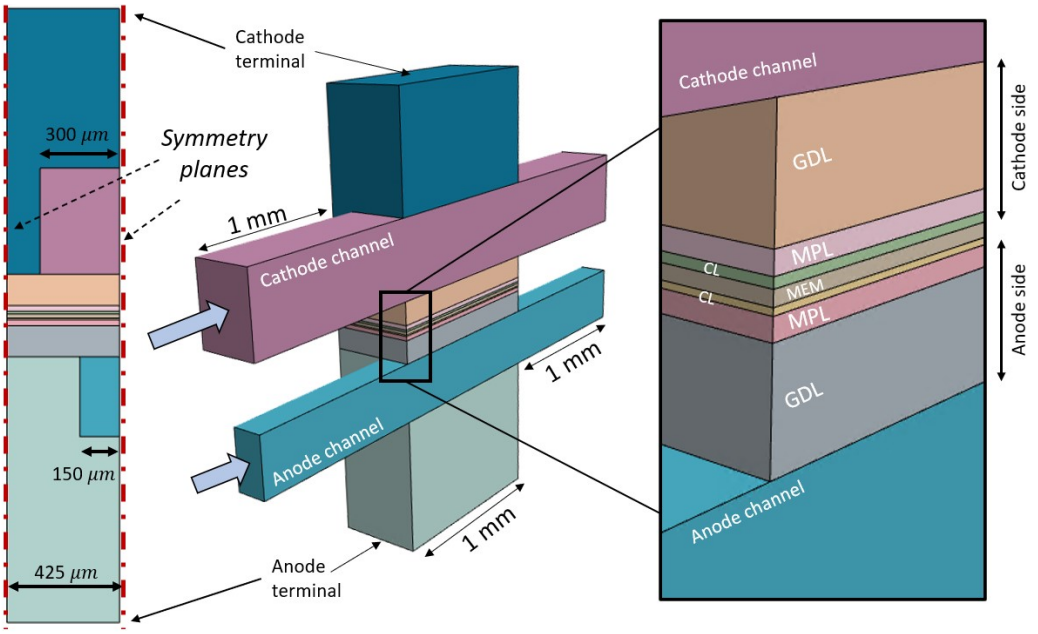


Fig. 6 Computational domain of PEMFC segment.

Operating conditions & material properties

The numerical simulations are performed under potentiostatic conditions, with a constant potential difference applied across the PEMFC terminals. The terminals are maintained at a uniform temperature $T = 353.15\,\mathrm{K}$, equal to the inlet temperature of the reactant gases, while all remaining external surfaces are treated as adiabatic. Molar fractions of inlet gases, inlet velocities, operating pressure, and relative humidity (RH) are reported in table 3. Material properties, listed in table 4, are assumed uniform and temperature-independent, due to the limited temperature variations expected within the PEMFC.

Table 3 Operating conditions of the experimental PEMFC adopted in the numerical models.

		Anode	**Cathode**
Velocity inlet	[m/s]	0.57	0.70
Pressure	[kPa]	250	230
RH	[-]	1	1
H_2O mole fraction	[-]	0.19	0.203
H_2 mole fraction	[-]	0.81	/
O_2 mole fraction	[-]	/	0.166
N_2 mole fraction	[-]	/	0.631

Table 4 Material properties adopted in the numerical models [5–7].

	ρ [kg/m^3]	χ [-]	k_{th} [$W/m/K$]	σ_{el}^{eff} [S/m]
s	2260	[-]	20	10000
GDL	2200	0.65	0.16	374
MPL	2260	0.44	0.16	447
CL	2170	0.40	0.20	200
MEM	1980	[-]	0.20	0